UNIVERSITY OF OKLAHOMA

GRADUATE COLLEGE

CREEPING WAVE PROPAGATION ON CYLINDRICAL RADIATING STRUCTURES

A THESIS

SUBMITTED TO THE GRADUATE FACULTY

in partial fulfillment of the requirements for the

Degree of

MASTER OF SCIENCE

By

Kristin Sperzel

Norman, Oklahoma

2019

CREEPING WAVE PROPAGATION ON
CYLINDRICAL RADIATING STRUCTURES

A THESIS APPROVED FOR THE
SCHOOL OF ELECTRICAL AND COMPUTER ENGINEERING

BY

Dr. Caleb J. Fulton, Chair

Dr. Jessica Ruyle

Dr. Hjalti Sigmarsson

Table of Contents

List of Tables

List of Figures

Abstract

Weather radar is a powerful tool for detecting hazardous weather that may impact the lives of many. Most weather radars used by meteorologists today rely on a mechanical sweep to obtain volumetric data. This mechanical sweep takes at minimum, four minutes to complete a full scan and there is not great flexibility in the scanning pattern. Phased array radars have been introduced as part of a multipurpose plan to replace current weather radars. Phased array radars allow scanning flexibility with fast scanning capability, such as electronic beam steering. When planar phased array radars are made to be polarimetric, which is necessary for accurate weather detection and prediction, bias errors occur that corrupt the data. In order to have the flexibility and swift updates of a planar phased array radar without the bias errors, a cylindrical phased array radar was created. Cylindrical phased array radars have the unique challenge of a type of surface wave, called a creeping wave, that causes back radiation levels to be destructive to pattern quality. Energy from broadside of the radar is azimuthally carried towards the opposite side. This challenge has not been greatly explored due to cylindrical phased arrays being on the leading edge of radar technology. This thesis seeks to explain, address, and mitigate front-to-back pattern isolation level problems that prevent the radar from reaching its meteorological potential. The two methods used in this thesis to intensify ways to reduce back radiation levels are called phase mode elimination and alternating projections.

Chapter 1

Introduction

Traditional weather radar systems use dish antennas that rotate mechanically to gather weather data, but in recent years rapid scan radar technologies have become more widely used to improve scanning functionality. Traditional dish-based radars rotate mechanically, and this mechanical motion is limited in speed, even when high-quality equipment is used to rotate the radars. Additionally, the mechanical rotation causes wear on the mechanical parts that is unavoidable. The mechanical scanning arrangement of a dish radar confines volume scans to a sequential beam sweep through a designated cycle. The mechanical confinement also does not allow for update of volume scans at rates faster than every four minutes [1]. A four minute volume scan is problematic because weather changes rapidly. For example, cyclones may form and then dissipate in seconds, and a four minute volume scan would miss this occurrence. In contrast, phased array radars do not require mechanical motion and have flexibility in scanning arrangement; this means the total update time and the sequence in which angles are scanned are not bound by the mechanical rotation of the radar [1]. The fast update times combined with dual-polarization capabilities of phased array radars enables unique data collection of efficient aircraft tracking, wind profiling, and observation of rapidly changing weather phenomena among many other applications. The intended next generation of radars, for the

above reasons, would combine nine different radar systems into one phased array radar that will improve long term cost and functionality [2]. The improved long term cost comes from having identical radars and system components; there will be no need to have extra radar technicians for different types of systems, since there will be only one system. Additionally the long term cost of PARs are lower than that of radar dishes. A phased array radar can still function if a few elements fail, but a dish cannot function if its only antenna fails. This multifunctional radar initiative was refereed to as MPAR (Multifunction Phased Array Radar), and was the original motivation for creating a cylindrical phased array. In more recent years the initiative was updated to Spectrum Efficient National Surveillance Radar (SENSR), a program designated to making a component of the L-band available and designated for the initiative's use [3]. Additionally, in recent years the meteorological applications were rescinded from the program. At this point the cylindrical array project was well underway and still geared towards weather radar. All is not lost though because phased array radars still remain a good candidate to replace the nations weather radar surveillance radar, called the WSR-88d, a polarimetric dish radar. One of the most common forms of phased array radars currently used is the planar version of polarimetric phased array radars (PPAR). One challenge of using a planar PPAR is the cross-polar biases that occur [4] [5]. Cross-polar biases occur due to the loss in orthogonality between single polarizations when electronically steering the beam away from the principal planes. These biases can be detrimental to data collection and lead to inaccurate results. Several techniques have been developed to mitigate cross-polar bias, such as pulse-to-pulse phase coding [6] [7], correction matrices [4], and using a cylindrical structure rather than a planar structure. The content of this work will focus on cylindrical polarimetric phased array radars (CPPAR) and cylindrical radiating structures. CPPARs have the same fast

volume scan times and scanning arrangement flexibility as planar PPARs while additionally enabling a 360° scanning range in the azimuthal direction. CPPARs are a solution to the cross-polar biases that occur with planar PPARs because a CPPAR is capable of commutating scans where the beam is electronically shifted in azimuth while maintaining symmetry around the beam center. As a result, the radiation pattern in azimuth is scan invariant and there is no loss in orthogonality between the two polarizations thus, making CPPAR a useful solution to the cross-polar bias issues that arise with planar PPARs. [8]

Due to CPPARs being a relatively new and uncommon technology, there is a great deal of electromagnetic phenomena that is yet to be understood [9]. It is well known that planar PPARs produce surface waves and leaky waves and there is a robust field of research for planar waves. Similarly, cylindrical radiating structures have cylindrical surface waves that are analogous to those of a planar structure. However, cylindrical radiating structures also produce creeping wave modes in addition to cylindrical surface waves. Creeping wave modes refer to azimuthally propagating waves on a cylindrical structure with a high attenuation rate in the azimuthal direction. These wave modes occur whether a dielectric coating is present or not [10]. Creeping waves are responsible for ripples in the far field radiation pattern and cause significant back radiation, both of which are significant draw backs to cylindrical phased arrays. *Back radiation* refers to the radiation opposite of broadside on a cylindrical array. More specifically, roughly between the angles of $-180° \leq \phi \leq -160°$ and $160° \leq \phi \leq 180°$. These two effects become detrimental to overall pattern quality [11]. One reason pattern quality needs to adhere to strict thresholds, such as low back radiation levels, is to use minimal frequency spectrum or to reuse spectrum when operating the radar. Reusing spectrum is cost efficient when purchasing rights to use sections of the spectrum, which is expensive. In or-

der to use the same frequency for any azimuthal direction on this cylindrical array, front-to-back isolation must be below -80dB in order for meteorological data to remain reliable [2]. It is important to manage creeping waves effects so the -80dB front-to-back isolation levels are achieved, and the benefits of using a cylindrical phased array radar may be realized. The first step in managing creeping waves is understanding them in a conceptual and mathematical sense so the phase modes may be manipulated.

The mathematical and physical nature of the radiation pattern from a cylindrical array or radiating structure is periodic and thus may be represented as a Fourier series, where each term in the Fourier series is a phase mode [2]. Thus, the Fourier series resulting from the radiation pattern with respect to θ_s and ϕ may be represented by

$$\mathbf{E}(\theta_s, \phi) \cdot \hat{n} = \sum_{m=-\infty}^{\infty} a_m e^{jm\phi}, \tag{1.1}$$

where a_m is the phase mode coefficient, $\hat{\mathbf{n}}$ is the unit vector normal to the far-field pattern, and θ_s is a specific elevation angle. This mathematical framework provides the basis for the electromagnetic analysis in the remainder of this paper.

The raw data from both CPPAR demonstrator, a cylindrical polaremtiric phased array radar that was built by the University of Oklahoma, measurements and simulations puts the front to back isolation levels around -40dB to -50dB. The CPPAR Demonstrator will be fully introduced in Section 2.3. These levels are not acceptable for the above meteorology standards. One post processing method to bring the levels down is to eliminate certain phase modes in the phase mode spectrum through antenna engineering concepts. This will be covered in Section 2.4 and Chapter 4. The next post processing method used is alternating projections. This method uses

the Moore-Penrose psuedoinverse to create a mask that forces the radiation pattern below defined thresholds. The alternating projections method attempts to reconcile differences between an ideal set of data, which will be called the "mask," and the raw simulated data, to preserve aspects of the far field radiation pattern that are desired and needed and eliminate or suppress components of the far field pattern that do not contribute to the data in a useful way. The alternating projections method will be introduced in Section 2.2.

The overall structure of the thesis will first provide a background for all simulations and experiments covered in this thesis. Chapter 2 will give an overview and understanding of creeping waves, as the creeping waves are the most integral component to this research. Chapter 2 next covers the method of alternating projections and introduces the CPPAR demonstrator created by the OU Radar Innovations Laboratory. The final component Chapter 2 covers is the work from [8] regarding the effects of eliminating specific phase modes to help the back radiation levels. Next, Chapter 3 describes the method of simulation and unit cell data processing for cylindrical arrays in detail. Chapter 3 also includes a fundamental simulation of a cylindrical phased array radar using simple slot antennas, with a study on perfectly matched layer (PML) boundary placement. This is done in order to ensure mathematically caused convergence issues do not occur on simulated data. Next, Chapter 4 will cover CPPAR simulations and measurements. This includes the alternating projections method and phase mode elimination applied to simulated CPPAR data, to determine how the back radiation levels are affected. The final chapter, Chapter 5, will conclude this thesis and provide a base for future research to be carried out.

Overall this thesis seeks to asses what methods of pattern adjusting or simulation details best help lower back radiation levels for cylindrical arrays. The three methods being focused on in this thesis are the phase mode elimination method,

alternating projections, and PML placement for simulations.

Chapter 2

Background Information and Fundamentals

2.1 Cylindrical Surface Waves and Creeping Waves

Cylindrical phased array radars provide a multitude of benefits to improve observing weather data, such as 360° scanning and fast volume update times without bias issues. However, the conformal nature of cylindrical phased array radars introduces a new challenge called creeping waves. Creeping waves are integral to understanding the complexities of CPPARs. To understand creeping waves, it is natural to progress by first defining and understanding surface waves on planar arrays. A planar phased array radar is made up of many individual antennas that are organized in a two dimensional pattern. The radar beam is steered electronically by implementing a different relative phase to each element in a vertical or horizontal manner. These elements are usually placed periodically on a dielectric slab. The dielectric structures that the antennas are placed on may support *surface waves*, waves that are lossless and travel tangential to the surface of the dielectric. Surface waves travel slower than the speed of light and remain close to the surface of the slab for all substrates [12]. For higher permeability substrates, The propagation constant of a planar surface wave, β, can be found using the following transcendental equation for TE waves,

$$k_1 cos(k_1 d) + j k_2 sin(k_1 d) = 0, \tag{2.1}$$

where k_1 is the wavenumber, d is the substrate thickness, For TM waves,

$$\epsilon_r k_2 cos(k_1 d) + j k_1 sin(k_1 d) = 0, \tag{2.2}$$

is used, where $k_1^2 = \epsilon_r k_0^2 - \beta^2$, $k_2^2 = k_0^2 - \beta^2$, and $\beta^2 = k_x^2 + k_y^2$ [12]. For cylindrical surface waves, higher level mathematics is used to find the propagation constant but the overall concept remains. Green's functions may be used to analyze electromagnetic fields based off a potential from a point or line source. More specifically, in the context of this thesis they are used to calculate the electromagnetic fields of planar slabs and cylindrical structures. Greens functions represent these electromagnetic fields as a spectrum of plane waves. The advantage of using Green's functions over other methods of analysis is that Green's functions provide closed form solutions that converge more quickly due to the simplicity of Maxwell's equations plane wave solutions [13] [14] [15]. For planar surface waves, the Green's function is expressed as a line integral in the complex plane, and poles and branch-point singularities appear within the plane [10]. A branch point singularity is a point in the complex plain where a function is not continuous when traversing around the point [16]. Instead of using a circle as the line integral, the branch point's respective branch cut must be avoided due to discontinuity along this line, as seen in 2.1. A branch cut is the line stemming from the branch point where the function is discontinuous. This can be visualized below in Figure 2.1 where α represents the branch point.

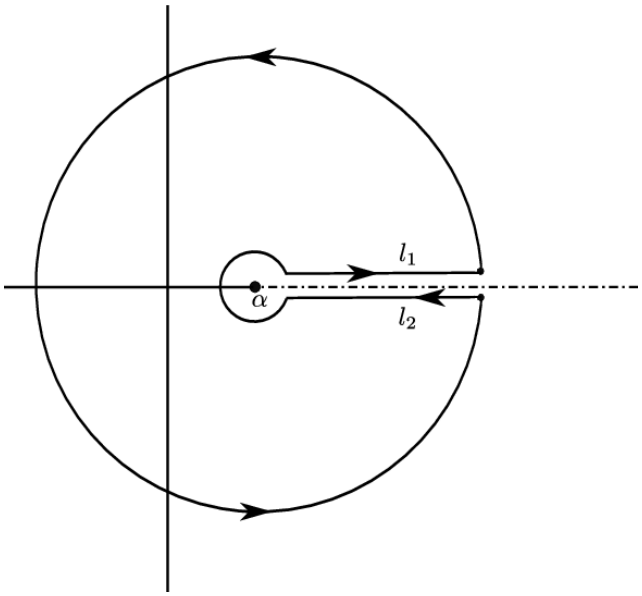

Figure 2.1: Branch point and the traversed function around the branch point with a respective branch cut.

However, the only singularities that occur in the complex plane for the cylinder are poles, without any branch points [10]. The integrand used in the complex plane to formulate the cylindrical Green's function uses Bessel functions, and this is why there are no branch points. The Bessel function basis is one reason why surface waves on planar arrays and surface waves on cylindrical arrays differ. The second reason is because planar arrays have one type of surface wave, while cylinders have two different types of azimuthally propagating surface waves. Creeping wave poles are poles that occur in a narrow region near the line integral representing the Greens function, as seen in Figure 2.2, where the black line represents the Greens function line integral in the complex plane and the green points represent creeping wave pole locations. These poles exist whether or not a dielectric coating/substrate is present and their location is weakly dependent on substrate properties [10]. There are also poles located to the right of the line integral in the complex plain that migrate de-

pending on the properties of the substrate; these poles represent cylindrical surface waves [10]. For comparison, surface wave poles for a planar phased array are shown in Figure 2.3. It should be noticed now that there are two different types of poles for cylindrical radiating surfaces. For cylinders: creeping wave poles represent cylindrical *creeping waves* and surface wave poles represent cylindrical surface waves. It is a common misconception that cylindrical creeping waves are analogous to planar surface waves. This is not the case. Cylindrical surface waves are analogous to planar surface waves. When the radius of a cylinder is increased, the cylindrical surface wave poles approach the locations of planar surface wave poles, while the creeping wave poles remain close to the integral line. Again, it is important that the two types of surface waves on cylinders be differentiated. Creeping waves can occur whether or not a coating is present and are the type of surface wave focused on in this body of work [10]. The conceptual difference between a planar surface wave and a cylindrical creeping or surface wave is shown in Figure 2.4. However there is not a clear way to visually show the overall difference between a cylindrical creeping wave and a cylindrical surface wave because both types propagate in the azimuthal direction.

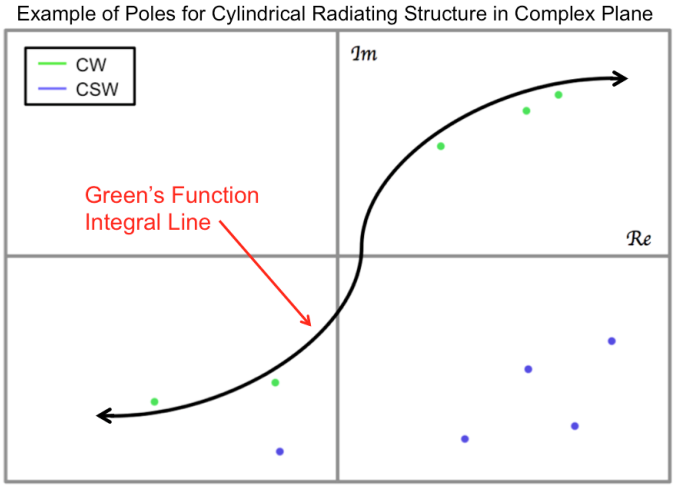

Figure 2.2: Example of creeping wave poles (green) vs. cylindrical surface wave poles (blue) in the complex plane surrounding the integration line for the Green's function for cylindrical radiating surface

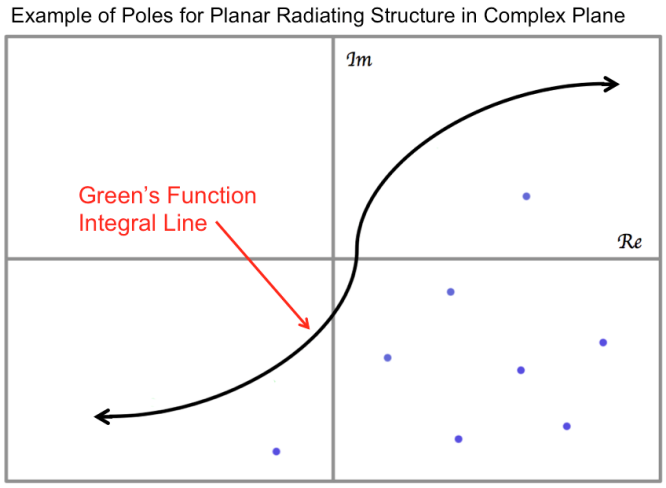

Figure 2.3: Example of surface wave poles in complex plane surrounding the integration line for the Green's function for planar radiating surface

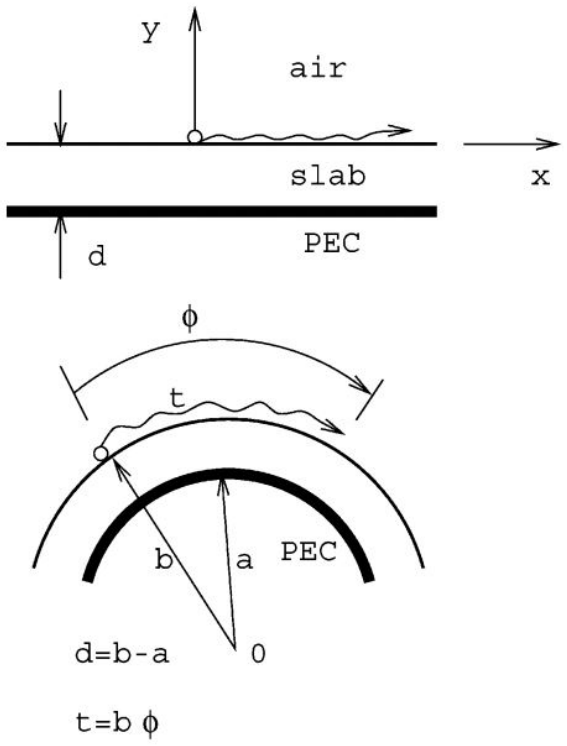

Figure 2.4: Illustration of surface waves on a planar coated surface and cylindrical coated surface due to line source [10].

2.1.1 Unit Cell Analysis by Fourier Series

The cylindrical array has a similar periodicity in the vertical dimension as the planar array; hence the use of Floquet analysis, an analysis often used for planar arrays, may be used vertically for the cylindrical array as well. The form of analysis used is called unit cell analysis and the technical process of performing unit cell analysis will be covered in Chapter 3. The fundamentals of unit cell analysis align with the fundamentals of array periodicity. Floquet analysis is an accurate way to account for the undesired complexities of mutual coupling and scan blindness that occurs in wide angle planar arrays, making the assumption that the array is large [17]. The

method can be used for smaller arrays as well, with some level of approximation. A periodic function that is used in a Fourier series can be represented as,

$$g(x) = \sum_{n=-\infty}^{\infty} f(x - na), \tag{2.3}$$

where the magnitude is represented by f and is periodic in x, with a being the periodicity constant. This series, when summed, approximates a function. The difference between a Fourier series and a Floquet series is that the input function for the Fourier transform, $h(x)$, is generalized to be periodic in both magnitude and phase as follows [18],

$$h(x) = \sum_{n=-\infty}^{\infty} f(x - na)e^{-jn\phi}, \tag{2.4}$$

where ϕ is the phase constant and j is the imaginary number. Electromagnetic fields produced by Floquet sources can be expressed in terms of Floquet modal functions with Fourier series input functions in the form of $h(x)$ [18]. This is the basis of Floquet analysis. Floquet analysis and periodicity is then used for unit cells and embedded element patterns to calculate the electromagnetic fields on finite arrays. For cylindrical arrays, a Fourier series, rather than Floquet series, is used to represent the periodicity regarding the creeping waves that travel in the azimuthal direction. This series is discussed in Chapter 3 to help understand unit cell analysis. Unit cell analysis is a necessary tool for analyzing creeping waves. Knowing these differences and similarities between creeping waves and surface waves, mathematically and conceptually, is important going forward. The above fundamentals will be more specifically applied to cylindrical arrays in this work. These fundamentals are the basis for a method called unit cell analysis. Unit cell analysis is similar to Floquet analysis but is used on cylindrical arrays. Unit cell analysis provides the

embedded element pattern as a sum of phase modes. This embedded element pattern can then be used to calculate an array's far field pattern. The resulting far field pattern is then used as the initial set of data for the alternating projections method.

2.2 Alternating Projections via Unit Cell Analysis

Certain types of beam shapes are required for different radar applications. Some applications require low side lobe levels, for example. Weather radar applications have many beam shape and pattern shape requirements due to the sensitive nature of parameters such as differential reflectivity, correlation coefficient, and reflectivity. Additionally, with cylindrical arrays, it is important to be able to re-use spectrum in order to avoid spending unnecessary money on frequency real estate. The strict requirements needed for weather data and the restriction on available frequency spectrum create a difficult back radiation threshold of -80dB front-to-back isolation. Along with the previously discussed methods of suppressing back radiation, a method called alternating projection pattern synthesis may be applied. Alternating projections is a post-processing method utilizing least squares approximation to project between matrix sets [19]. The matrix method used in this material relies on a math object called the Moore-Penrsoe Psuedoinverse.

2.2.1 Moore-Penrose Pseudoinverse

An inverted matrix, **B**, is the matrix that when multiplied by the original matrix, **A**, produces the identity matrix as follows,

$$\mathbf{BA} = \mathbf{AB} = \mathbf{I}. \tag{2.5}$$

However, this only works when the matrices are square matrices where $\mathbf{A}x = 0$ has only the trivial solution $x = 0$. Most matrices used in engineering do not have such properties. Often, **A** may have dimensions of n by m where $n \neq m$. For complex matrices, a matrix-like object called a psuedoinverse may be used. The psuedoinverse does not confine **A** to having dimensions $n = m$. The Moore-Penrose psuedoinverse is a specific type of psuedoinverse used in linear algebra, and the most commonly used one. The "pseudo" component of the name comes from the fact that the product of the non-square matrix and its inverse only approximately recovers the identity matrix. The method essentially performs a least square error evaluation of the dimensions that recovers the identity matrix as closely as possible by minimizing the off-diagonal values and driving the main diagonal towards unity. This psuedo-inverse matrix will be applied to the alternating projections method in the next section as the weight matrix, $\underline{W}$.

2.2.2 Method of Alternating Projections for Phased Array Antennas

The alternating projection method is chosen over other methods due to it being simple with high quality convergence [19]. Two examples of these other methods include the Chebyshev synthesis method and Taylor synthesis method. These two methods, along with the others, are local optimization methods. These methods rely on convergence of each iteration and are limited in their ability to optimize the overall pattern [19]. The alternating projections method projects between two sets of data to find a desired result. The first set of data for the alternating projections method, which will be referred to as the mask, is the threshold set by application constraints. The second set is based on the measured data, and is the adjusted pat-

tern that may be actually realized. A mask and respective array pattern can be visualized in Figure 2.5 for better understanding. The method chooses initial weights for each element and then adjusts the weighting if the calculated pattern does not belong to the desired step [19]. The initial weights for each element are organized in an array, $\underline{W}$, which can be visualized in Figure 2.6.

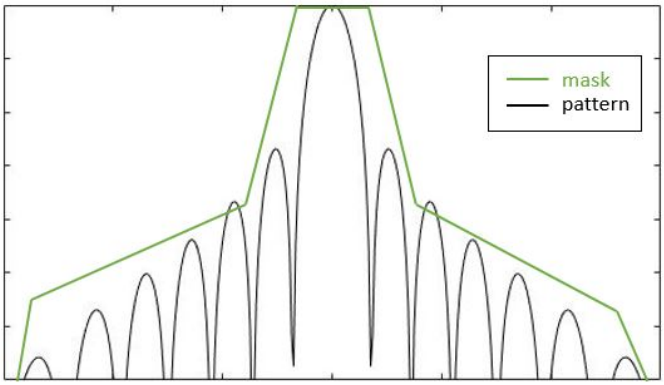

Figure 2.5: A general example of a mask and the resulting optimized pattern

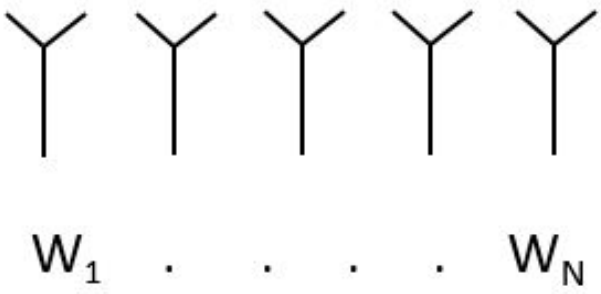

Figure 2.6: Array antenna elements with their respective weights labeled

Mathematically, the process is as follows; guess the antenna weights and call this vector W', then calculate $F'(\theta)$ and normalize $F'(\theta)$ to the peak value. Next, form $F'_{masked}(\theta)$ using Equation 4.2.

$$F'_{masked}(\theta) = \begin{cases} F'(\theta) & \text{for } |F'(\theta)| < mask \\ \frac{F'(\theta)}{|F'(\theta)|} * mask & \text{for else} \end{cases} \tag{2.6}$$

Once $F'_{masked}(\theta)$ is formed, find the best fit of $\underline{W}^2$ to produce $F'_{masked}(\theta)$.

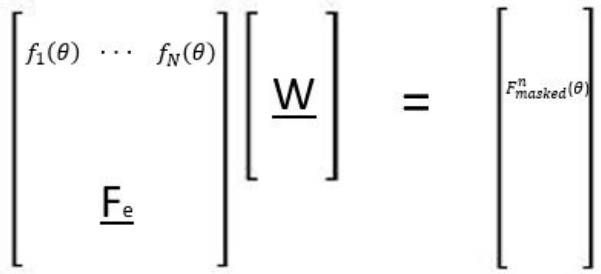

Figure 2.7: Matrix equation to find $F^n_{masked}(\theta)$

The final weights are then chosen using,

$$min[|\mathbf{F}_e(\mathbf{W}^n)^H - \mathbf{F}^n_{mask}|] \tag{2.7}$$

where this equation takes the minimum difference possible between the mask and the adjusted pattern. The final weights are then used to calculate the best far field pattern, producing the final result. In the next section, the final and best far field pattern for cylindrical simulations is shown with various different masks.

Applying Alternating Projections Method to a Generic Cylindrical Unit Cell Measurement

Too apply the above method to simulated data, the data must first be loaded into MATLAB. Next, the embedded element pattern is formed using the method found in Chapter 3.

where N is the total number of phase modes (as well as the number of columns), k represents each individual phase mode, and n represents an individual element. The scan angles θ_s and ϕ are the elevation and azimuthal scan angles, respectively. An example of an embedded element pattern that is formed from a cylindrical array simulation can be seen in Figure 2.8.

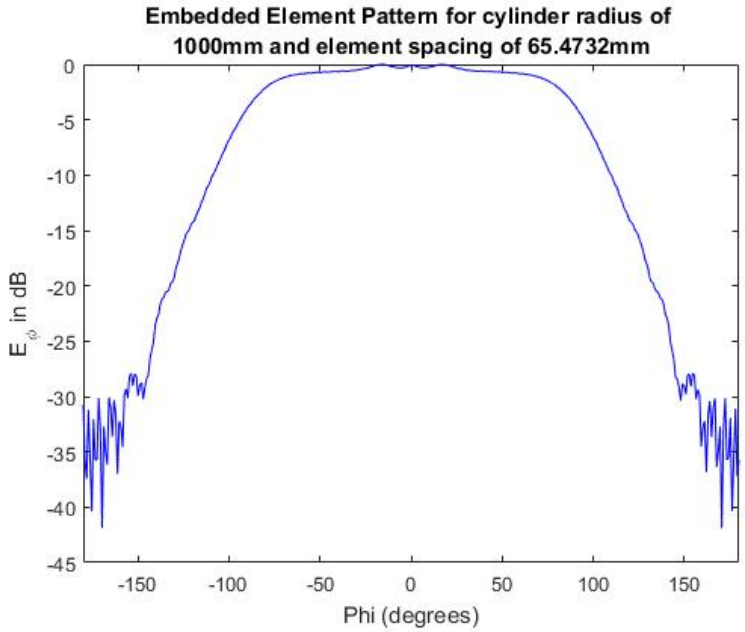

Figure 2.8: Generic cylindrical array embedded element pattern example

Once the embedded element pattern is formed it is circularly shifted N times to obtain an embedded element pattern for each column of the cylinder. Next, a sector of the cylinder is chosen because only a sector of columns are excited when

performing measurements on a functional cylindrical array radar. The number of sectors used will be represented by N_s and the number of columns per sector may be represented by N_c. Most commonly N_c is set to 20 or 22 columns, this number of columns amounts to a 90 degree sector. A plot of each of a sector's embedded element pattern for a 22 column sector can be seen in Figure 2.9.

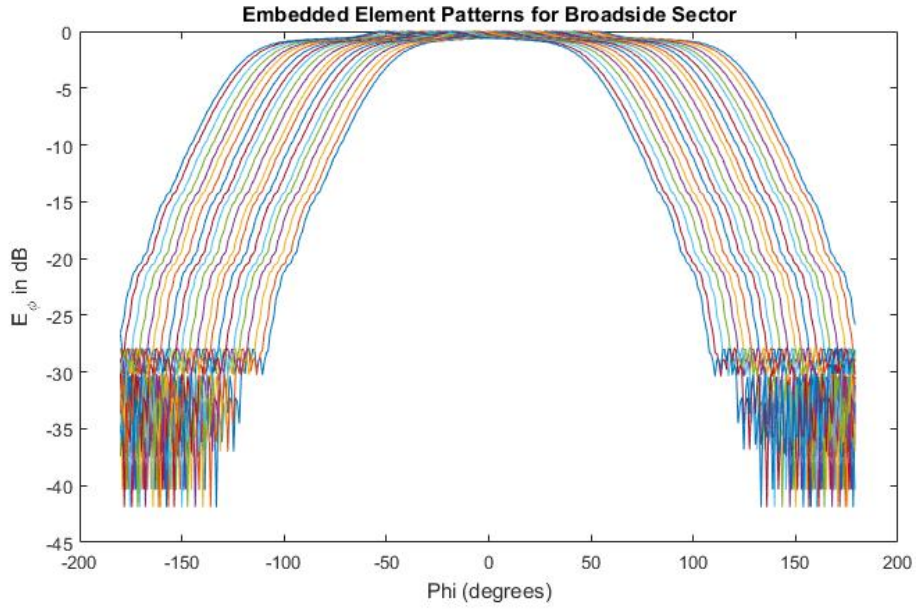

Figure 2.9: Embedded element patterns for broadside sector with 22 columns

Next, the far field pattern is formed by multiplying the element patterns by the array factor and an additional weight to account for the element density near the edges using,

$$\mathbf{E}_T(\theta_s, \phi) = \frac{e^{-jkr}}{r}\mathbf{f}(U, V) \sum_m w(m)|a_m|e^{j(kU - k_0U_0)mdx} \sum_n w(n)|a_n|e^{j(kV - k_0V_0)ndy}, \tag{2.8}$$

where $U = sin(\theta_s)cos(\phi)$, $V = sin(\theta_s)sin(\phi)$, $f(U, V)$ is the embedded element

pattern, $w(m)$ and $w(n)$ are the weights to account for element density near the edges, a_m and a_n are the element excitation weights, r is the radius of the cylinder, and k is the wave number. This equation is similar to the traditional method of calculating a far field radiation pattern for planar phased arrays, using an array factor and element spacing. However, this equation has an additional weight component to account for the cylindrical nature of the conformal array. This far field pattern is then the initial set of data, $F'(\theta)$, used in Section 2.2.2. An example of a far field pattern formed using this equation, from the embedded element patterns, can be seen in Figure 2.10

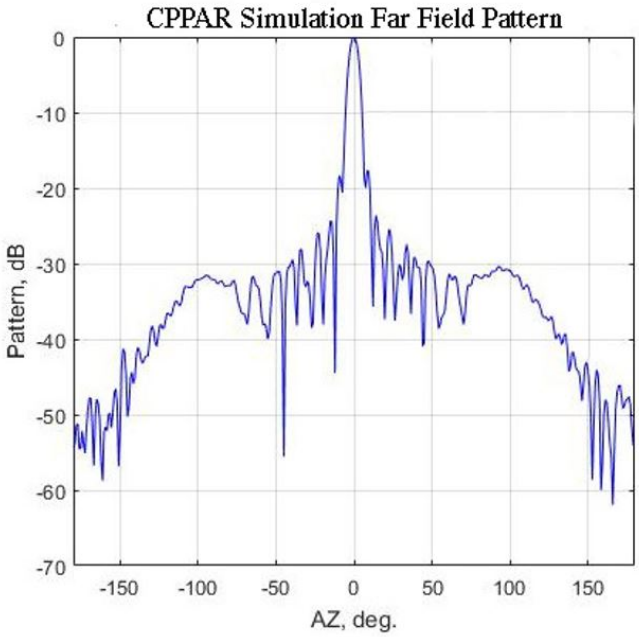

Figure 2.10: Far field pattern example resulting from using Equation 2.8

This alternating projections method will be later used on simulated data for a cylindrical polarimetric phased array radar in HFSS. This simulated data will be based off a radar called the CPPAR Demonstrator.

2.3 The CPPAR Demonstrator

The Advanced Radar Research Center designed and built one of few existing cylindrical polarimetric phased array radar demonstrators (CPPAR), shown in Figure 2.11. Creeping wave research in this thesis will be applied to this radar.

Figure 2.11: The CPPAR demonstrator on a pedestal inside the Radar Innovations Laboratory

The CPPAR demonstrator was built for weather applications, but could be useful for many of the desired mulit-purpase phased array radar (MPAR) applications. This radar has potential to replace the current standard WSR-88d weather radar. The CPPAR demonstrator allows measurable data to be compared to simulated data and theory for better understanding the electromagnetic occurrences on cylindrical radiating structures. This radar was initially populated by 48 columns of 19 square patch antennas, covering 180°of the cylinder. The columns are 1.52 meters in length [20]. The second half of the radar was populated by an additional 48 columns

in 2018. With a radius of one meter, this creates an element spacing of roughly 0.65λ, depending on what frequency is used. As indicated in the name, the radar is polarimetric and has both vertical and horizontal channels. This eliminates errors due to the loss of orthogonality. The CPPAR demonstrator is designed to operate between 2.7GHz and 3.1GHz, and has a 3dB beamwidth of roughly 5 degrees. In order to simplify the radar and avoid expensive element-level phase shifters, the beam is steered in the vertical direction by adjusting frequency and has a range of 20 degrees in elevation [20]. This shift is controlled by the length of the transmission lines. The array is series fed with only one T/R module per column [20]. The beam is steered in the azimuthal direction by commutating the active sector, it is not electronically steered in the azimuthal direction like a traditional planar array. This means every direction is "broadside" in a sense, and eliminates any bias issues encountered when steering away from broadside. A quick reference of these system parameters can be seen in Table 2.1.

Table 2.1: CPPAR System Parameters

Parameter	Value
Frequency	2.7-3.1 GHz
Power Radiated/Column	80 W
Number of Elements	1824
3dB Beamwidth	4.5-6.5 deg.
Cross-polarization	$<$-30dB everywhere
Scan Range (EL)	0-20 deg.
Radiated Power, Peak	1.5 kW
Max Duty Cycle	15%
Max Waveform Bandwidth	20 MHz

Designing the dual polarized antenna for this array was challenging due to the need for high cross-polarization isolation and low side lobes [20]. Each polarization was fed separately through stripline transmission lines and multi-layer patch technology was used to create high isolation [20]. The specific make up of the antenna is as follows: Tactonic TLX-8 was used as the material, and the antenna is made up of two patch antennas, two ground planes, and two aperture coupling transmission lines [20]. Two transmission lines excite the two different polarizations. These transmission lines also provide the series fed frequency steering feature of the array. The single element schematic is shown in Figure 2.12. As noted in the schematic, the spacing between the two patches is 5mm, the spacing between the bottom patch and the ground plane is 3.175mm, and the spacing between the two ground planes is 2×0.787mm with the feed network in the middle of the two ground planes.

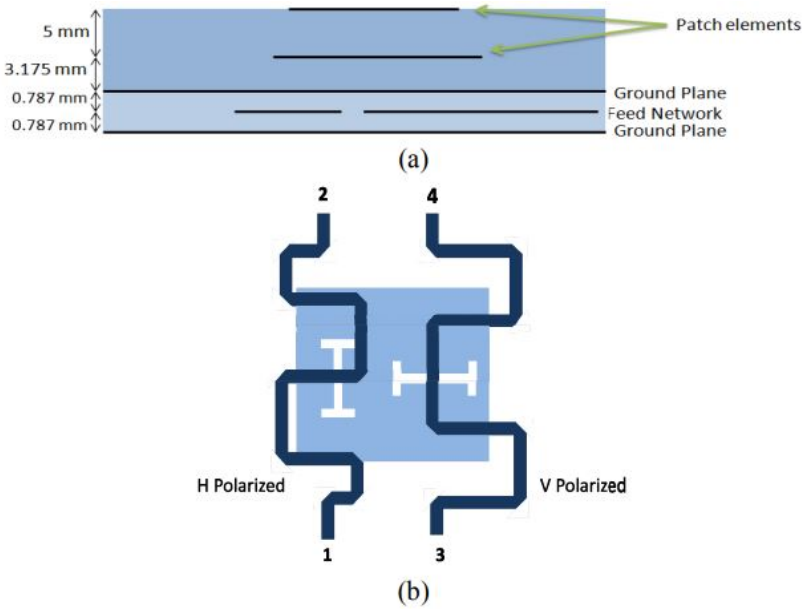

Figure 2.12: CPPAR antenna element schematic side view (a) and top view (b) [20]

Calibration is vital for any phased array's capability to make successful measurements. In order to test the CPPAR demonstrator and take measurements, careful calibration is needed to remove errors in the electric channels [21]. Calibration also enables corrections for mutual coupling and other electromagnetic effects such as fringing fields to be corrected [21]. To calibrate the CPPAR demonstrator, it was taken out to the open field near the Radar Innovations Laboratory. Two horn antennas were mounted on a support beam called the far field tower. The CPPAR demonstrator was then placed on a rotating platform so each column could be tested. In between the far field tower and the CPPAR demonstrator, radio frequency absorbers were placed in order to eliminate ground reflections. This set up can be seen in Figure 2.13. The far field set up was chosen because it was the easiest and most accurate way to obtain the amplitude and phase information from each column [21].

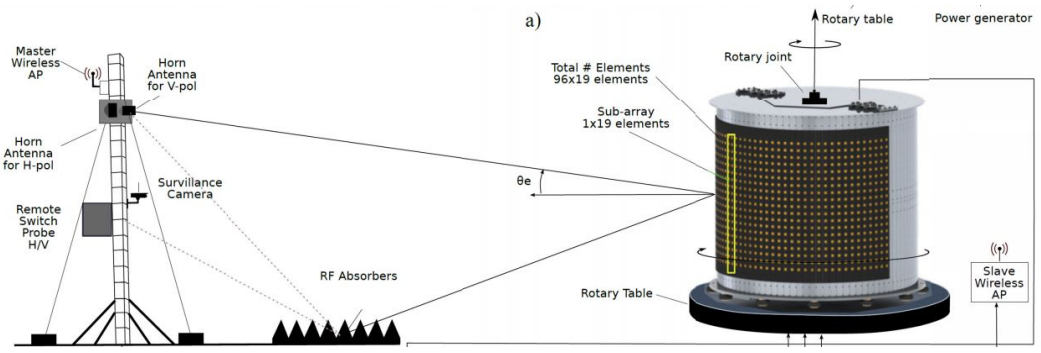

Figure 2.13: CPPAR test bed/calibration set up [21]

The horn antennas for the H and V channels are both linearly polarized and have a cross-polarization isolation of better than -40dB [21]. As the rotating platform turns, a column either receives or transmits depending on which mode is being tested. When the receiving mode is being tested a phase locked reference is connected to a switch box and each column of data is stored with a corresponding column number [21]. For the transmitting measurements, one polarization is transmitted at a time while the non-transmitting channel is used to store the data received by the far field horn [21]. The transmitting polarization channel transmits all sectors simultaneously [21]. The data is then stored and loaded into MATLAB to process. Once the data is processed, the errors in the electric channels, mutual coupling, and other electromagnetic effects may be accounted for to provide accurate far field patterns and electromagnetic data.

2.4 CPPAR Measurements and Motivation for Cylindrical Array Simulations

The CPPAR Demonstrator has been taking measurements since 2015. With each measurement, an undesirable amount of back radiation has occurred. It was found

in [2] that when the antenna elements had a spacing of 0.5λ instead of 0.5λ, the array did not encounter this problem. However, because the radar was already built and the element spacing could not be changed, new measurements were made with revisions put in place to try to eliminate the high levels of back radiation, such as putting electromagnetic absorbers where there were possible ground reflections and other problem areas occurring in the environment. This improved the amount of back radiation, but there was still a significant amount of disruption form the remaining levels of back radiation. With the knowledge that creeping waves are often responsible for adverse radiation effects, the measured data was imported to MATLAB so phase mode spectral analysis and experiments could be performed to study the creeping waves and their adverse effects. It was found that eliminating certain creeping wave modes, without making other adjustments, causes the back radiation to drop significantly. More specifically, due to the CPPAR Demonstrator having un-populated back half of the cylinder the creeping wave modes near the speed of light are enhanced. Figure 2.14 shows measured data for CPPAR demonstrator that was then run through MATLAB to find what would occur when certain creeping wave modes were eliminated. These measurements were taken using a frequency of 2.76GHz at a scan angle of 3° in elevation. It can be seen that the back radiation levels before the creeping wave modes near the speed of light are eliminated (top row), near $\theta = -180^\circ$ and $\theta = 180^\circ$ is equal to about -50dB. The first set of significant modes to be eliminated are the creeping wave modes near the speed of light, which are depicted by the yellow regions in the phase mode index column [2]. As some of the creeping wave modes in the yellow region are eliminated the back radiation levels begin to drop below -50dB. Finally, once all of the creeping wave modes are eliminated, the back radiation levels drop to roughly -60dB. This indicates that creeping wave modes directly affect back radiation levels, and elimi-

nating creeping wave modes will be advantageous in achieving the meteorological goal of a front-to-back isolation of -80dBc or below [8].

The second set of significant modes to be evaluated are the surface waves in the dielectric, which are depicted in Figure 2.15 by the purple regions in the phase mode index column. These surface wave modes do not affect back radiation, but still significantly impact the radiation pattern. Figure 2.15 shows the radiation pattern and phase mode spectrum before the purple region is eliminated, just after most of the purple region is eliminated, and finally once all of the purple region has been completely eliminated. It can be seen in the first row, where the maximum phase mode index is 49, that the radiation pattern is not symmetric and has many fluctuations within the overall pattern. Once most of the purple region has been removed, the back radiation level, and grating lobes remain the same but the pattern becomes more symmetric and smooth. The grating lobes are not removed because they are produced by the spacing of the elements in the array rather than the creeping waves. Planar structures and cylindrical structures are periodic, so when one element is excited, all spatial frequencies and phase modes are excited [2]. In turn, surface waves may be excited and will couple to all the elements in the array with a phase progression determined by the surface wave propagation constant [2]. The elements in planar arrays will then radiate in the grating lobe direction, opposing the direction of the surface wave, and cause a cancellation that results in blindness at particular scanning angles [2] [22]. A similar phenomena happens with cylindrical arrays, but this occurs in the phase mode spectrum instead of scan angle [2]. Additionally, once most of the surface waves in the dielectric (in the purple regions) are removed, the spectrum content is removed. This means there is no longer scan blindness in the radiation pattern. Lastly, as all of the dielectric surface wave modes and most of the creeping wave modes in general have been eliminated, aside from the seven-

teen remaining, the pattern becomes more symmetric, but the side-lobe levels and beamwidth begin to increase significantly [8].

Eliminating phase modes without making other adjustments resulted in a drop in back radiation levels for measured data. Physically filtering out the phase modes near the light line caused a drop in back radiation while physically filtering out the surface wave modes caused the pattern to behave more smoothly. This was done without making other adjustments to the back radiation levels. This motivates the need for further analysis of the phase mode content near the light line and surface wave indices. There is an apparent relationship between back radiation levels and the phase mode content near the light line, and a relationship between the surface wave indices and overall pattern shape. These relationships will be further investigated in this work by applying different filtering and pattern manipulation methods to simulated patterns. It is important to see what adjustments to the phase mode spectrum and patterns have the most important effect among alternating projections, phase mode elimination, and convergence.

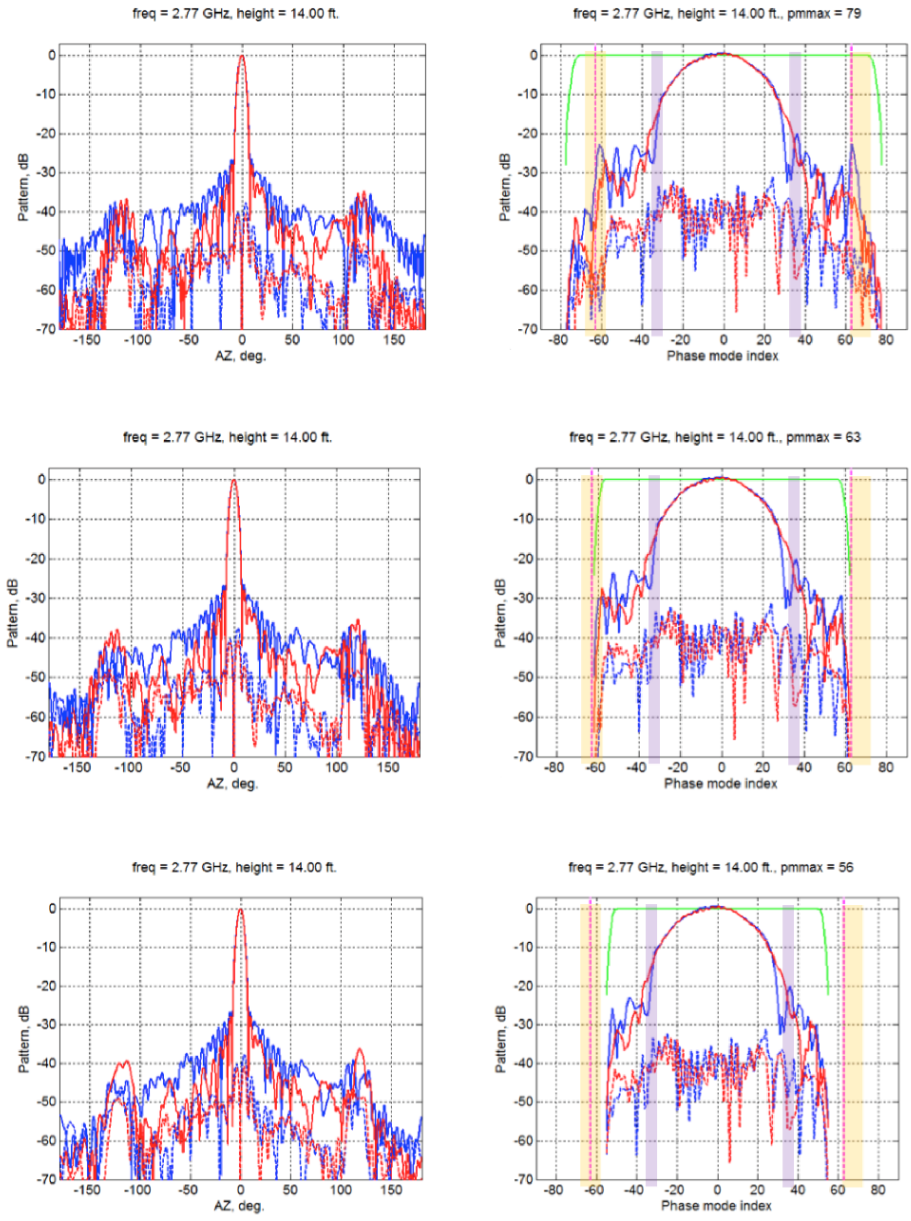

Figure 2.14: The measured radiation pattern from the CPPAR Demonstrator for different maximum indices is shown in the left column, where red is the vertical polarization and the blue is the horizontal polarization. The measured phase mode spectrum for different maximum indices is shown in the right column, where the yellow lines depict where the creeping waves are near the speed of light [8].

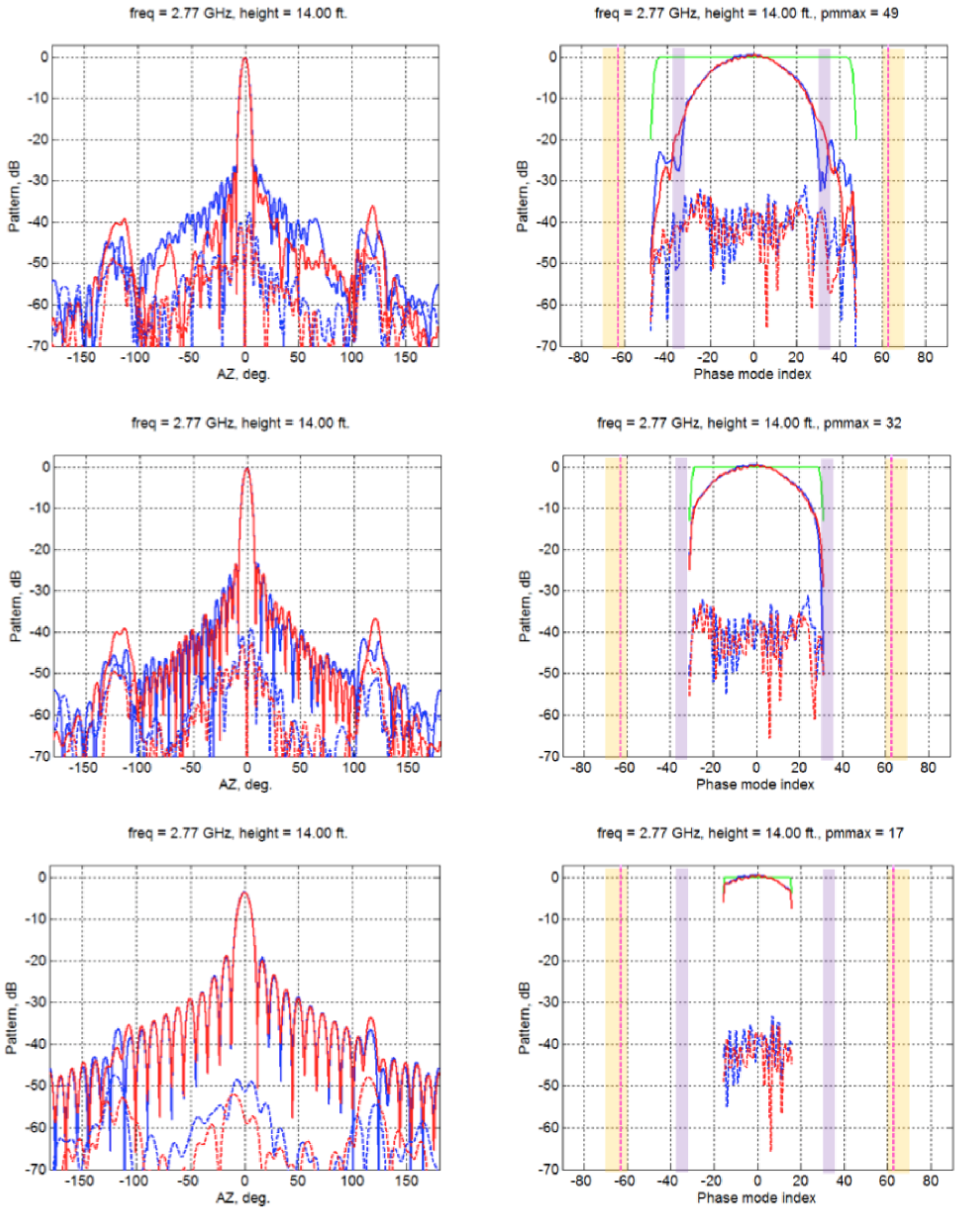

Figure 2.15: The measured radiation pattern from the CPPAR Demonstrator for different maximum indices is shown in the left column, where red is the vertical polarization and the blue is the horizontal polarization. The measured phase mode spectrum for different maximum indices is shown in the right column, where the purple lines depict the dielectric surface wave modes [8].

Chapter 2 Conclusion

Planar array concepts are a useful tool to give a simplified basis of knowledge on the periodicity and electromagnetic nature of arrays. Greens functions in the complex plane may be used to represent electromagnetic fields resulting from both types of arrays. Floquet analysis is a useful way to analyze planar array element patterns while the similar unit cell analysis may be used for cylindrical array element patterns. This knowledge translates planar array concepts to cylindrical array concepts, but it is necessary to keep one important difference in mind. This difference is that creeping waves and cylindrical surface waves are different types of waves that occur on a cylindrical surface. The stubborn nature of the creeping wave poles, that are weakly affected by substrate properties and occur weather or not a dielectric is present, make them difficult to deal with. Creeping waves will cause undesired effects such as high back radiation levels for all simulations and measurements shown in this thesis.

The alternating projections method combined with unit cell analysis provides a good basis to investigate back radiation levels created by creeping waves on cylindrical arrays. The alternating projection concept and math for generic cylinder unit cells is provided, and will be applied in Chapter 4.

Additionally, the CPPAR demonstrator is a physically realized radar created by the University of Oklahoma. This radar has 96 columns that each have 19 elements, for a total of 1824 elements. The radar operates in the same frequency range as the SENSR project (2.7-3.1GHz) and was created to take weather data measurements. The antenna elements are created using multi-layer technology and use two patches, two ground planes, and two separate feed lines to provide dual polarization capabilities. Calibration is a vital component to ensuring the radar functions well,

calibration methods were carried out using a far field test bed set up.

Once the CPPAR demonstrator was properly calibrated, it was able to take measurements. These measurements were then processed in MATLAB. It was found that eliminating phase modes that corresponded to phase mode content near the speed of light lowered back radiation, alluding to a strong relationship between such phase modes and back radiation levels. Additionally, eliminating the phase mode content that corresponded to cylindrical surface waves provided a more predictable and "clean" pattern, alluding to a relationship between cylindrical surface waves and pattern shape, as expected. These findings provide motivation to investigate phenomena through simulated data, where results are more ideal than measured data where interference may occur.

Chapter 3

Details on Unit Cell Analysis of Cylindrical Arrays

3.1 Method of Processing Unit Cell Simulation Data

For unit cell analysis, an HFSS simulation calculates the electromagnetic fields for one element of an array. In order to obtain a radiation pattern for the entire array, MATLAB will be used. The array pattern is computed by exporting the data obtained from the HFSS unit-cell simulation and performing mathematical computations. The excitation of the 0^{th} element only is the sum of all cylindrical phase sequence excitations (CPSE) [2]. A CPSE is a harmonic excitation and each CPSE produces one or two phase modes to the array radiation pattern for arrays with element spacing from 0.4λ to 0.8λ [2]. This means every phase mode that contributes to the radiation pattern may be extracted from

$$c_{l+pN}^{(l)} = a_{l+pN} = \frac{1}{N} b_{l+pN}^{(l)} \forall p, l = 0, 1, ..., N-1, \tag{3.1}$$

where p is an integer, N is the number of phase modes, $b_m^{(l)}$ is the phase mode coefficient of the l^{th} CPSE, $c_m^{(l)}$ is the coefficient of the unit cell field under the l^{th} CPSE, and as stated above, a_m is the Fourier series phase mode coefficient [23] [2].

A MATLAB function was created to take the 0^{th} element pattern, phase shift the array by $2\pi/N$, and then add the phase shifted calculation to the total pattern. This can be mathematically represented as

$$\mathbf{E}(\theta_s, \phi) = \frac{1}{N} \sum_{k=0}^{N-1} \sum_{n=0}^{N-1} \mathbf{E}(\theta_s, \phi - \frac{2\pi}{N} n) e^{j\frac{2\pi}{N}nk}, \tag{3.2}$$

where k is the k^{th} CPSE and n is the column number, θ_s is the scan angle in elevation, and ϕ is the azimuthal angle. The total sum is equal to the embedded element pattern. A slot antenna cylindrical array is used as a measurable means to study these phase mode effects using the framework from Section 3.2.

3.2 Unit-Cell Analysis

Unit cell-analysis is a useful tool for CPPAR simulations, and cylindrical phased array simulations in general. It is helpful to relate a planar array simulation method to cylindrical unit cell analysis. For planar arrays, a well established method of computing electromagnetic fields, called Floquet analysis, is often used to simulate large arrays while accounting for mutual coupling and scan impedance effects [2], [24]. Floquet analysis is performed by using a base element or structure while computing all scan angles in parallel to avoid computing thousands of elements separately [2]. A similar method [2] of unit-cell analysis was created for cylindrical structures due to the axial symmetry of cylinders. The periodic nature of a cylinder allows for this unit-cell based analysis to be used in the azimuthal direction of the array while Floquet analysis is used for the vertical dimension of the array. This simulation technique allows for less obtuse simulation times and usage of computational resources with no loss in pattern accuracy if set up correctly. With traditional means of simulating an entire array, the computation usage goes up by $\mathbf{N}^3$, where **N**

is the number of elements in the array. On the other hand, the computational usage for the unit-cell technique increases linearly with **N**, making the unit-cell technique particularly advantageous for medium to large arrays where a high percentage of the elements see the same electromagnetic environment that they would see in an infinite array. Additionally, unit-cell analysis for cylindrical arrays has been shown to have strong agreement with measured results. The measured results from the CPPAR demonstrator were compared to a cylindrical unit-cell simulation in [2] and the results are shown in Figure 3.1. It is noted that in [2], a frequency of 2.77GHz is used for both measured and simulated data. The method of these simulations and measurements will be covered in 4.1.

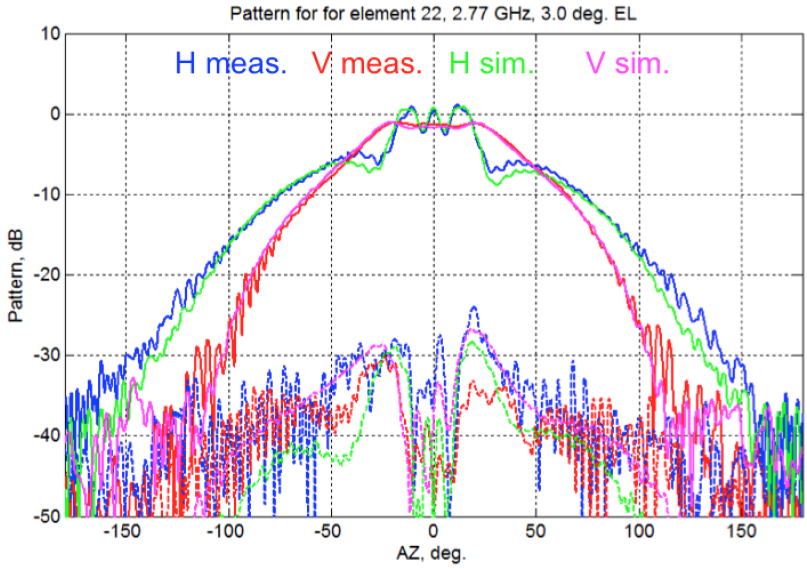

Figure 3.1: CPPAR Demonstrator patterns: phase mode simulation vs. initial measurements for illustration purposes [2]

A slot antenna is used for simplified cylindrical array unit cell simulations. The simulation is designed in ANSYS HFSS, a finite element method solver for electromagnetic structures. The HFSS design is set up to simulate a cylindrical array made of 96 elements, with a cylinder radius of one meter. A slot antenna is chosen over

other antenna designs because a patch antenna may be modeled as an array of two slot antennas, both antennas have similar properties which are discussed in the A.1 section of the Appendix. The height of the slot is much shorter than the width of the antenna; the height is also chosen so that two slots approximate the height of what a patch antenna would be. The slot antenna is seen in Figure 3.2, and has a height of 10mm, width of 32.74mm, and slot width of 1mm. A more detailed view of the slot antenna can be seen in Figure 3.3. It can be seen that the slot is infinite with two small sections of perfectly conducing magnetic material at the top and bottom of the slot. The slot is then excited by a wave port, rather than the more traditionally used lumped port. The placement of the two perfectly conducting magnetic sections and wave port excitation is explained in the Appendix in Sections A.3 and A.4. The material used for the antenna is a finite conductivity with no substrate in order to keep the design and results simplified. The antenna is has a single polarization in the horizontal direction, again, for simplicity. Complex antenna designs or cross-pol bias errors from dual polarization can interfere with the electromagnetic and far field results on a fundamental level. By using such a simple antenna, it will be more apparent what effects are caused by the array's cylindrical nature. The final important component to this design is the PML used to truncate radiation at the end of the air-box. A PML was chosen over a radiation boundary, as described in detail in the Appendix, Section A.2.

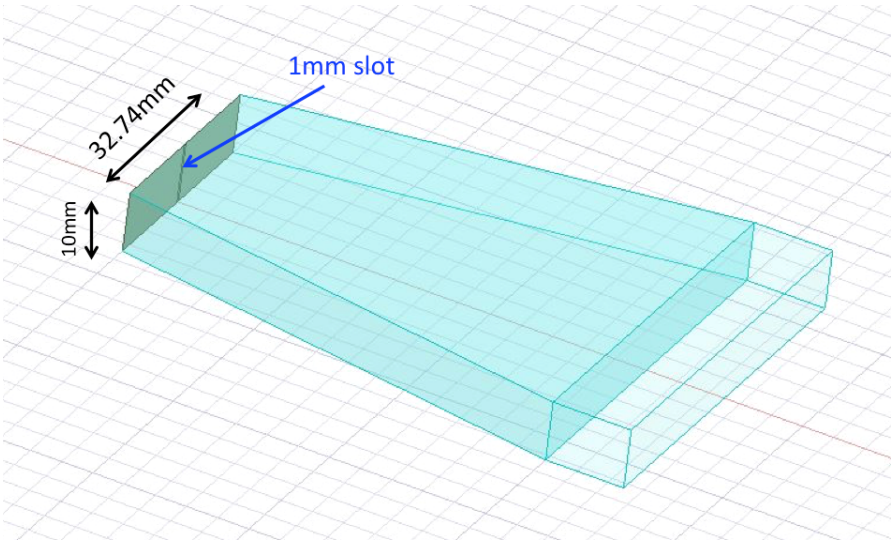

Figure 3.2: Slot antenna design in HFSS

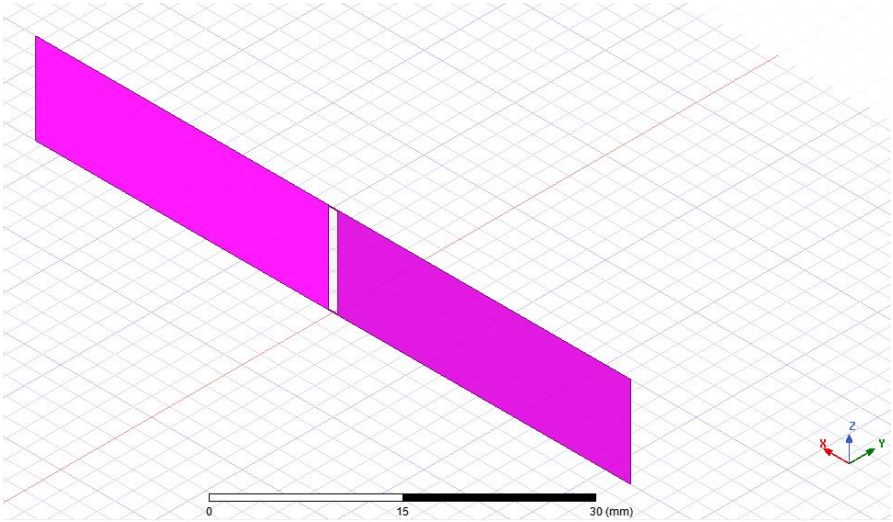

Figure 3.3: Detailed view of slot antenna design in HFSS

3.2.1 Unit-Cell Analysis Set Up and Configuration

The unit-cell analysis mentioned above is used and the cylinders are placed axially along the $\hat{z}$ axis with the 0^{th} element facing the positive $\hat{y}$ axis as seen in Figure 3.4. However, unlike Figure 3.4, the HFSS simulations will not include all

columns of the array. The simulation will compute one element, specifically the 0^{th} element, and use master/slave boundary conditions to emulate the full array of elements. Figure 3.5 [2] points to the boundary conditions mentioned above. The first master/slave boundary conditions are located on the "air-box" surfaces which are parallel to the x-y plane. These two boundaries emulate currents on these surfaces as if there were an infinite array of elements both above and beneath the unit-cell. The "Slave 1" boundary condition follows a phase difference of $k_0 dz \cos(\theta_s)$ between the bottom and top boundaries. The second master/slave boundary conditions are located on the "air-box" and are perpendicular to the x-y plane. The second master/slave boundary conditions create a phase difference between the master and slave by $k2pi/N$ to emulate a fully populated cylinder in the azimuthal direction. The perfectly matched layer (PML) is the square box in Figure 3.5 that is capping the wedge-shaped air-box. In HFSS, a PML is a radiation boundary that emulates reflection-free radiation [25]. If the PML were not present, the default radiation boundary for HFSS would be a short at the end of the air-box. This would result in disruptions in the radiation patterns that would not physically be present in an experimental measurement.

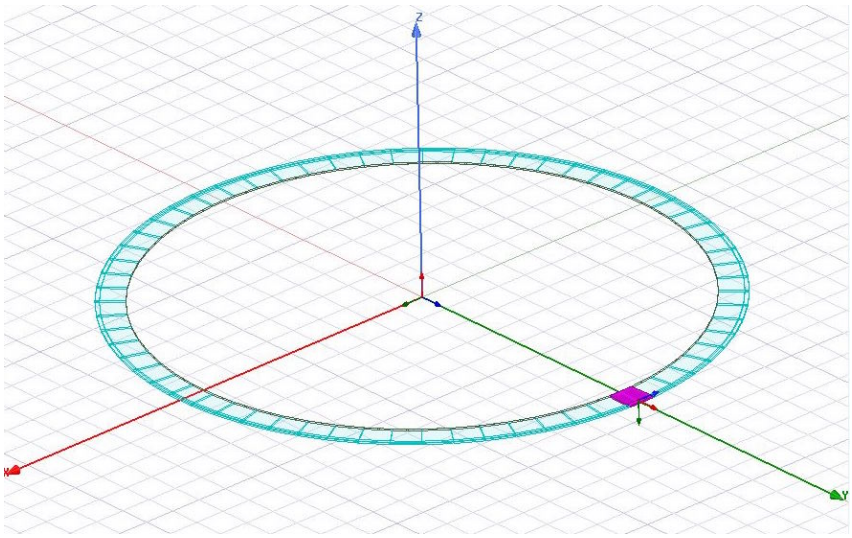

Figure 3.4: The base row of elements in a cylindrical array showing the orientation about the $\hat{z}$ axis with the 0^{th} element facing the $\hat{y}$ axis

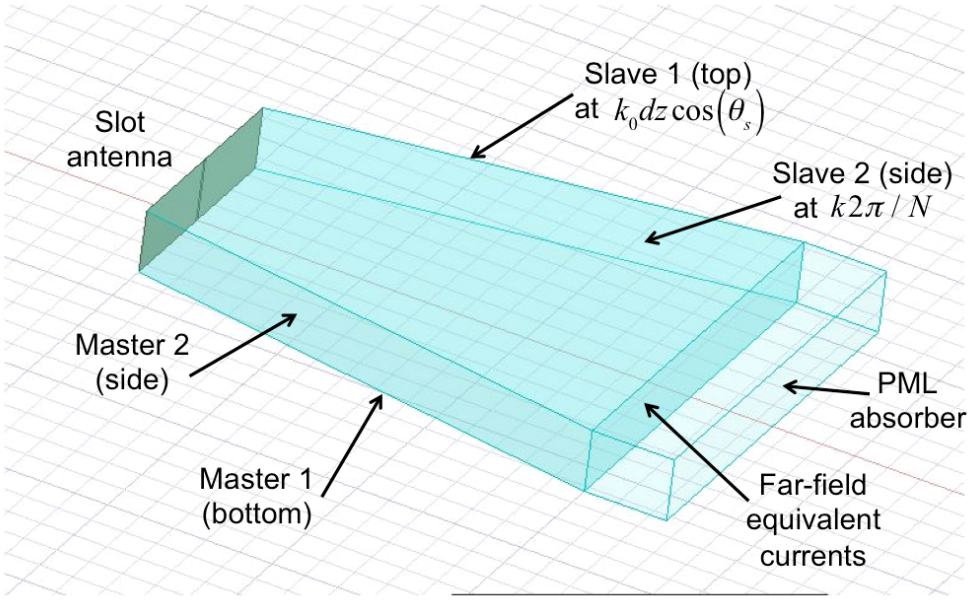

Figure 3.5: A detailed diagram of the boundary conditions on a unit-cell design in HFSS

3.3 Boundary Conditions on Radiation Surface and Limitations with Convergence Discussion

The results discussed in the last section were based off of measured data. In Chapter 4, this process will be repeated for the simulated data. Before the process is repeated for simulated data, it must first be discussed how to achieve the most functional simulated data possible for unit-cell analysis in HFSS. When designing cylindrical unit cell simulations it is important that convergence issues are avoided in order to accurately compare the measured data to the simulated data. At the mathematical solver end of unit cell analysis, limitations on the simulated structures occur.

In this work, HFSS is the primary field simulator used to calculate the embedded element patterns. HFSS is used to simulate a simple cylindrical phased array made up of slot antennas. The frequency used for the slot antenna simulations is 2.9GHz, at an elevation scan angle of $3°$. This differs from the experimental measured frequency of 2.76GHz for two reasons. Firstly, the antenna element is different than the CPPAR antenna element, so direct comparisons are less strict. Secondly, 2.9GHz is CPPAR's center frequency, but the measurements are made using 2.76GHz because the scan angle in elevations is dependant on the frequency used. For measured data it was important that the scan angle in elevation not be at $0°$ in order to avoid ground clutter. One element is simulated using master/slave boundary conditions and the results are processed to create an embedded element pattern in MATLAB. The method of simulation used is unit cell analysis. The cylindrical array is designed to be infinitely long to understand fundamentally how the curvature of the array is dictating the electric and magnetic fields. This physical design can be visualized in Figure 3.6. The first component in the XZ-plane is the slot antenna. This component is the one closest to the origin. The second component

in the XZ-plane is the radiation boundary. The third component in the XZ-plane is the PML, and the final face in the XZ-plane is the end of the air box. The location of the PML is moved in the y-direction during the simulations in the next section, Section 3.2.1. The PML distance is adjusted to analyze how PML distance affects convergence of the simulation.

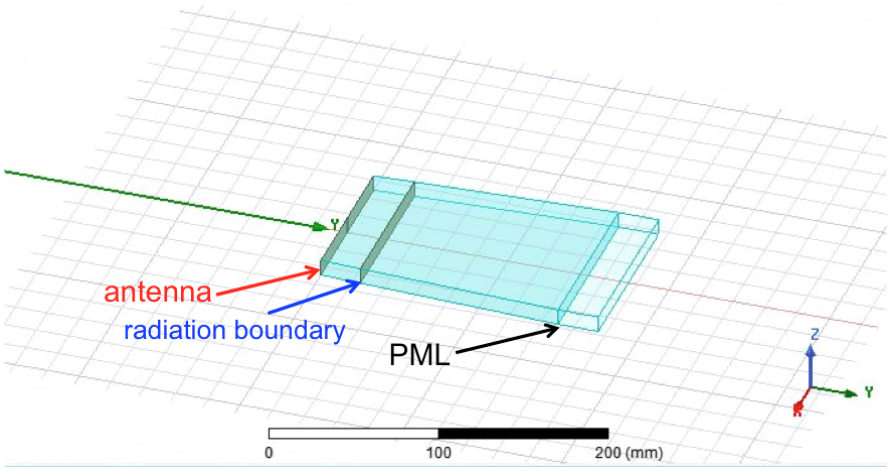

Figure 3.6: Simulation design of the base element

3.3.1 PML Distance Sensitivity Investigation

The radius of the cylinder is fixed at one meter while the length from the antenna to the PML is varied. The closer the PML is to the antenna, the more the phase mode spectrum acts uncharacteristically. The radiation surface was fixed at a quarter wavelength from the antenna while the distance from the antenna to the PML was varied from 0.45λ to 0.65λ. At a distance less than 0.45λ, the electric fields on the wedge would be difficult to observe with the PML backed-off with a radiation surface a quarter wavelength away. This means the radiation surface would be 0.20λ away from the antenna, and there would not be useful information in such a small space. For this reason, 0.45λ was the starting point for the simulation. The

results, shown in Figures 3.7 and 3.8, showed the phase mode spectrum and phase modes behaving mostly as expected, meaning the phase modes had similar values in the same range for each PML placement.

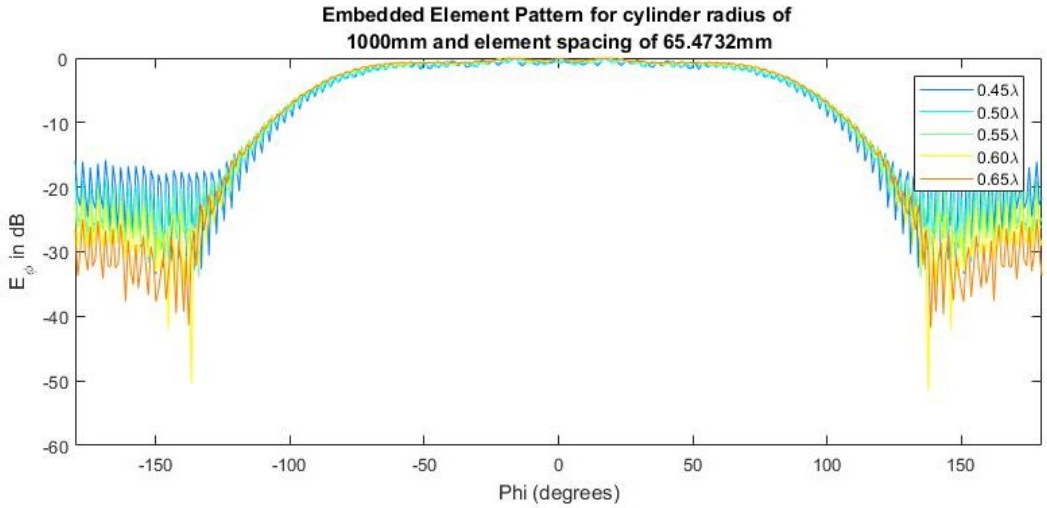

Figure 3.7: E_ϕ field for each PML position, see figure below for legend

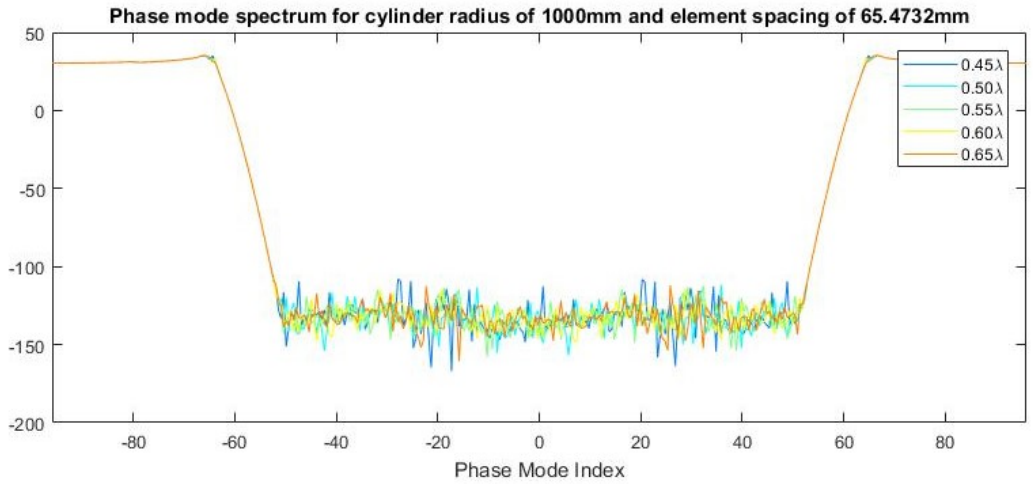

Figure 3.8: Phase mode spectrum pattern for each PML distance from the antenna

However, as seen in Figure 3.8 and Figure 3.9, convergence issues did appear significantly around phase modes -65 and 65, when the PML was 0.65λ or less away

from the antenna (and a quarter wavelength away from the radiation surface). Each placement of the PML showed slight non-convergence, the 0.45λ or less case is being emphasized to show the more exaggerated effects non-convergence has on the E_ϕ patterns. Another simulation of this type was executed to find the approximate length where the convergence issues are no longer present. The distance from the antenna to PML was extended up to 1.1λ in increments of 10mm. When the PML is 0.60λ and 0.70λ away there is a small amount of non-convergence at the specified phase modes, which creates ripples in the radiation pattern, as seen in Figures 3.10 and 3.11. Once the PML is 0.80λ away from the antenna the convergence issues are cleaned up and the radiation pattern does not have ripples. This is based off of the simulation with a simple slot antenna; with more complex antenna designs, it is recommended that the PML be placed at a greater distance, of at least 2λ, away from the antenna.

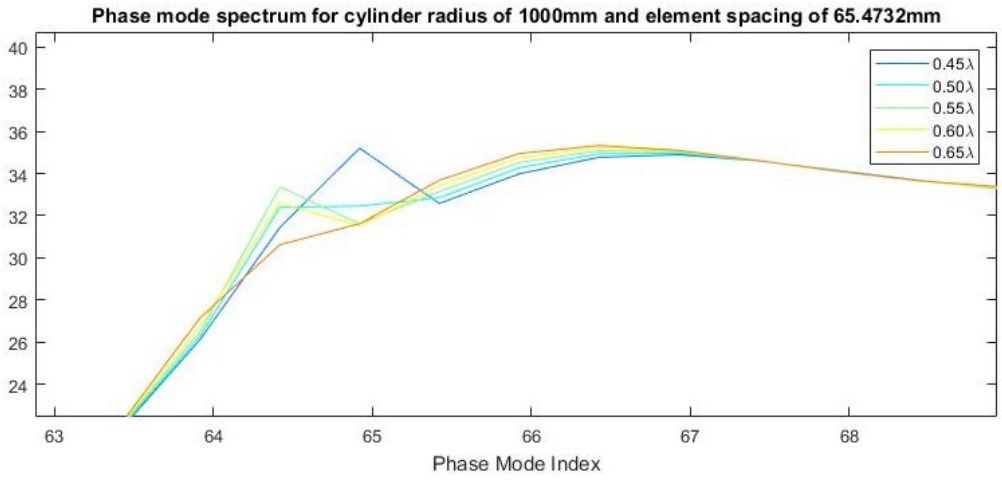

Figure 3.9: Detailed view of non-convergence areas in phase mode spectrum pattern for each PML distance

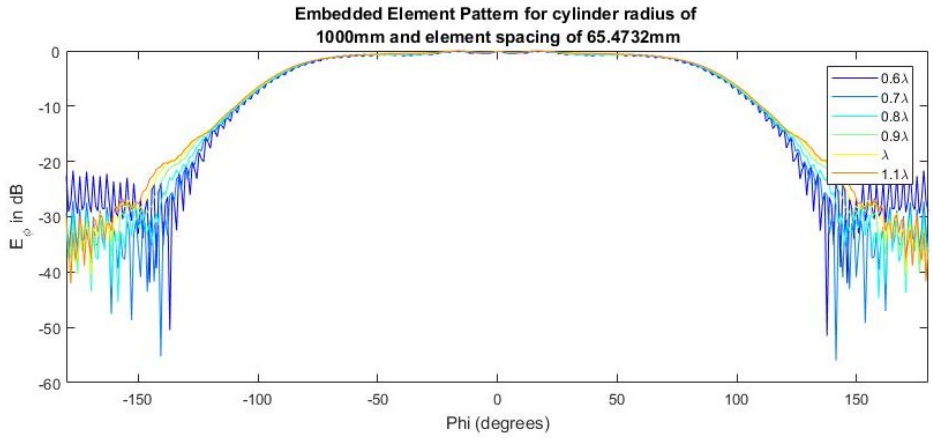

Figure 3.10: E_ϕ field patterns for each extended PML distance from the antenna

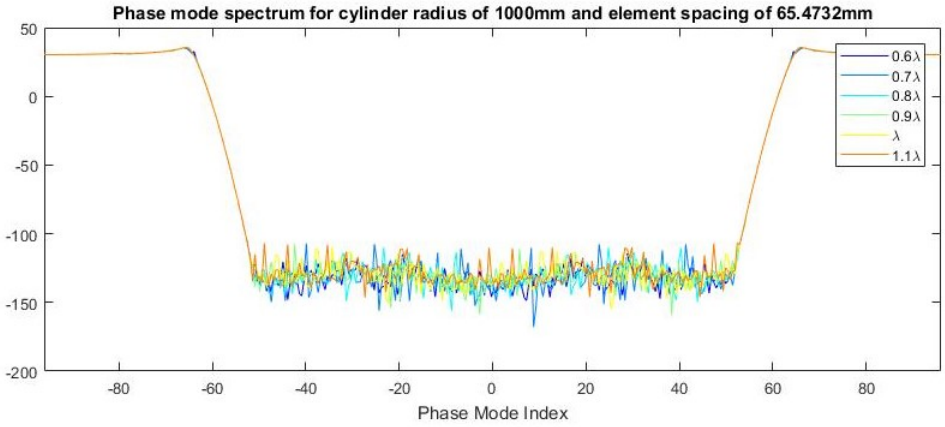

Figure 3.11: Phase mode patterns for each extended PML distance from the antenna

3.3.2 Electric Fields

Finally, the electric fields on the wedge component were observed for different phase modes and different PML distances. The phase modes included are 65 and 80. Phase mode 65 is included because this is the phase mode where non-convergence begins to appear, as seen in Figure 3.9. Phase mode 80 is included as a baseline. It can be seen in Figure 3.8 that the convergence issues, regardless of PML placement, no longer appear in this region. It is expected that the fields for phase mode 80 should look similar regardless of PML placement. In this sense, PML 80 is the control group. The phase was chosen to be 30 degrees for visual purposes. The PML distances included are 0.55λ and 0.65λ. The PML distance of 0.45λ may have been more interesting than the PML distance of 0.55λ, but the 0.45λ distance would not have allowed for much room for the fields to be seen visually, with the radiation surface being so close to the antenna. So the alternative of 0.55λ was chosen to provide more room for the electric fields to be visualized.

Figure 3.12 shows the electric fields on the unit-cell wedge for phase mode 65 when the distance of the PML is set to 0.55λ away from the antenna. Next, Figure 3.13 shows the same thing, but for a PML distance for 0.65λ away from the antenna. Comparing both figures, it can be seen that the fields behave differently. The differences are especially notable in the "dark blue" region. When the PML is placed closer to the antenna, the lower threshold of 150V/m is larger compared to that of the PML distance of 65 case. In contrast to these phase mode 65 differences, Figures 3.14 and 3.15 show that the electric fields on the wedge for each phase mode 80 case look mostly similar, as expected.

It is now clear the PML distance has a realizable effect on both the electric fields, the phased mode spectrum, and far fields. Small differences may have a

large effect on the far field results. Although convergence errors resolved around a PML distance of 65 in this simulation, it is important to keep the PML distance at roughly a 2λ away to ensure convergence issues don't interfere with simulated data for more complex antenna designs. In the next section, simulated data will be manipulated through the alternating projections method in an attempt to push the back radiation levels down. When the backed-off PML is not far enough away from the antenna the undesirable effects from lack of convergence make the alternating projections results asymmetric and diminishes the ability to reduce back radiation levels.

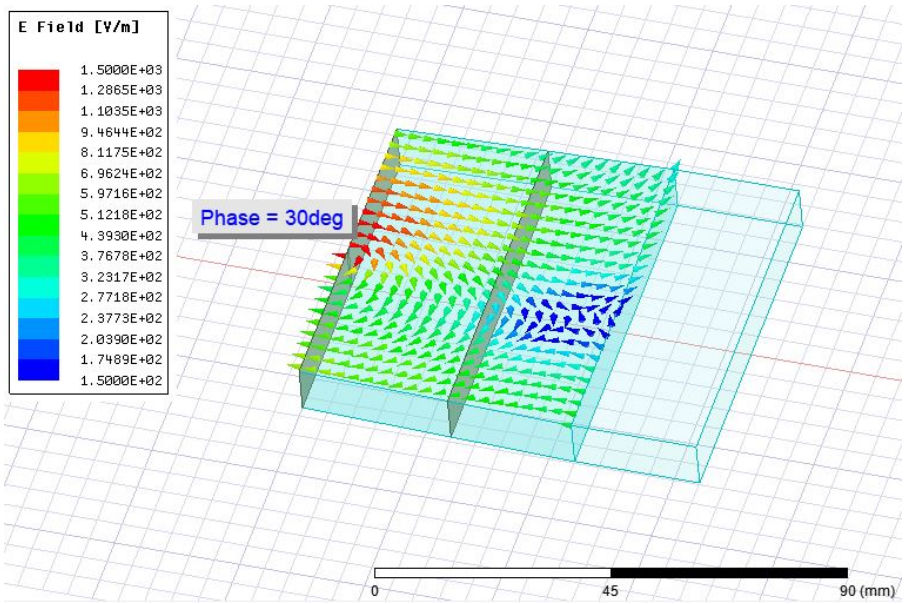

Figure 3.12: Electric field on wedge design for phase mode 65 with PML 0.55λ away from the antenna

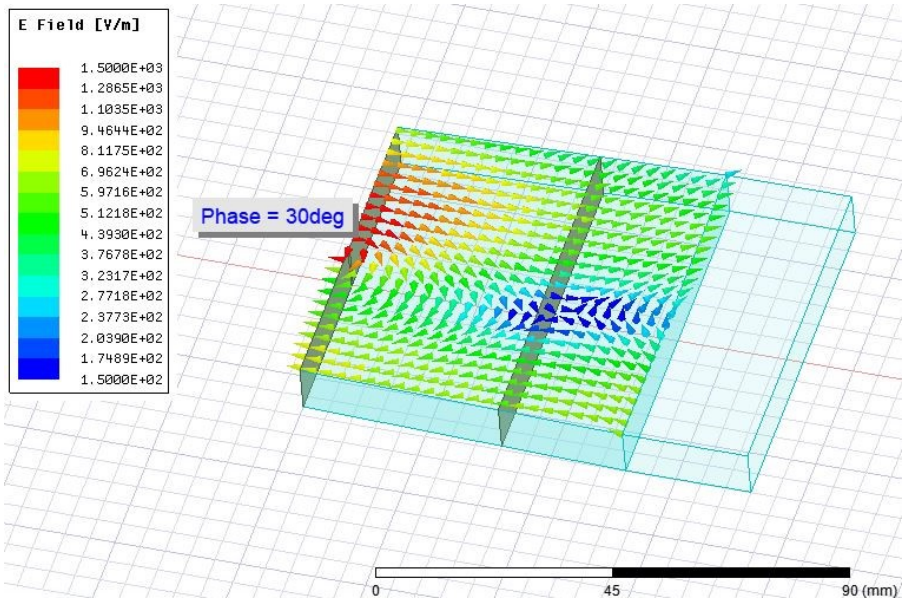

Figure 3.13: Electric field on wedge design for phase mode 65 with PML 0.65λ away from the antenna

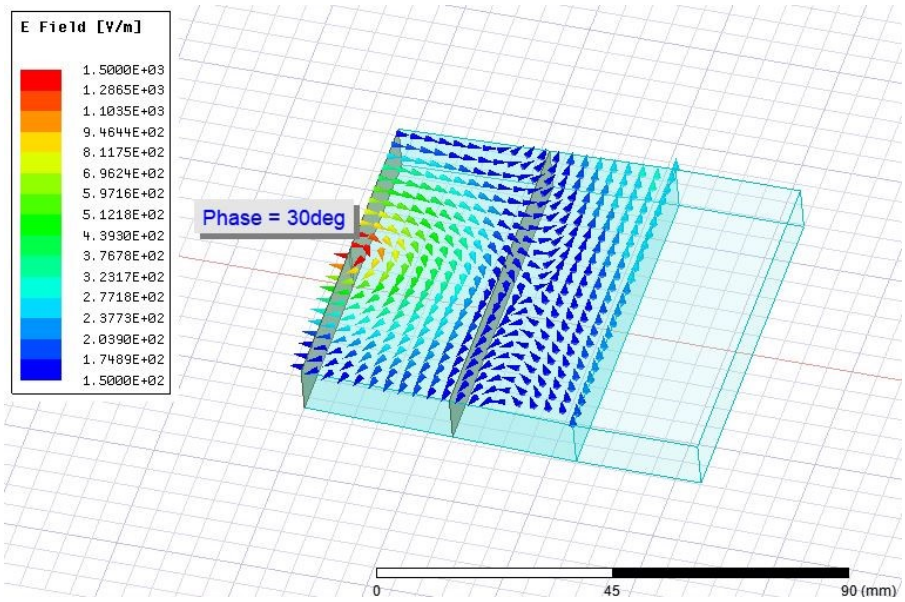

Figure 3.14: Electric field on wedge design for phase mode 80 with PML 0.55λ away from the antenna

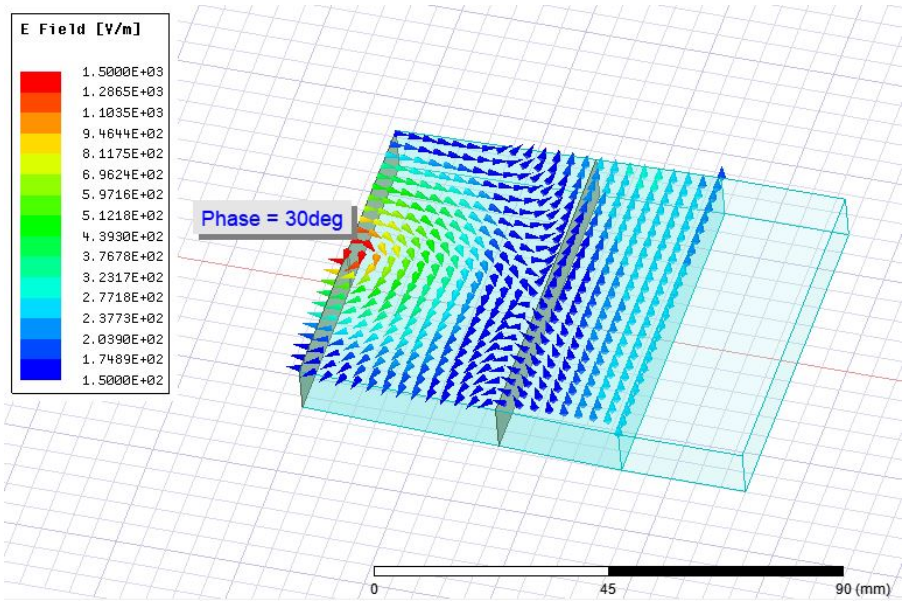

Figure 3.15: Electric field on wedge design for phase mode 80 with PML 0.65λ away from the antenna

Chapter 3 Conclusion

The method of unit-cell analysis has been explained using geometry and master slave boundary conditions, unit-cell analysis can be used for both planar and cylindrical arrays but is used for cylindrical arrays in this body of work. Unit-cell analysis allows for the simulation of large arrays with out using a large amount of computational resources, specifically, it uses N resources rather than the standard N^3 used in traditional array simulations. This method also remains accurate when compared to measured CPPAR results, and as a result is used for the simulations in this work.

It was also seen that PML placement has a significant effect on the far field radiation patterns in simulations. When the PML is positioned too close, convergence errors arise and cause the phase modes -65 and 65 to have a slight increase in magnitude compared to what is expected. If the PML is place a significant distance of 2λ or greater away from the antenna, there are no convergence issues in the simulation and data analysis can be performed, as desired. Although there was a subtle visual difference in the electromagnetic fields for the problematic phase modes when the PML is placed less than one wavelength away from the antenna, the convergence issues are still apparent in the phase mode spectrum and far field. Knowing how to properly place the PML allows this work to proceed to the next chapter, where back radiation levels on simulated data will be adjusted.

These simulated results with the simple slot antenna provide a good intuitive understanding to how convergence can effect overall pattern results. These findings can then be applied to the CPPAR demonstrator simulations in the next chapter to provide a more meaningful result.

Chapter 4

CPPAR Results

This chapter will cover the results from varying the PML placement, the alternating projections method, and the phase mode elimination method for data from a CPPAR demonstrator simulation. The purpose of this chapter is to investigate which methods have a significant impact on the far field radiation patterns, with a focus on the back radiation levels. Along with investigating each method independently, the alternating projections method and phase mode eliminating method will be combined to assess the effectiveness of combining methods.

4.1 Convergence on CPPAR Pattern Simulations

PML placement and convergence errors were covered in Chapter 3 for the slot antenna cylindrical array. Here a smaller study on PML placement and convergence is done for the CPPAR antenna. Placing the PML at a large enough distance is seen to positively affect convergence in CPPAR antenna unit cell analysis simulations as well. For the CPPAR HFSS simulations the frequency was set to 2.76GHz at an elevation angle of 3° to best match the CPPAR measurements. When the PML is set at 1.5λ away from the antenna with the PML backed off. The radiation surface is a quarter wavelength away from the PML, towards the antenna. Asymmetry occurs

significantly in the embedded element patterns at this distance. When the PML is moved to 3λ away from the antenna, the pattern becomes symmetric and convergence issues are no longer detrimental. This can be seen in Figure 4.1.

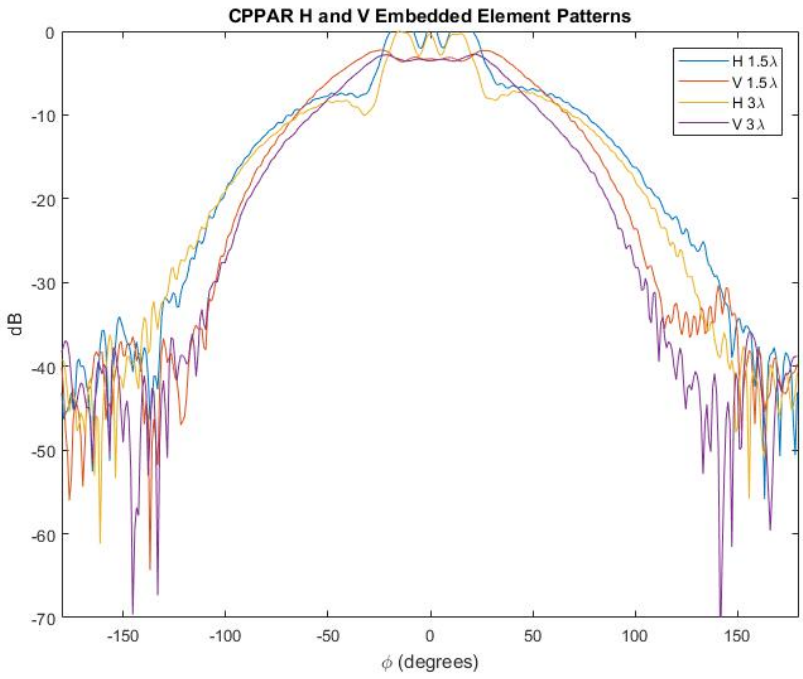

Figure 4.1: Embedded element pattern for CPPAR antenna with backed-off PML at a distance of 1.5λ and 3λ from the antenna

Next, the PML was placed at an even greater and exaggerated distance away from the antenna to see if any additional benefits in pattern quality may be achieved. For this iteration, the PML was placed at a distance of 10λ away from the antenna. This distance was chosen, as it is a exaggerated distance, and it is desired to investigate whether exaggerated PML distances cause adverse or positive effects on the embedded element pattern. It can be seen in Figure 4.2 that no adverse effects occurred due to the increase in distance. Additionally, the embedded element pattern is nearly the same as it was for the 3λ case. It is concluded that placing the PML

at a greater distance away is useful to a certain extent of distance, but exaggerated distances provide no additional benefit.

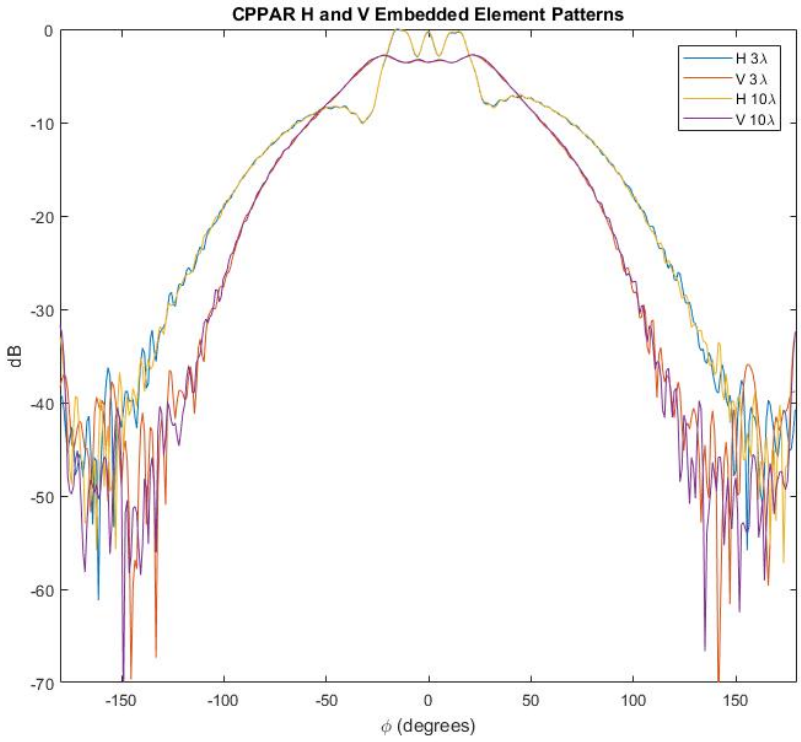

Figure 4.2: Embedded element pattern for CPPAR antenna with backed-off PML at a distance of 3λ and 10λ from the antenna

4.2 Alternating Projections Applied to a CPPAR Simulation

The alternating projections method covered above is now applied to a simulation of CPPAR created on HFSS. This simulation is designed and analyzed in the same way as in Chapter 3. Instead of using a simple slot antenna, the CPPAR antenna design is used instead, as shown in Figures 4.3 and 4.4. Figure 4.3 shows a close up view of the two-patch antenna design above the ground plane. The spacing between the patches is 5mm. Figure 4.4 shows the HFSS CPPAR simulation design includ-

ing the possible radiation boundary and PML space. The gold component facing the reader is the ground plane. This design was created in [2] and modified to meet conditions within the most recent model of HFSS.

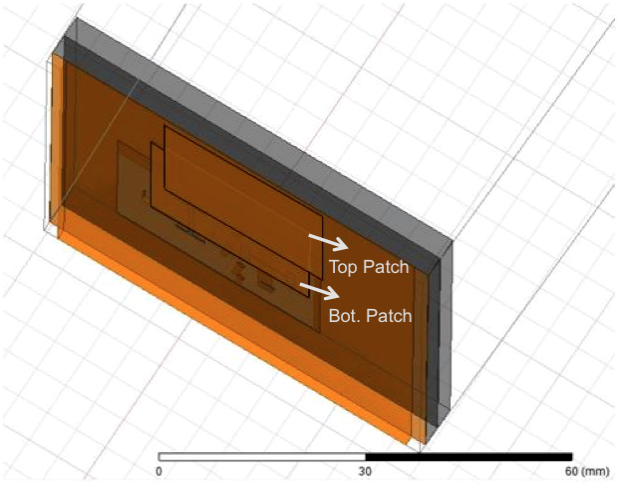

Figure 4.3: CPPAR antenna design [2]

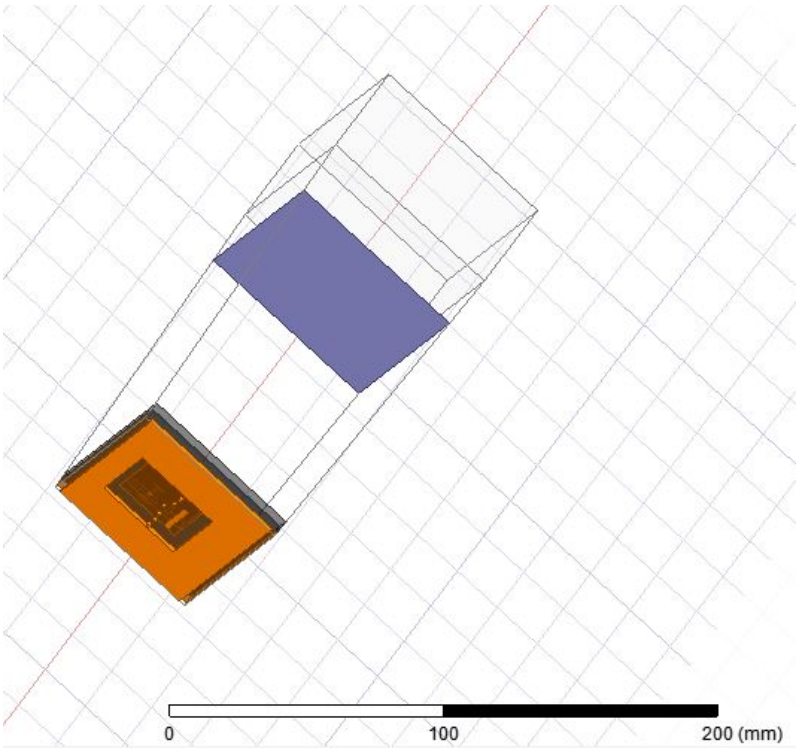

Figure 4.4: CPPAR HFSS design [2]

The far field embedded element patterns for H and V for this simulation can be seen in Figure 4.5. The embedded element patterns are the basis on which the far field is formed, and are the most important components to getting accurate results in this section. In order to form the simulated far field patterns for the entire array, the embedded element patterns shown in Figure 4.6 are circularly shifted in MATLAB and combined using the "sum" function. Finally, the alternating projections method may be applied.

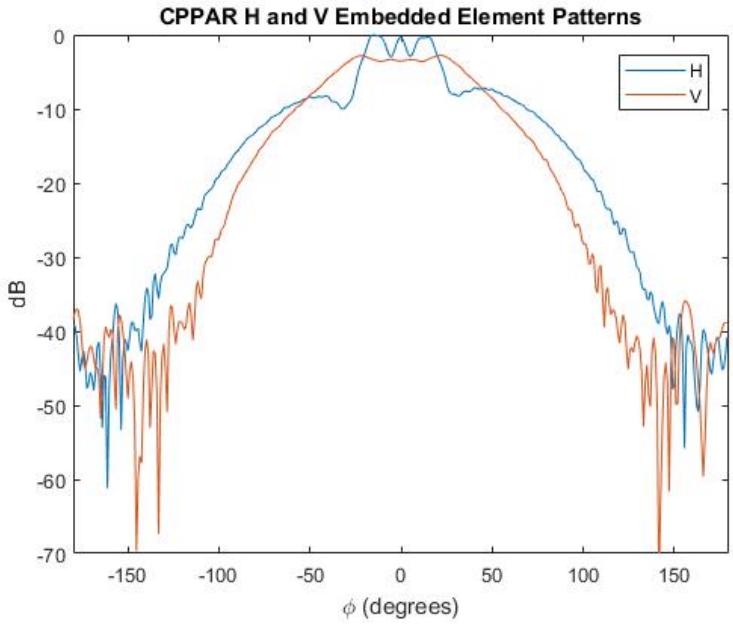

Figure 4.5: CPPAR embedded element patterns for H and V polarizations

The initial alternating projections mask and weight factor came from previous research that used this mask to manage side lobe levels on measured CPPAR data. The initial mask design and resulting alternating projection patterns and weights can be seen in Figure 4.7. The initial back radiation level of the mask is -20dB, with a weight factor of -0.6. For a more direct understanding on how the weight factor impacts the weights, the initial weights matrix is presented in Figure 4.6, where M is the value of the mask for the k^{th} column and WGT is the weighting factor. This matrix is then applied to the pseudo inverse equation. The initial weight factor of -0.6 was chosen because when the weight factor is positive, the alternating projections method does not improve the side lobe levels or the back radiation levels. When a negative number with a larger magnitude is used, the radiation pattern as a whole has a significant decrease in power. The -0.6 weighting factor is a neutral weighting factor that slightly improves side lobe levels.

$$\begin{bmatrix} (M_{1,k})^{WGT} & 0 & 0 & \cdots \\ 0 & (M_{2,k})^{WGT} & & \\ 0 & & \ddots & \\ \vdots & & & (M_{Nphi,k})^{WGT} \end{bmatrix}$$

Figure 4.6: Initial weight matrix with weighting factor, WGT

For the weight factor of -0.6, the back radiation is not reduced in any significant way. It should also be noted that the back radiation levels for the vertical polarization are better than the horizontal polarization, as expected, because creeping waves do not exist in the vertical direction. For the previous work regarding side lobe level reduction, this mask was applied to measured data, and differntaiting between each sector was important. In this work, each sector is the same due to the nearly perfect nature that simulations create. Sector 37 will be the sector used because it is broadside, there are no disconnected ("dummy") columns near by.

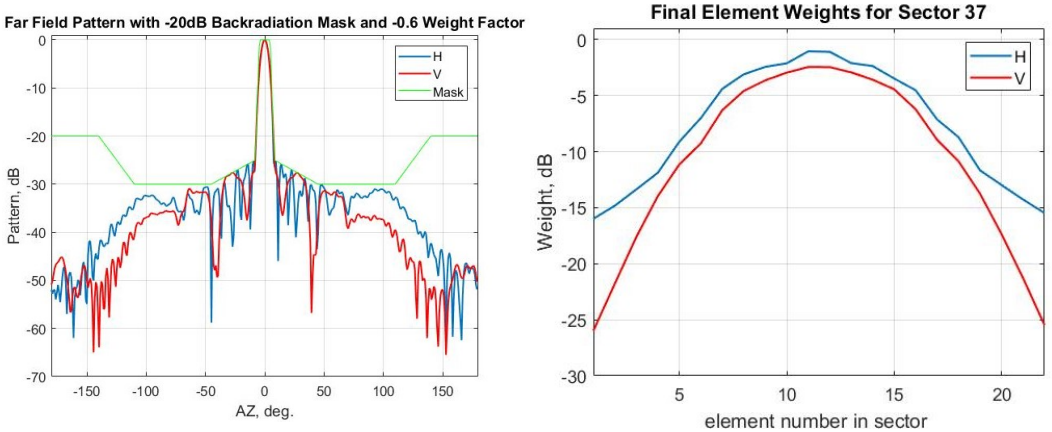

(a) Far field pattern with mask

(b) Weights

Figure 4.7: Far field radiation pattern when weight factor is set to -0.6 and the mask back radiation level is set to -20dB, and the respective final weights

The goal of this mask is to decrease the back radiation levels, so the obvious first adjustment is to decrease the value of the back radiation component of the mask in order to force the back radiation levels down. The first reduction was set at -40dB rather than -20dB, with the weight factor not adjusted. This does result in radiation levels below -40dB for ϕ values close to $-180°$, as seen in Figure 4.8, but there is not a significant decrease compared to the -20dB mask case. Next, the back portion of the mask is set even lower, to -50dB. The resulting horizontal polarization back radiation near $\phi = -180°$ is pushed down more this time, but not quite below -50dB, as seen in Figure 4.9. The vertical polarization back radiation levels remain unchanged. When the back radiation level of the mask is pushed down to -70dB, the back radiation levels drop to roughly -50dB for more values of ϕ. Also, a small portion of the horizontal back radiation drops to -50dB near $\phi = -160°$ and $\phi = 140°$. Changing the mask does have an affect on the back radiation levels for horizontally polarized waves, but not dramatically enough to bring the back radiation down to -60dB over a useful range of ϕ. Adjusting the weights manually does provide a slight improvement when the element weights towards the edges of the sector are low. Figure 4.11 shows the -50dB mask with the outer weights forced to form a truncated sector. There is slightly more back radiation below the mask than in the -50dB mask simulation in Figure 4.9.

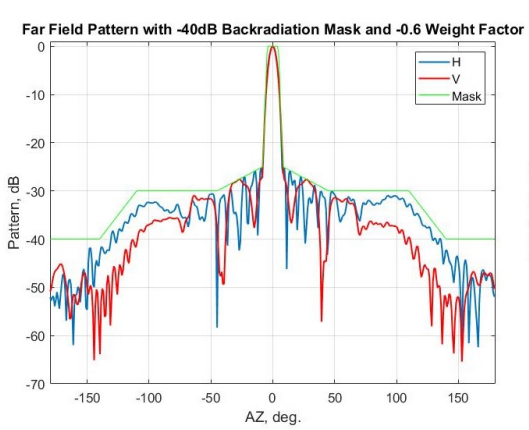

(a) Far field pattern with mask

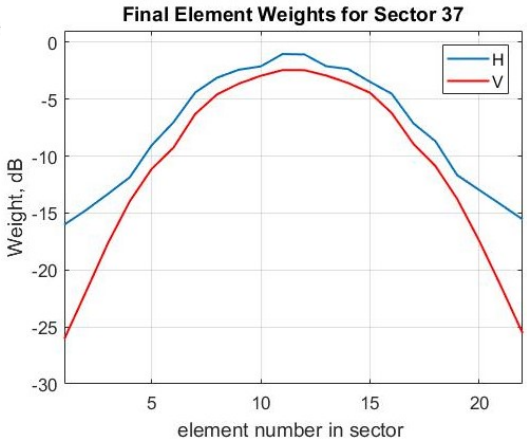

(b) Weights

Figure 4.8: Far field radiation pattern when weight factor is set to -0.6 and the mask back radiation level is set to -40dB, and the respective final weights

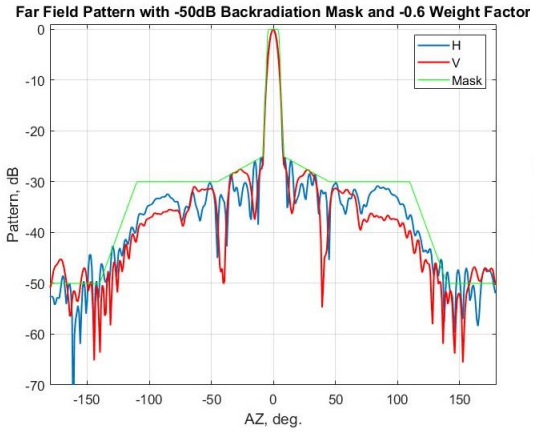

(a) Far field pattern with mask

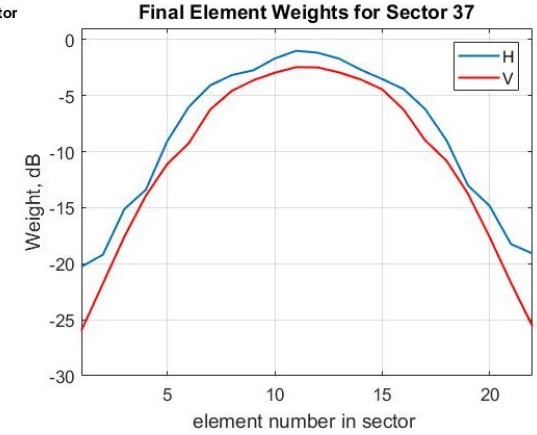

(b) Weights

Figure 4.9: Far field radiation pattern when weight factor is set to -0.6 and the mask back radiation level is set to -50dB, and the respective final weights

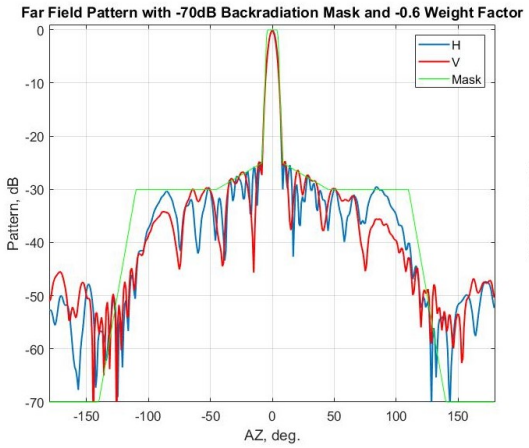

(a) Far field pattern with mask

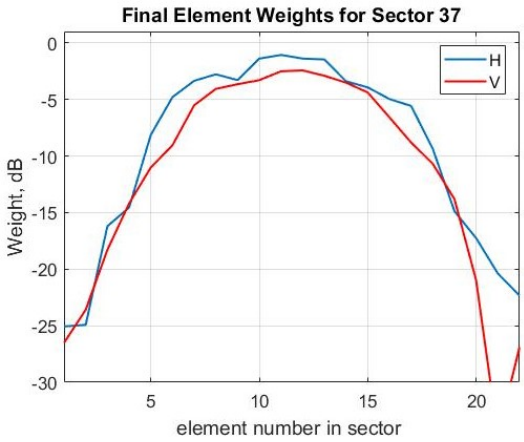

(b) Weights

Figure 4.10: Far field radiation pattern when weight factor is set to -0.6 and the mask back radiation level is set to -70dB, and the respective final weights

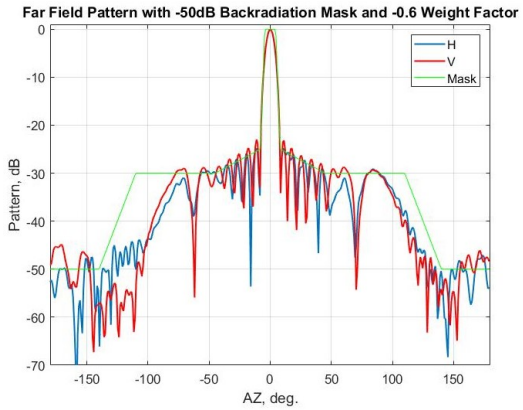

(a) Far field pattern with mask

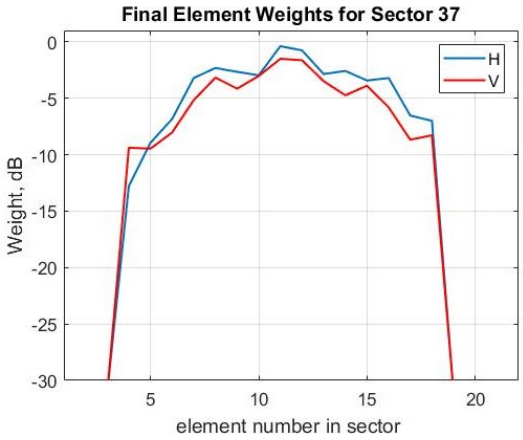

(b) Weights

Figure 4.11: Far field radiation pattern when weight factor is set to -0.6 and the mask back radiation level is set to -50dB, and the respective final weights, where the first and last three have been forced to have small values

The next adjustment made in order to bring down back radiation levels is adjusting the weighting factor, WGT. The back radiation mask level is brought back to -50dB because this threshold is enough to produce a slight decrease in back radiation levels. If any additional decrease in back radiation level is produced by

changing WGT, it would be more apparent than if the mask were set to -70dB. However, there is no change to back radiation levels, regardless of where the mask back radiation levels are set. When the back radiation level mask is set to -40dB, to see if results would be more obvious, no chang occured to the back radiation levels in this case either. Decreasing WGT reduces sidelobe levels. If WGT is set to zero, the side lobe levels are greater than the boundary set by the mask. Masking can be useful to an extent, but is limited due to the psuedoinverse matrix. The greater the difference is between the mask and the original data set, the worse recovery of the identity matrix will be, which is what the psuedoinverse matrix seeks to do. For minor adjustments the alternating projections method can provide improvement in pattern characteristics.

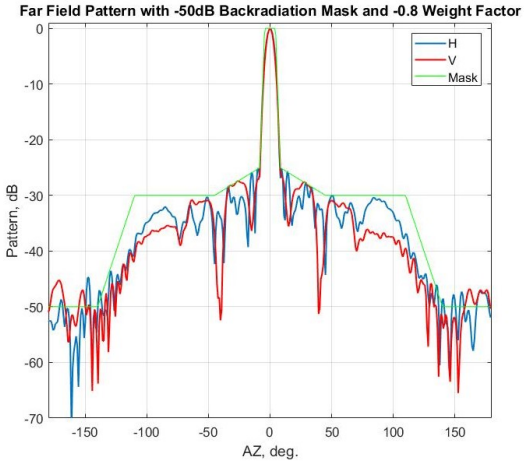

(a) Far field pattern with mask

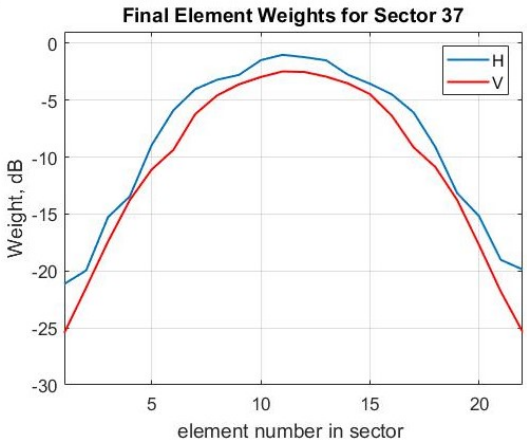

(b) Weights

Figure 4.12: Far field radiation pattern when weight factor is set to -0.8 and the mask back radiation level is set to -50dB, and the respective final weights

4.3 Study on Phase Mode Filtering and Convergence Without Alternating Projections

Next, the phase mode elimination will be explored for the CPPAR demonstrator simulation. The phase mode elimination in this section is performed prior to any alternating projections manipulation, to see what can be accomplished through only phase mode elimination for the simulated results. The different maximum phase modes chosen were 79, 63, and 56, and 30 to match the phase mode elimination performed on the measured data in Section 2.4. Phase mode 63 represents a phase mode that corresponds to a creeping wave that is traveling near the speed of light. Phase modes near the region of 30 represent surface wave related phase modes that introduce spectral content. Additionally, eliminating all phase modes greater than 35 was chosen to show a result discussed below.

It can be seen in Figure 4.13, not many changes occur when eliminating so few phase modes; this is expected. Figure 4.14 shows a maximum phase mode of 63. The results do not match the results in Section 2.4., where the phase mode elimination is performed on measured data. In section 2.4., eliminating phase modes greater than 63 resulted in a significant drop in back radiation levels. Here, no significant change occurs. It is evident the phase mode spectrum looks quite different for the simulated and measured data, and as a consequence eliminating the same phase modes provides different results. The CPPAR demonstrator is made up of numerous layers, while the HFSS CPPAR antenna has the same number of layers as the design given in Figure 2.12. This may be responsible for the different results. Figure 4.15 shows that no significant changes occur for eliminating phase modes greater than 56. However, when eliminating phase modes near 35, a minor drop in back radiation level occurs, as seen in Figure 4.16. Finally, once phase modes

greater than 30 are eliminated, the pattern becomes “cleaner” and more predictable, as seen in Figure 4.17. This is similar to the results of eliminating phase modes corresponding to cylindrical surface wave content in Section 2.4.

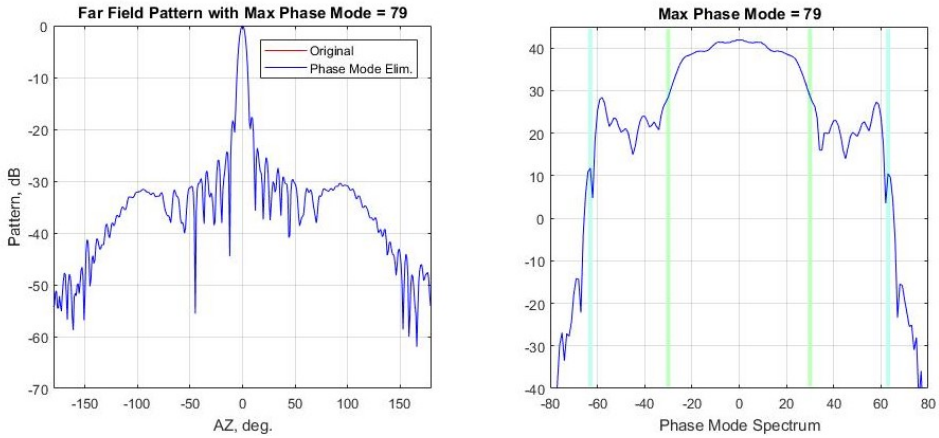

Figure 4.13: Resulting far field pattern from elimination of phase modes greater than 79 (left) and phase mode spectrum (right) where the blue vertical lines represent creeping wave content and green vertical lines represent surface wave content

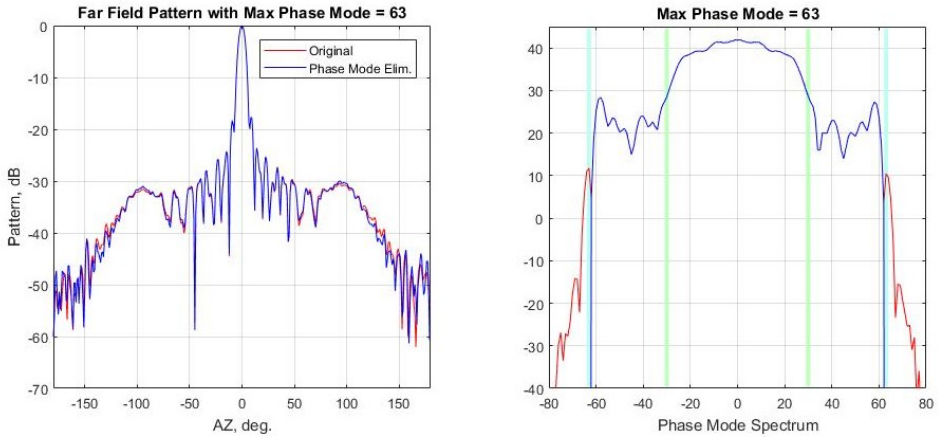

Figure 4.14: Resulting far field pattern from elimination of phase modes greater than 63 (left) and phase mode spectrum (right) where the blue vertical lines represent creeping wave content and green vertical lines represent surface wave content

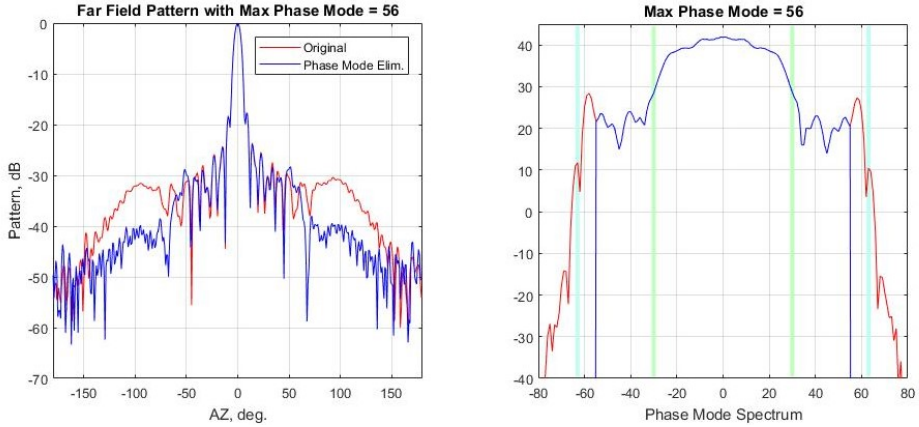

Figure 4.15: Resulting far field pattern from elimination of phase modes greater than 56 (left) and phase mode spectrum (right) where the blue vertical lines represent creeping wave content and green vertical lines represent surface wave content

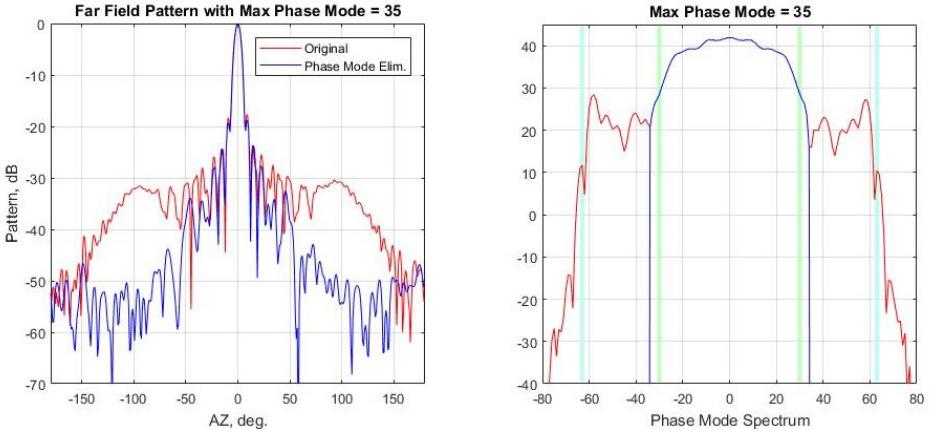

Figure 4.16: Resulting far field pattern from elimination of phase modes greater than 35 (left) and phase mode spectrum (right) where the blue vertical lines represent creeping wave content and green vertical lines represent surface wave content

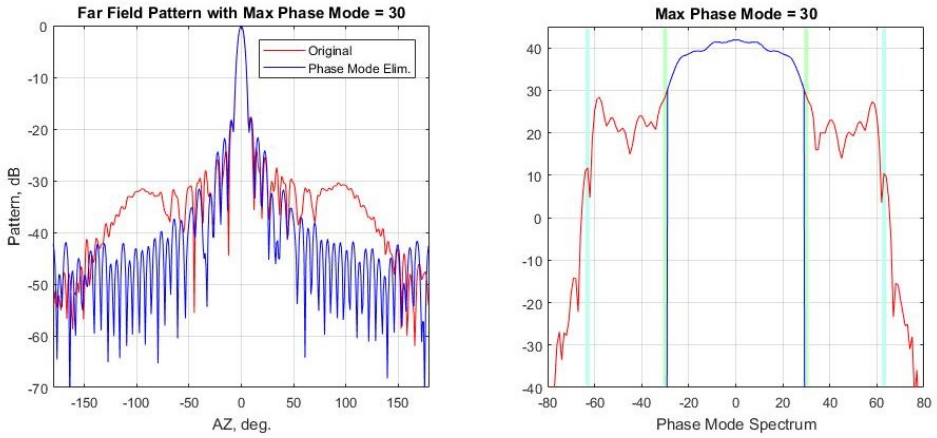

Figure 4.17: Resulting far field pattern from elimination of phase modes greater than 30 (left) and phase mode spectrum (right) where the blue vertical lines represent creeping wave content and green vertical lines represent surface wave content

4.4 Phase Mode Elimination Method Combined with Alternating Projections

Combining the phase mode elimination methods used in Section 2.4 with alternating projections methods may provide useful results in decreasing back radiation levels. This work will cover two different methods of combining these two techniques. The first experiment will apply the alternating projections method to the raw data first, and then apply the phase mode elimination method. The second experiment will reverse this order; the phase mode elimination method will be applied first, followed by the alternating projections method.

4.4.1 Alternating Projections Application followed by Phase Mode Elimination

For the experiment, a mask of -55dB with a weighting factor of -0.6 was applied first. Then different phase modes were eliminated to observe the effects on back radiation and overall pattern shape. The different maximum phase modes chosen were 79, 63, and 56 to match the phase mode elimination performed on measured data in Section 2.4., and an additional maximum of 21 was performed as well. The first phase mode elimination removed all phase modes larger than 79, as seen in Figure 4.18. This provided no difference to the far field patterns, as expected. The next phase mode elimination removed all phase modes larger than 63, as seen in Figure 4.19. Based on the information from Section 2.4., it was expected that the back radiation levels would decrease due to the phase modes near the speed of light being eliminated. However, this did not occur and very few changes were made to the far field pattern. Next, all phase modes larger than 56 were removed, as seen in Figure 4.20. Very few changes to the back radiation levels in the far field pattern were made, but the side lobe levels did drop significantly when eliminating phase modes larger than 56, which is beneficial. When the maximum phase mode level is set to 35, there is a small drop in back radiation levels. The back radiation levels are pushed down to -50dB, as seen in Figure 4.21. It seems that when the main "curve" of the phase mode spectrum begins to be eliminated, the back radiation levels drop. Similar to the previous section, for phase mode 35, which is near the main curve of the phase mode spectrum. Finally, all phase modes larger than 30 were removed, as seen in Figure 4.22. The results for this elimination matches the results from Section 2.4 where the phase modes matched the surface wave content were eliminated. The pattern is "cleaned up," and more predictable than before the

surface waves were eliminated.

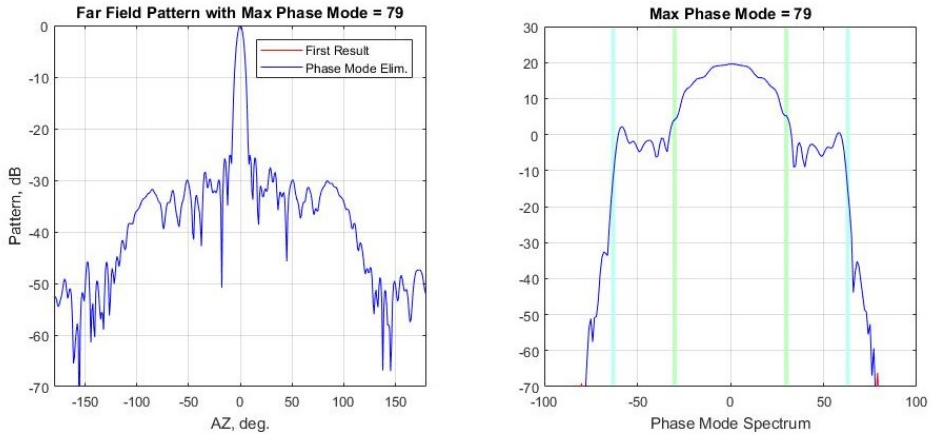

Figure 4.18: Resulting far field pattern from alternating projections combined with phase mode elimination of phase modes greater than 79 (left) and phase mode spectrum (right) where the blue vertical lines represent creeping wave content and green vertical lines represent surface wave content

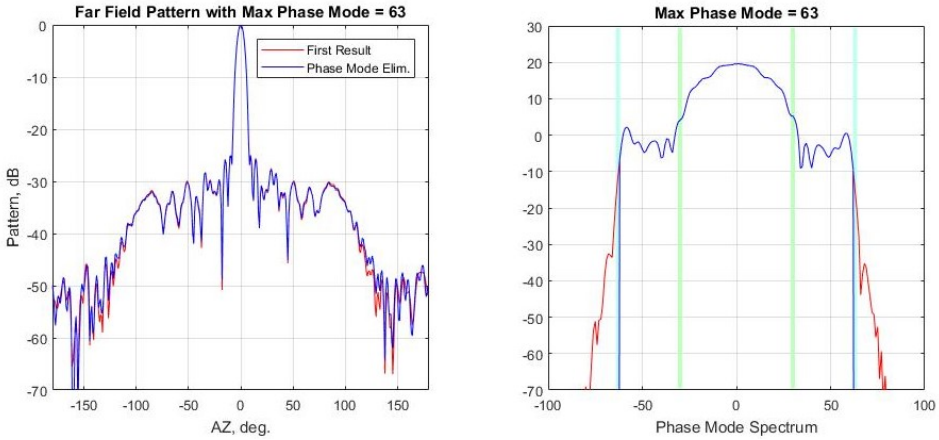

Figure 4.19: Resulting far field pattern from alternating projections combined with phase mode elimination of phase modes greater than 63 (left) and phase mode spectrum (right) where the blue vertical lines represent creeping wave content and green vertical lines represent surface wave content

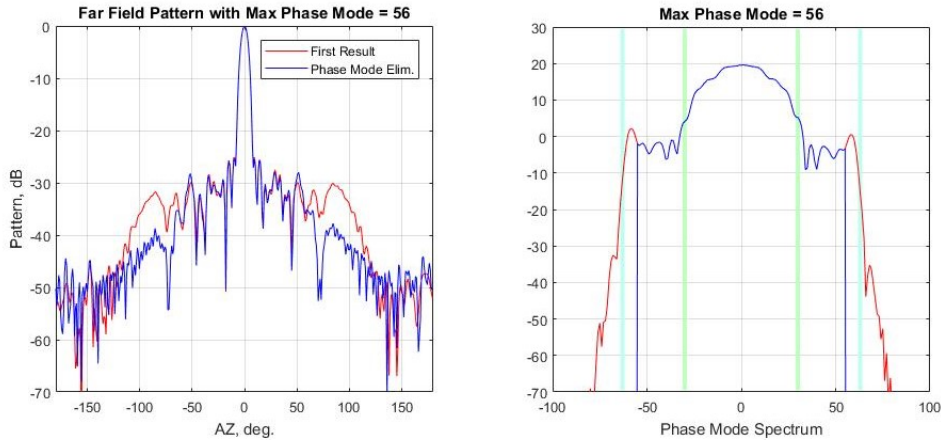

Figure 4.20: Resulting far field pattern from alternating projections combined with phase mode elimination of phase modes greater than 56 (left) and phase mode spectrum (right) where the blue vertical lines represent creeping wave content and green vertical lines represent surface wave content

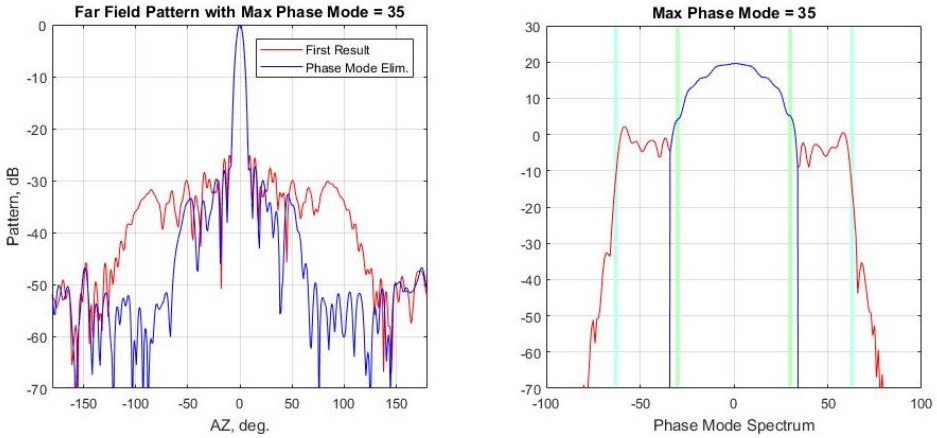

Figure 4.21: Resulting far field pattern from alternating projections combined with phase mode elimination of phase modes greater than 35 (left) and phase mode spectrum (right) where the blue vertical lines represent creeping wave content and green vertical lines represent surface wave content

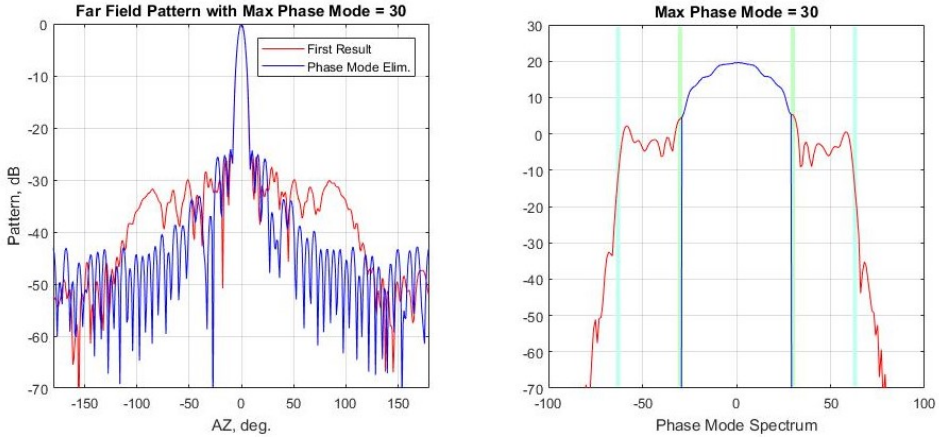

Figure 4.22: Resulting far field pattern from alternating projections combined with phase mode elimination of phase modes greater than 30 (left) and phase mode spectrum (right) where the blue vertical lines represent creeping wave content and green vertical lines represent surface wave content

4.4.2 Phase Mode Elimination Application Followed by Alternating Projections Method

This subsection reverse the reverse of the previous section. First the phase mode elimination method is applied. Once this is accomplished, the alternating projection method is applied using a mask with back radiation levels of -55dB. This mask was chosen to attempt to push the levels down with out attempting to push the mask levels too far. The maximum phase modes shown are 79, 63, 56, and 35 for the same reasons in the previous subsection. For all four variations, the final resulting back radiation levels were just below -50dB for the most part. The mask did improve the phase mode elimination results when the maximum phase mode was 63 and 56. Prior to the alternating projection mask being applied, the back radiation levels were above -50dB. Once the mask was applied the levels were brought down to -50dB. The alternating projections method helped only slightly for the maximum phase

mode of 79 case and did not help for the maximum phase mode of 35 case. When the maximum phase mode was set to 35 the back radiation levels were already -50dB. As seen previously, the alternating projections method can be helpful to an extent, but once the levels reach -50dB the alternating projections method seems to be limited by the psuedoinverse.

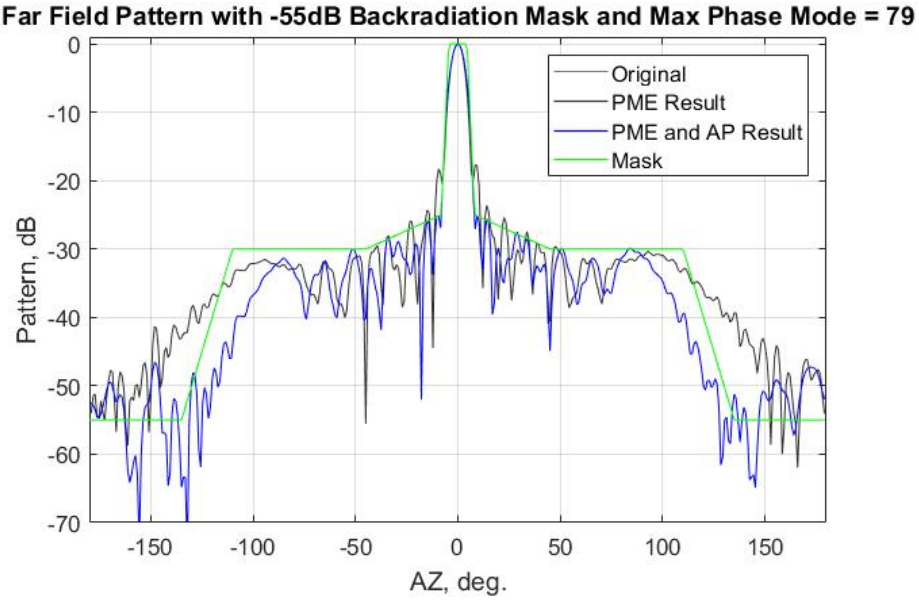

Figure 4.23: Combination of phase mode elimination for maximum phase mode of 79 followed by the Alternating projections method with a mask of -55dB

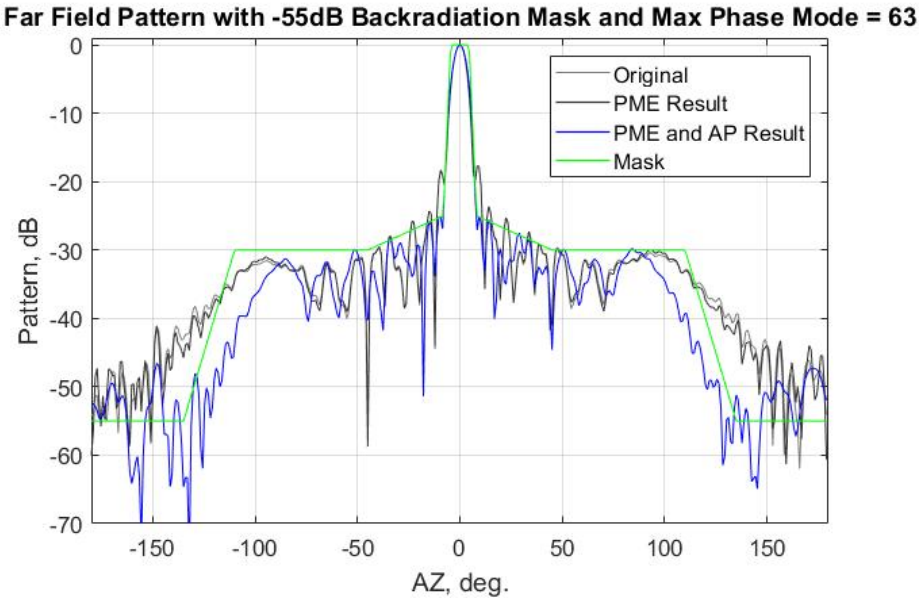

Figure 4.24: Combination of phase mode elimination for maximum phase mode of 63 followed by the Alternating projections method with a mask of -55dB

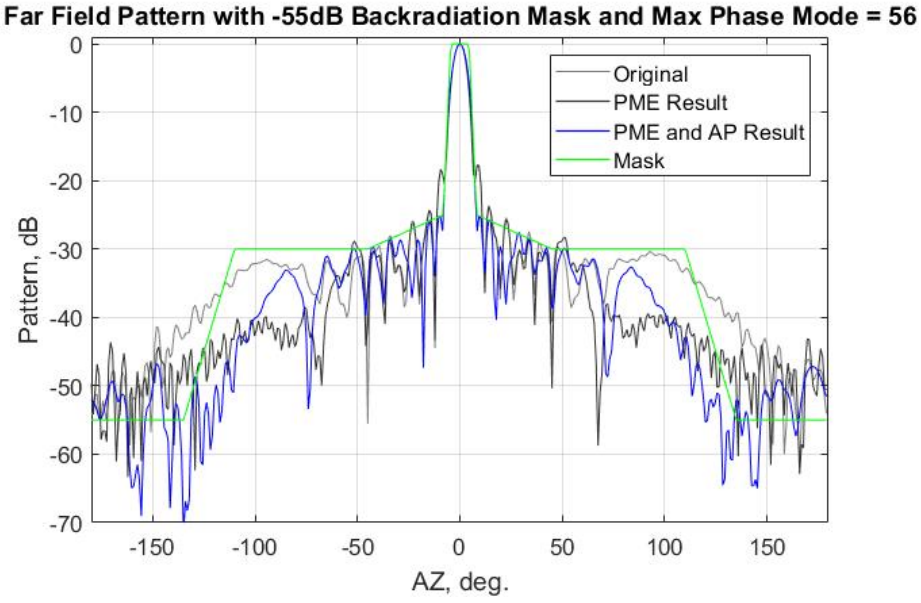

Figure 4.25: Combination of phase mode elimination for maximum phase mode of 56 followed by the Alternating projections method with a mask of -55dB

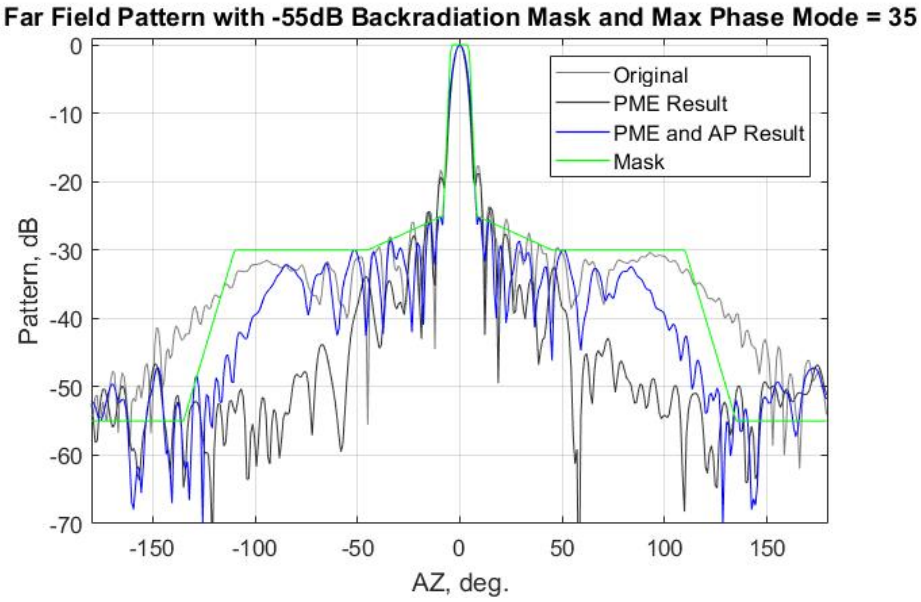

Figure 4.26: Combination of phase mode elimination for maximum phase mode of 35 followed by the Alternating projections method with a mask of -55dB

Chapter 4 Conclusion

The alternating projections method on its own does not provide dramatic improvements. Minor adjustments are made but not enough to meet the meteorological -80dB front-to-back isolation requirement. This is at least partially due to the nature of the pseudo-inverse matrix. The larger the least square error is, the less well the pseudo-inverse recovers the identity matrix. This means if the difference between the mask and the raw data is large, the identity matrix wont be recovered well and there will not be a drastic change in the final results. This makes alternating projections a strong method for making minor changes to the radiation pattern, but a less productive method for making dramatic changes.

The phase mode elimination method performed on the simulated CPPAR data does not behave exactly as expected, compared to the results from Section 2.4. for

phase mode elimination on measured data. Similar effects do occur, the back radiation levels can be decreased, but much less dramatically than the results from section 2.4. The back radiation level also decreases at a different maximum phase mode than the previous results. Thus, this component of the experiment was not successful in replication the results in Section 2.4. This may be due to the differences in the construction of the actual CPPAR demonstrator antennas and the simulated antennas. The CPPAR demonstrator antenna has a greater number of substrate layers than the HFSS CPPAR antenna design.

Combining the alternating projections method followed phase mode elimination provided no additional improvement than the phase mode elimination method alone. When the phase mode elimination was applied first, followed by the alternating projections method. A small amount of improvement was made for the maximum phase mode cases of 56 and 63. This was not the initial expected result, but may be a result of the limitations on the alternating projections method and the level of difficulty it takes to decrease signals past the -50dB level. This limitation explains why performing the alternating projections second is helpful, because the back radiation levels are slightly increased when applying the phase mode elimination method for phase modes 56 and 63. It was seen in both Section 4.3 and 4.4 that when the phase modes up to and near the main curve of the phase mode spectrum are eliminated, the back radiation levels drop slightly. This does not match the results from Section 2.4., but may provide a doorway to future work investigating different phase mode spectrum shapes for the phase mode elimination method on cylindrical arrays.

Chapter 5

Conclusion and Future Work

There are many benefits to using cylindrical arrays; such as fast update times, $360°$s of azimuthal scanning range, and no bias errors due to steering away from the principal plane compared to planar arrays. These benefits have potential to outweigh the unique challenge of creeping waves that are presented by cylindrical arrays, if creeping wave effects can be mitigated. This thesis sought to bring back radiation levels below a -80dB threshold, which is set by meteorological standards. Although the goal of -80dB was not achieved, useful tools and information have been found.

One of the most important aspects to this thesis is an approachable and compact explanation of creeping waves as a concept, and how they are mathematically modeled in the complex plane using Green's functions. This explanation provides a concrete understanding of the difference between cylindrical surface waves and cylindrical creeping waves, which is commonly misunderstood. Creeping waves are ever present, while cylindrical surface waves are more maneuverable by changing the properties of the substrate and cylinder radius.

The next important item covered in this thesis is how the elimination of certain phase modes can affect the far field pattern and back radiation levels. This is a strong gateway to future work, where it should be mathematically investigated at a fundamental level why eliminating certain phase modes has this effect. Similar re-

sults were observed in this thesis to the measured results found in Section 2.4. Phase mode elimination did achieve a drop in back radiation levels when the maximum phase mode was 35. Phase mode elimination combined with the alternating projections method also provided a slight drop in back radiation when the maximum phase mode was 35. Both drops occur when the maximum phase mode is set to be near the main curve of the phase mode spectrum. This drop in back radiation levels occurred for phase mode 63 for the measured data phase mode elimination method. The different maximum phase mode locations for back radiation decreasing may provide a doorway to future work investigating different phase mode spectrum shapes for the phase mode elimination method on cylindrical arrays. Additionally, once enough phase modes are eliminated for the simulated results, the pattern begins to become more predictable. This is similar to the measured phase mode elimination results but for slightly different maximum phase modes. A relationship seems to exist, but a deeper investigation should be done with various antenna types and various element spacing for future work.

Thirdly, it is known that PMLs can provide accurate results by emulating reflection free radiation. The PML emulates reflection free radiation by absorbing the electromagnetic fields acting on the boundary. It has been also shown in [2] that backing-off the PML with a radiation boundary 25mm away from the PML can provide even better results. This thesis expands upon accurate PML usage by observing convergence when the PML is placed at different distances from the antenna. It was found that if the PML is too close, significant convergence errors occur and disrupt the far field radiation pattern. For safe PML placement, the PML should be placed at least two wavelengths away from the antenna. Future work may be explored for PML placement, but does not seem very necessary. At most, it is simply recommended that a PML parametric sweep be performed and analyzed

prior to all cylindrical array unit cell simulations, to ensure the PML is placed far enough away.

Finally, an alternating projections method was tested to see if this could bring the back radiation levels down. The method was able to minimally adjust the back radiation levels, but not enough to bring them down more than -55dB. It is possible this method could provide significant results, but the pseudo-inverse matrix has limits to what it can absolve. The greater the difference between the mask and the raw data, the more loosely fit the pseudo-inverse matrix will be, leading to less dramatic adjustments.

References

[1] D. Zrnic, J. Kimpel, D. Forsyth, A. Shapiro, G. Crain, R. Ferek, J. Heimmer, W. Benner, T. McNellis, and R. Vogt, "Agile-beam phased array radar for weather observations", *Bulletin of the American Meteorological Society*, vol. 88, no. 11, pp. 1753–1766, 2007.

[2] C. Fulton, "Phase mode analysis of a cylindrical polarimetric phased array antenna", in *Proc. Allerton Antenna Appl. Symp.*, 2014.

[3] M. E. Weber, J. Y. Cho, and H. G. Thomas, "Command and control for multifunction phased array radar", *IEEE Transactions on Geoscience and Remote Sensing*, vol. 55, no. 10, pp. 5899–5912, 2017.

[4] G. Zhang, R. J. Doviak, D. S. Zrnic, J. Crain, D. Staiman, and Y. Al-Rashid, "Phased array radar polarimetry for weather sensing: A theoretical formulation for bias corrections", *IEEE transactions on geoscience and remote sensing*, vol. 47, no. 11, pp. 3679–3689, 2009.

[5] M. Galletti and D. S. Zrnic, "Bias in copolar correlation coefficient caused by antenna radiation patterns", *IEEE Transactions on Geoscience and Remote Sensing*, vol. 49, no. 6, pp. 2274–2280, 2011.

[6] D. Zrnić, R. Doviak, V. Melnikov, and I. Ivić, "Signal design to suppress coupling in the polarimetric phased array radar", *Journal of Atmospheric and Oceanic Technology*, vol. 31, no. 5, pp. 1063–1077, 2014.

[7] I. R. Ivić, "Phase code to mitigate the copolar correlation coefficient bias in ppar weather radar", *IEEE Transactions on Geoscience and Remote Sensing*, vol. 55, no. 4, pp. 2144–2166, 2017.

[8] K. J. Sperzel and C. J. Fulton, "Mechanisms for generation and suppression of creeping waves on a radiating cylindrical structure", *2017 Antenna Applications Symposium, Monticello, Illinois*, vol. 63, 2017.

[9] G. Zhang, R. J. Doviak, D. S. Zrnić, R. Palmer, L. Lei, and Y. Al-Rashid, "Polarimetric phased-array radar for weather measurement: A planar or cylindrical configuration?", *Journal of Atmospheric and Oceanic Technology*, vol. 28, no. 1, pp. 63–73, 2011.

[10] R. Paknys and D. R. Jackson, "The relation between creeping waves, leaky waves, and surface waves", *IEEE Transactions on antennas and propagation*, vol. 53, no. 3, pp. 898–907, 2005.

[11] J.-C. Sureau and A. Hessel, "Element pattern for circular arrays of waveguide-fed axial slits on large conducting cylinders", *IEEE Transactions on Antennas and Propagation*, vol. 19, no. 1, pp. 64–74, 1971.

[12] R. J. Mailloux, *Phased array antenna handbook*. Artech house, 2017.

[13] R. E. Collin, *Field theory of guided waves*. McGraw-Hill, 1960.

[14] C. A. Balanis, *Advanced engineering electromagnetics*. John Wiley & Sons, 1999.

[15] P. C. Clemmow, *The Plane Wave Spectrum Representation of Electromagnetic Fields: International Series of Monographs in Electromagnetic Waves*. Elsevier, 2013.

[16] J. W. Brown, R. V. Churchill, *et al.*, *Complex variables and applications*. Boston: McGraw-Hill Higher Education, 2009.

[17] A. K. Bhattacharyya, "An accurate model for finite array patterns based on floquet modal theory", *IEEE Transactions on Antennas and Propagation*, vol. 63, no. 3, pp. 1040–1047, 2015.

[18] ——, *Phased array antennas: Floquet analysis, synthesis, BFNs and active array systems*. John Wiley & Sons, 2006, vol. 179.

[19] H. Guodong, W. Wei, and D. Biao, "Perturbation alternating projections method for pattern synthesis of phased array antenna", in *Proceedings of 2012 5th Global Symposium on Millimeter-Waves*, IEEE, 2012, pp. 385–388.

[20] S. Karimkashi, G. Zhang, R. Kelley, J. Meier, R. Palmer, A. Zahrai, R. J. Doviak, and D. S. Zrnic, "Cylindrical polarimetric phased array radar demonstrator: Design and analysis of a frequency scanning antenna array", in *2013*

IEEE International Symposium on Phased Array Systems and Technology, IEEE, 2013, pp. 477–480.

[21] C. Fulton, J. L. Salazar, Y. Zhang, G. Zhang, R. Kelly, J. Meier, M. McCord, D. Schmidt, A. D. Byrd, L. M. Bhowmik, *et al.*, "Cylindrical polarimetric phased array radar: Beamforming and calibration for weather applications", *IEEE Transactions on Geoscience and Remote Sensing*, vol. 55, no. 5, pp. 2827–2841, 2017.

[22] R. J. Mailloux, *Phased array antenna handbook*. Artech House Boston, 2005, vol. 2.

[23] C. Fulton and A. Mirkamali, "Spectral analysis of embedded element patterns of cylindrical arrays", *IEEE Transactions on Antennas and Propogation*, vol. 57, no. 3, pp. 132–138, 2015.

[24] E. Brookner, B. Porter, K. Chang, Y.-C. Chang, D. Zwillinger, B. Considine, and T. Sikina, "Demonstration of accurate prediction of pave paws embedded element gain", in *Phased Array Systems and Technology (ARRAY), 2010 IEEE International Symposium on*, IEEE, 2010, pp. 417–422.

[25] Unknown. (2017). Ansys hfss perfectly matched layer boundary automation, [Online]. Available: `http://www.ansys.com/-/media/Ansys/corporate/resourcelibrary/techbrief/ab-hfss-perfectly-matched-layer-boundary-automation.pdf`.

[26] S. Karimkashi, G. Zhang, R. Kelley, J. Meier, R. Palmer, A. Zahrai, R. J. Doviak, and D. S. Zrnic, "Cylindrical polarimetric phased array radar demonstrator: Design and analysis of a frequency scanning antenna array", in *Phased Array Systems & Technology, 2013 IEEE International Symposium on*, IEEE, 2013, pp. 477–480.

[27] Wikipedia, the free encyclopedia, *Phased array*, [Online; accessed August 15, 2017], 2016. [Online]. Available: `https://en.wikipedia.org/wiki/%5Ctext%7BPhased_array%7D`.

[28] A. J. Fenn, D. H. Temme, W. P. Delaney, and W. E. Courtney, "The development of phased-array radar technology", *Lincoln Laboratory Journal*, vol. 12, no. 2, pp. 321–340, 2000.

[29] A. Ben-Israel and T. N. Greville, *Generalized inverses: theory and applications*. Springer Science & Business Media, 2003, vol. 15.

[30] C. A. Balanis, *Antenna theory: analysis and design*. John wiley & sons, 2016.

[31] C. Wolff. (). Radar basics: Patch antenna or microstrip antenna, [Online]. Available: http://www.radartutorial.eu/06.antennas/Microstrip20Antenna.en.html (visited on 07/27/2019).

[32] (). Wave ports and lumped ports, [Online]. Available: http://www.mweda.com/hfss/down/hfss-18.pdf (visited on 07/28/2019).

[33] (). Lumped port and wave port, [Online]. Available: https://www.edaboard.com/showthread.php?116727-HFSS-lumped-port-and-wave-port (visited on 07/28/2019).

[34] ANSYS, *Electromagnetics suite version 15.0.0 manual*, 2014.

[35] ——, *Workshop 4-1: Radiation boundaries*, 2015.

[36] (). Ansys hfss open regions, [Online]. Available: https://www.ansys.com/-/media/ansys/corporate/resourcelibrary/techbrief/ab-hfss-open-regions.pdf (visited on 07/29/2019).

Appendix A

Tutorials

A.1 Patch Antenna Transmission Line Model

It is seen in this thesis that both patch antennas and slot antennas are used. This section will focus on patch antennas and how to model them with transmission lines. A patch antenna is a patch of metal or conducting material that sits on top of a substrate slab. Commonly, below the substrate lies a ground plane, as seen in Figure A.1. It can also be seen in Figure A.1 that the phase of the current is cancelled, but the phase of the voltage in the fringing fields add. For an antenna to radiate, either the current must add in phase or the voltage must add in phase [30]. This voltage being in phase is what enables the patch antenna to radiate. However, in order for these fringing fields to occur and provide a voltage, the patch must be excited.

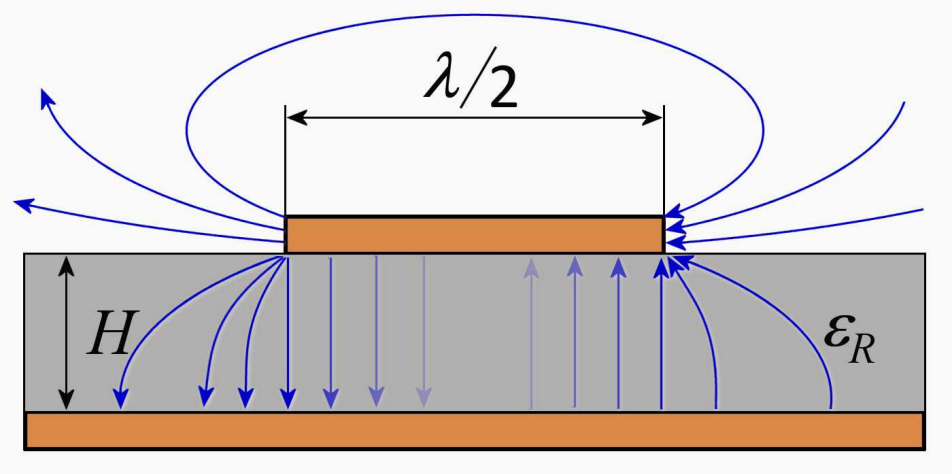

Figure A.1: Patch antenna over ground plane and associated fields [31]

Patch antennas can be excited/fed through several different means; such as a transmission line feed, aperture-coupled feed or coaxial feed. For this thesis, the focus

will be on the transmission line fed patch antenna. The most commonly used way to model a microstrip or patch antenna is through a transmission line model. It is commonly used because it is an easiest and provides a good physical insight [30]. For a rectangular patch, the length of the patch will be defined as L, the width of the watch will be defined as W, and the height off the substrate will be defined as h. The dielectric constant of the substrate is defined as ϵ_r. Because some of the waves travel tough air and some travel through the substrate, an effective dielectric constant is used to calculate parameters of the transmission line model [30]. The effective dielectric constant, ϵ_{reff} may be calculated using [30],

$$\epsilon_{reff} = \frac{\epsilon_r + 1}{2} + \frac{\epsilon_r - 1}{2}\left[1 + 12\frac{h}{W}\right]^{1/2}. \tag{A.1}$$

Additionally, because of the fringing effects, the dimensions of the patch are electrically larger than that of the physical size [30]. The following equation [30] is used calculate how much the length is increased, which is dependent on the width-to-height ratio of the antenna,

$$\frac{\Delta L}{h} = 0.412\frac{(\epsilon_{reff} + 0.3)\left(\frac{W}{h} + 0.264\right)}{(\epsilon_{reff} - 0.258)\left(\frac{W}{h} + 0.8\right)}. \tag{A.2}$$

Now the procedure for designing the patch may go as follows: for the antenna to radiate efficiently a width of the following is chosen [30],

$$W = \frac{1}{2f_r\sqrt{\mu_0\epsilon 0}}\sqrt{\frac{2}{\epsilon_r + 1}}, \tag{A.3}$$

where μ_0 is the permeability of free-space, ϵ_0 is the permittivity of free-space, and f_r is the resonant frequency. This means the three parameters that must be determined prior to the design process are ϵ_r, f_r, and h. Once W is calculated the change in length due to the fringing fields may be calculated using Equation A.2. Finally, physical length of the patch may be determined using [30],

$$L = \frac{1}{2f_r\sqrt{\epsilon_{reff}}\sqrt{\mu_0\epsilon 0}} - 2\Delta L. \tag{A.4}$$

Now that the patch dimensions are designed, a transmission line model may be built. A patch antenna may be modeled as an array of two radiating narrow apertures, or slot antennas [30]. Both patch antennas and slot antennas radiate due to the voltage being in phase along the width of the structures, rather than the current being in phase. The fringing fields that add in voltage-phase that cause the antenna to radiate may be modeled using as the voltage that occurs on a radiating slot antenna. The voltages add in the same direction and emit an electromagnetic

field that radiates away from the antenna surface for both cases. However, the magnitude of the voltage for a single slot antenna and patch antenna are not equal, so two slot antennas must be used so the voltage intensity matches that of Figure A.2. The two slots used to model the patch antenna may be labelled as Slot 1 and Slot 2. The slots will have admittances of Y_1 and Y_2, conductances of G_1 and G_2, and susceptances of B_1 and B_2, where $Y = G + jB$. The rectangular patch antenna and the transmission line model of the equivalent slots may be seen in Figure A.3.

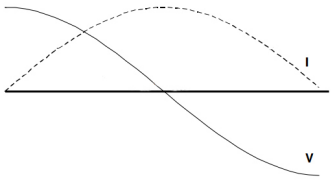

Figure A.2: Voltage and current plots for patch antenna

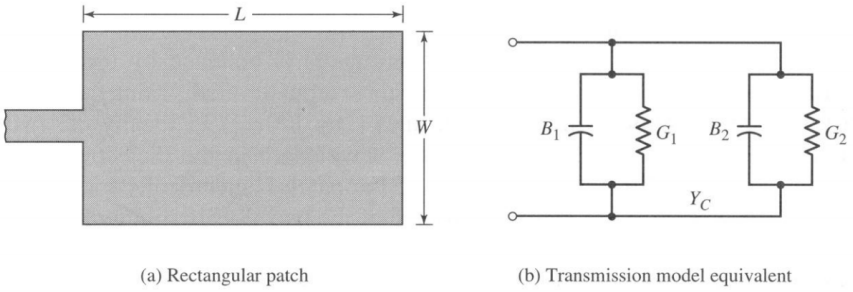

Figure A.3: Patch antenna (a) with equivalent transmission line model (b) [30]

For a slot with a finite width the conductance and susceptance may be calculated using [30],

$$G_1 = \frac{W}{120\lambda_0}\left[1 - \frac{1}{24}(k_0 h)^2\right], \tag{A.5}$$

and

$$B_1 = \frac{W}{120\lambda_0}[1 - 0.636\ln(k_0 h)]. \tag{A.6}$$

Both slots are identical so $G_1 = G_2$ and $B_1 = B_2$. As shown, the process for designing patch antennas using transmission line theory is straightforward and modeling a patch antenna using two slots provides a physical representation for the fields being radiated from a patch antenna.

A.2 Radiation Boundaries and PMLs

In HFSS, an air-box is needed to emulate free space for a simulations. If no radiation boundary is assigned, HFSS assumes the faces of the air box are perfectly electric conductors, which would cause reflections. A radiation boundary or PML is used to truncate the radiation at the edge of the air-box perpendicular to the direction of the traveling waves. Below covers the theory behind each method of truncating the electromagnetic fields at the end of the air box. Additionally, instructions on how to implement a radiation boundary and PML are included. These instructions implement radiation boundaries and a PML on a stand alone slot antenna on an infinite ground plane, finite ground plane, and antenna in an infinite array environment.

A.2.1 Radiation Boundary

A *radiation boundary* is an assigned boundary at the end of the air-box that simply truncates the radiation at that boundary. This abrupt truncation can cause the electromagnetic fields to reflect back into the air-box, causing disruptive reflections. So, the radiation boundary should be placed at a distance of $\lambda/4$ away or $\lambda/2$ from the radiating element to eliminate reflections at the boundary. It is well known that quarter wavelength spacing eliminates impedance mismatches. However, many HFSS simulations require a frequency sweep to observe how the radiating structure behaves at different frequencies. This means the radiation boundary will cause reflections and disrupt the fields for many frequencies. The distance from the radiating element to the radiation boundary may be parameterized to change with frequency. In this case, it is also recommended a mesh operation be used to absorb reflection, as an air-box is not a perfect transmission line. The mesh should seeded with a $\lambda/6$ operation for the highest frequency [35].

Radiation Boundary for Slot in an Infinite Array Environment

To implement a radiation boundary in HFSS for a slot antenna in an infinite array environment, first build the desired radiating element and respective air box, an example can be found in the figure below. The air box should extend at least $\lambda/4$ for the minimum frequency used in each direction around the antenna, as seen in Figure A.4.

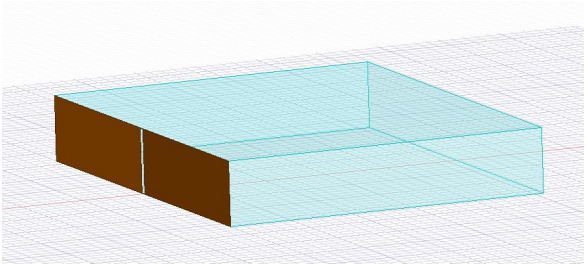

Figure A.4: Example of antenna and air-box set up

Next, select the face of the air-box, as seen in Figure Figure A.5.

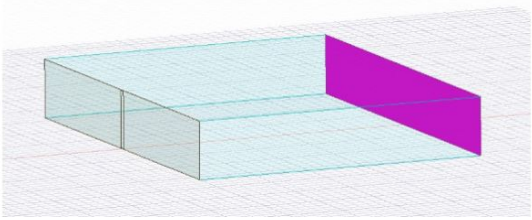

Figure A.5: Antenna and air-box set up with the non-antenna faces selected

Now, find the Project Manager and right click ”Boundaries, as seen in Figure A.6. This will bring up a selection of boundaries to choose from and the ”Radiation Boundary” option should be selected.

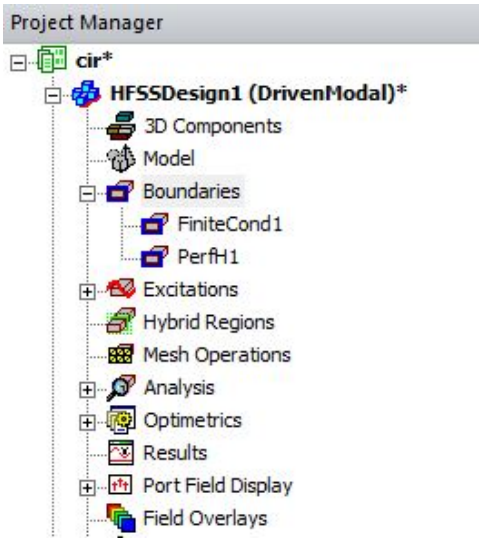

Figure A.6: Project manager selection in HFSS

Finally, the radiation boundary will be applied and should look similar to that in Figure A.7. It should be noted this design is for an infinite slot, if the desired slot is finite, the same process may be followed but with a ground plane boundary above and below the slot.

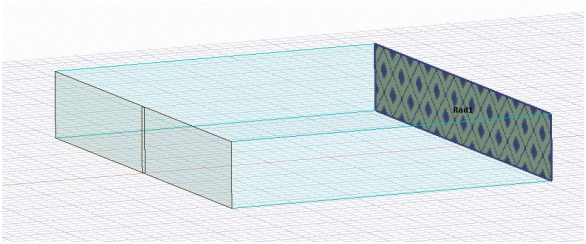

Figure A.7: Radiating element with completed radiation boundary

Radiation Boundary for Slot in an Infinite Ground Plane

To implement a radiation boundary in HFSS for a slot antenna in an infinite ground plane, first build the desired radiating element and respective air box, an example can be found in the figure below. The air box should extend at least $\lambda/4$ for the minimum frequency used in the front and back of the antenna, as seen in Figure A.8.

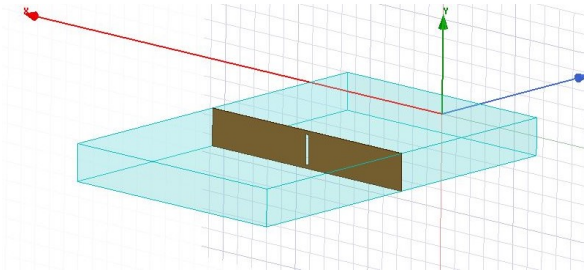

Figure A.8: Example of antenna and air-box set up for slot in an infinite ground plane

Next, select each face of the air-box, as seen in Figure A.9.

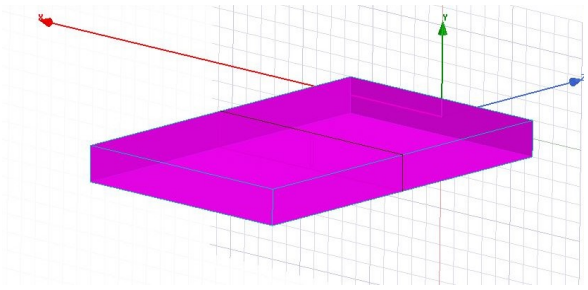

Figure A.9: Antenna and air-box set up with the faces selected for slot in an infinite ground plane

Now, find the Project Manager and right click the selection and hover over the "Assign Boundary" option. This will bring up a selection of boundaries to choose from and the "Radiation Boundary" option should be selected. Finally, the radiation boundary will be applied and should look similar to that in Figure A.10.

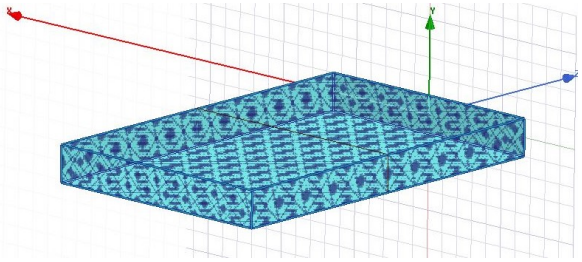

Figure A.10: Radiating element with completed radiation boundary

Radiation Boundary for Slot in a Finite Ground Plane

The same exact process is followed for applying a radiation boundary to a slot antenna simulation in an infinite ground plane as applying a radiation boundary to a slot antenna in a finite ground plane, with one important difference. For the finite ground plane case, the air box must be expanded in every direction away from the antenna element by a minimum distance of $\lambda/4$ for the minimum frequency used in the simulation. The expanded version of the air-box can bee seen in Figure A.11.

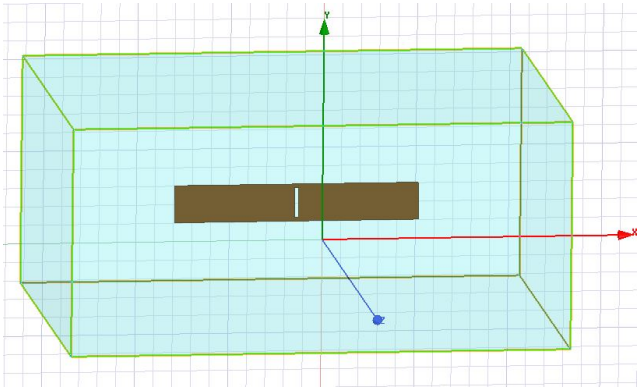

Figure A.11: Expanded air-box for finite ground plane case

A.2.2 Perfectly Matched Layer

A *perfectly matched layer* (PML) is also an assigned boundary at the end of an air-box. The PML, regardless of placement, absorbs the fields at the boundary to emulate reflection-free radiation. The PML acts as an absorber and also strongly attenuates fields propagating through it [36]. This allows for the air-box to end at a spacing that is not a quarter wavelength increment. It is recommended by ANSYS that the PML be placed at least $\lambda/8$ away from the radiating element, but as seen in Chapter 3, a greater distance may be needed. The PML is overall a more effective and flexible means of truncating radiation with out reflections occurring and allows for flexibility of the air-box length. For these reasons, a PML was chosen for the work in this thesis.

PML Boundary for Slot in an Infinite Array Environment

To implement the PML in HFSS for a slot antenna in an infinite array environment, first create the radiating element and air-box. An example of this can be seen in Figure A.4. Next, select the end face of the air-box as seen in Figure A.5. Now, right click and select the "Assign Boundary" and then "PML Setup Wizard..." option. For the PML set up it is recommended that the PML thickness is set to at least $\lambda/3$, the minimum frequency is set to the minimum frequency used in the simulation, and the minimum radiation distance is $\lambda/8$ [35]. These parameters can be visualized in Figure A.12.

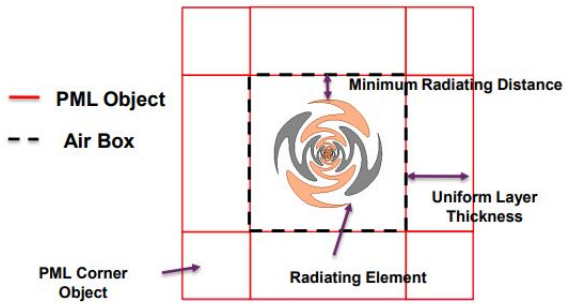

Figure A.12: Example of physical PML parameters [35]

Once the parameters in the PML Setup Wizard are finalized, the set up wizard creates the PML at the end of the air-box and should look similar to Figures A.13 and A.14.

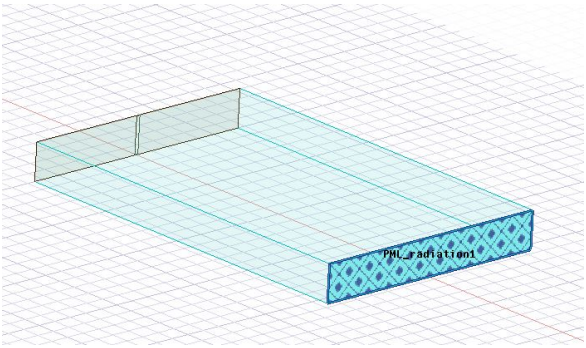

Figure A.13: Example of PML boundary surface

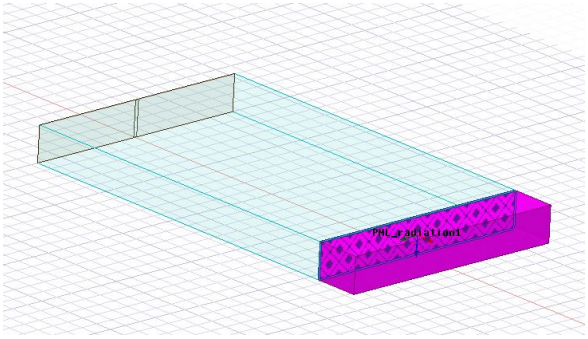

Figure A.14: Example of PML box

PML Boundary for Slot in an Infinite Ground Plane

To implement a PML boundary in HFSS for a slot antenna in an infinite ground plane, first build the desired radiating element and respective air box, an example can be found in the figure below. The air box should extend at least $\lambda/4$ for the minimum frequency used in the front and back of the antenna, as seen in Figure A.15.

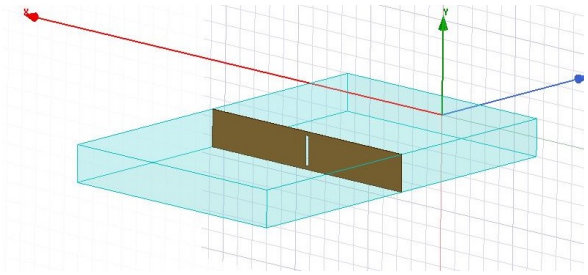

Figure A.15: Example of antenna and air-box set up for slot in an infinite ground plane

Next, select each face of the air-box, as seen in Figure A.16.

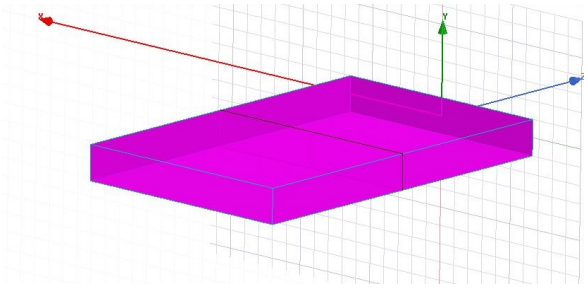

Figure A.16: Antenna and air-box set up with the faces selected for slot in an infinite ground plane

Now, find the Project Manager and right click the selection and hover over the “Assign Boundary” option. This will bring up a selection of boundaries to choose from and the ”PML Setup Wizard...” option should be selected. Once the parameters in the PML Setup Wizard are finalized, the set up wizard creates the PML, as seen in Figure A.17.

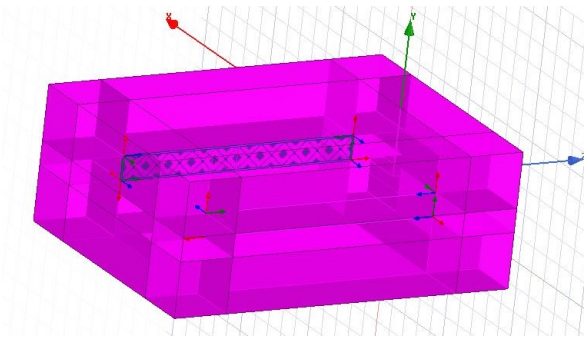

Figure A.17: PML boundary applied for slot in an infinite ground plane

PML Boundary for Slot in a Finite Ground Plane

Similar to the radiation boundary case above, the same exact process is followed for applying a PML boundary to a slot antenna simulation in an infinite ground plane as applying a PML boundary to a slot antenna in a finite ground plane. However, there is one important difference. For the finite ground plane case, the air box must be expanded in every direction away from the antenna element by a minimum distance of $\lambda/4$ for the minimum frequency used in the simulation. The expanded version of the air-box can bee seen in Figure A.18.

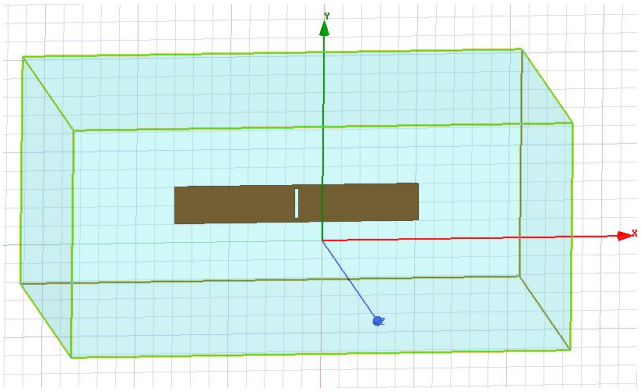

Figure A.18: Expanded air-box for finite ground plane case

A.3 Wave Ports and Lumped Ports

If the wrong excitation is applied to an antenna in HFSS, the entire electromagnetic field results will be incorrect. It is important to carefully choose the correct model excitation. Two commonly used excitations are wave ports and lumped ports. A

port is a two dimensional surface on which Maxwell's equations are solved to determine the electromagnetic fields throughout the whole model volume [32]. To show a visual example of a wave port and lumped port, an idealized dipole is excited by a wave port and by a lumped port in Figure A.19.

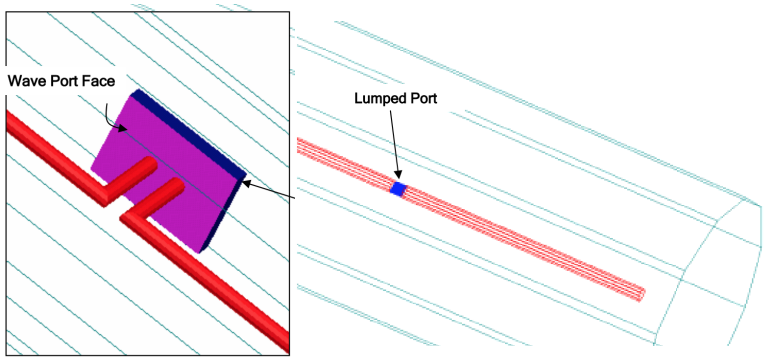

(a) Wave Port Excitation (b) Lumped Port Excitation

Figure A.19: Idealized dipole antenna excited by wave port (left) and lumped port (right) [32]

A *wave port* is a port that HFSS assumes is connected to a semi-infinitely long waveguide and the waveguide has the same physical cross section as the port itself [33]. The resulting fields from the solved Maxwell's equations on the port's surface provide a boundary condition for the model's solution. Each port is excited individually, and the characteristic impedance and propagation constants are solved for at the port crossection. The wave port is capable of determining the natural modes in the port's crossection and accounts for all relevant modes [33]. The sizing and location of the wave port is extremely sensitive because the edges of the port match the boundary characteristics of the faces that share edges with the wave port [32]. For this reason the wave port should be much larger than the element being excited. The edges of a wave port are seen as perfect electric conductor boundaries in the and if the edges are too close to the signal line, artificial coupling will alter the port impedance [33]. For a microstrip structure of height, h, and width, w, the sizing recommendation are as follows; height of the port should be between $6 \times h$ and $10 \times h$ [34]. The width of the port should be $10w$ if $w \geq h$ or $5w$ if $w < h$ [34]. A wave port should be placed on an outer surface perpendicular to the direction of traveling waves for structures in HFSS, if placed internally as in Figure A.19, a cap is needed.

A *lumped port* is similar to a wave port but is recommended for surfaces internal to the model, as seen in Figure A.19. However, lumped ports have perfect electric conductor boundaries on the edges that touch conductors and perfectly magnetic conductor boundaries on the edges that do not touch conductors [33]. Recall that all wave port edges assume perfect electric conductor boundaries if no edges are

shared with other design elements. This forces a field distribution that creates a uniform current, which is the equivalent of the fundamental mode for an infinite planar waveguide [33]. This means unlike wave port excitations, the lumped port excitation only accounts for the fundamental mode. Additionally, the user must manually input a reference impedance for the S-matrix on the lumped port [33]. Lumped ports also may not touch master/slave boundary conditions, making them a poor candidate for unit cell analysis simulations.

Overall, when choosing between a wave port excitation and lumped port excitation, the placement of the port may be an initial reference for which port to choose. Wave ports are recommended for external surfaces while lumped ports are generally recommended for internal surfaces. Wave ports make better candidates for microstrip structures because the fields occurring in, outside, and around the strip will be accounted for. Additionally, a wave port accounts for the numerous modes that occur within a waveguide structure while the lumped port only accounts for the fundamental mode. However, due to the simplicity of the lumped port, they can make good candidates for internal surfaces. This usually makes lumped ports ideal candidates for slot antennas. Slot antennas radiate due to the addition in phase of the voltage across the slot. In other words, there is a voltage difference applied to the inner edges of the slot antenna. As described above, this is what a lumped port excitation does; a constant current is forced creating a voltage difference between the edges of the port. However, because lumped ports may not touch surfaces with master/slave boundary conditions, a lumped port may not be used for the slot antenna unit cell analysis in Chapter 3 and a wave port is chosen instead.

A.4 Implementing a Wave Port and Lumped Port on a Slot Antenna in HFSS

As stated in the previous section, both wave ports and lumped ports may be used to excite different radiating elements in HFSS. This section will cover how to implement a wave port and lumped port on a slot antenna. This slot antenna will be independent of other elements and will not have any master/slave boundary conditions applied to it so both implementations may be shown. The wave port implementation is the implementation used for the slot antenna in Chapter 3.

A.4.1 Wave Port Implementation, Case 1: Infinite Array Environment

To begin the wave port implementation, build the slot, air-box, and desired radiation truncation boundary. In this example an infinite slot as used. Make sure the material assigned to the area surrounding the slot is a perfect electric conductor. An example of what this will look like can be seen in Figure A.20.

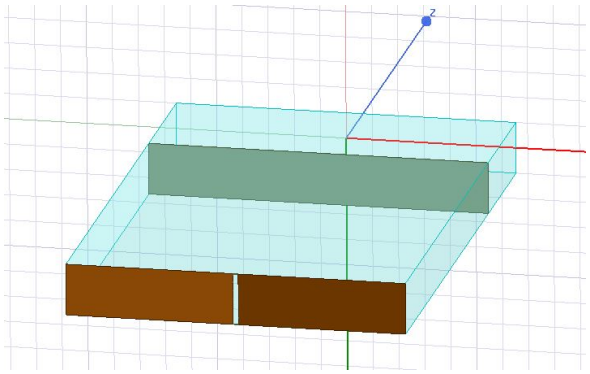

Figure A.20: Example of initial slot antenna set up

Now that the antenna is built, setting up the excitation may begin. The first step in setting up the excitation is creating the perfect magnetic boundary the top and bottom of the slot. To do this, create a rectangle that is equal to the size of the slot. Now subtract the majority of the middle portion of the rectangle so all that remains is two small slivers of material at the top and bottom of the slot, as seen in Figure A.21.

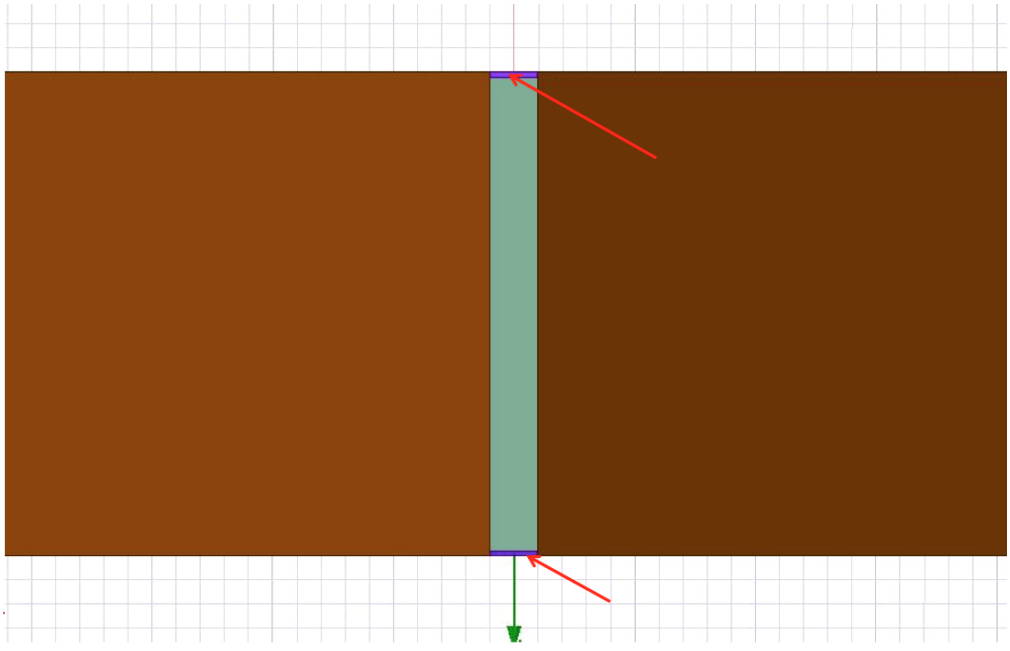

Figure A.21: Perfect H boundary components left over from rectangle subtraction, indicated by red arrows

Next, right click the small remaining surface and select “Assign Boundary.” Then assign a “Perfect H” boundary. This perfect H boundary is assigned so a constant current is forced across the slot. This is done automatically with a lumped port, but for a wave port this boundary needs to be assigned so the wave port assumes a perfect magnetic conducting boundary for the top and bottom edges. As stated in Section A.3, a wave port in HFSS assumes the boundaries of the edges it is in contact with. Now create a rectangle in the space that was left from creating the perfect H boundaries, as shown highlighted in purple in Figure A.22.

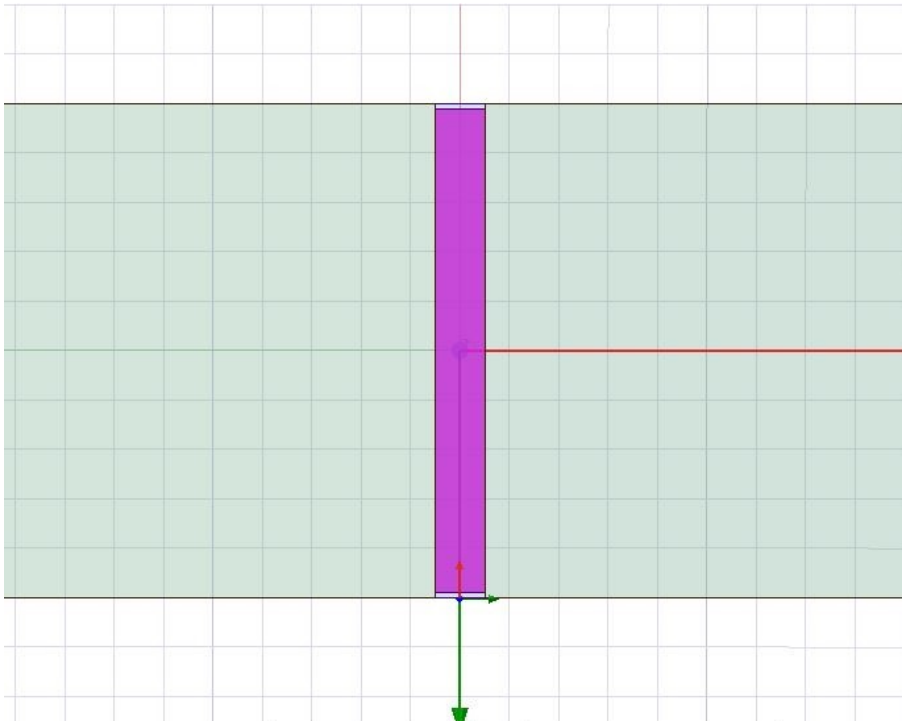

Figure A.22: Rectangle created for wave port assignment highlighted in purple

Once this rectangle is created, right click the rectangle and select “Assign Excitation,’ then select “Wave Port.” Now, the integration line must point across the slot so in the box that says “Integration Line,” change the value from “None” to new line. It will then prompt the user to define the line, define the line from one vertical edge of the slot to the other. The next option allows the user to re-normalize the port to a specific impedance, this may be done if needed. Once the port is created the final result should look similar to Figure A.23. Because the wave port edges to the left and right of the slot are touching a perfectly electric conductor, the port adopts these boundaries. Meaning this wave port essentially acts as a lumped port with the benefit of still being able to apply master/slave conditions in the simulation.

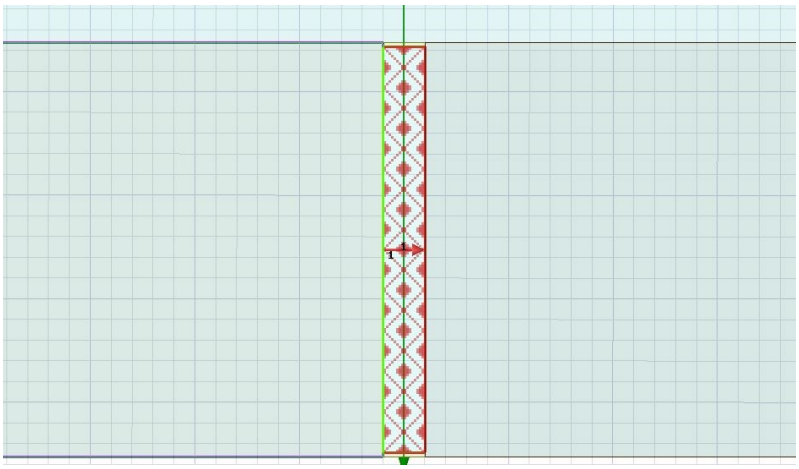

Figure A.23: Wave port assigned across slot

A.4.2 Wave Port Implementation, Case 2: Singular Slot Antenna (non-array)

This implementation is similar to that of the infinite array environment. However, if the slot antenna is to be simulated on its own, not in an array, an additional step must be taken to ensure the wave port adopts the correct surface boundary condition. In this example a finite slot on an infinite ground plane is shown, but the same stems may be taken for setting up a wave port on a finite ground plane once the air-box is expanded. First, build the slot antenna and air-box, as seen in Figure A.8. Next, as previously done, build two small rectangles at the top and bottom of the slot as seen in Figure A.24 in green.

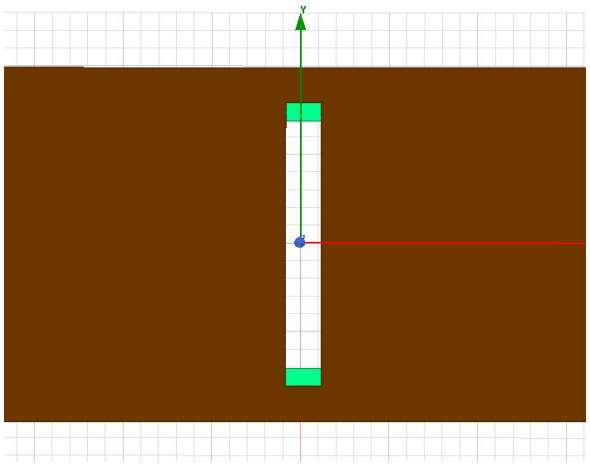

Figure A.24: Rectangles created for perfect magnetic conductor boundary, shown in green

Once these rectangles are placed, assign the “perfect H” boundary to each of the small rectangles. Now create a rectangle that fits in the blank space as seen in the yellow portion of Figure A.25

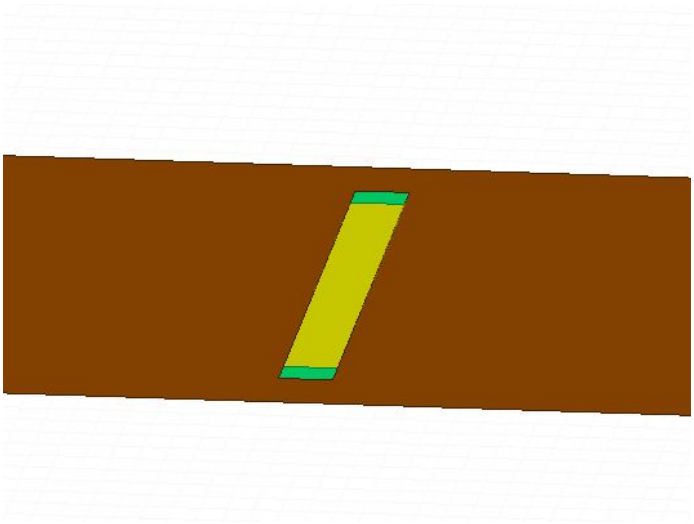

Figure A.25: Yellow rectangle created for wave port placement

Now, in order for the wave port to assume perfect electric conducting (PEC) conditions on the edges, rather than air, a PEC cap is used. To build the cap create a box above the yellow rectangle created in the last step, as shown in Figure A.26. Once this box is built, assign the “perfect E...” boundary to the box.

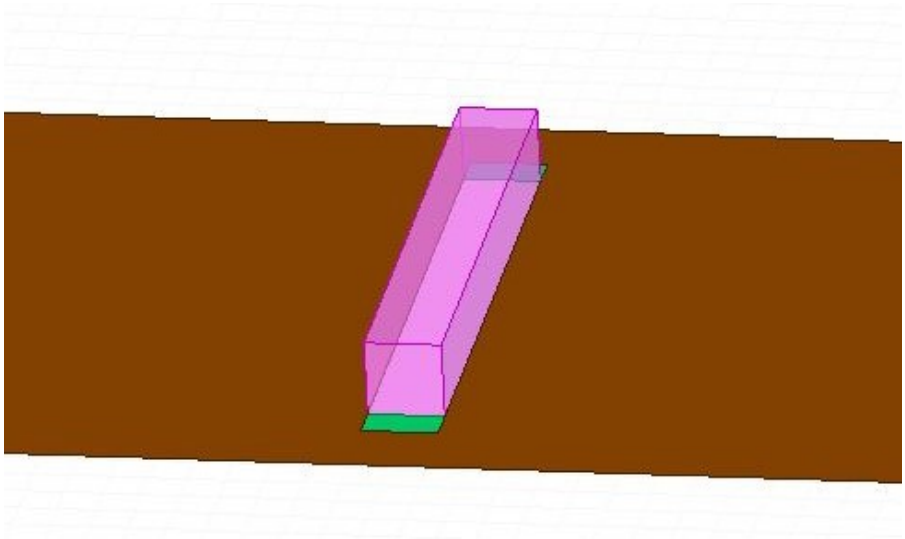

Figure A.26: Box for perfect wave port cap, shown in pink

Finally, select the yellow rectangle that was created in Figure A.25 and right click the selection. From the drop down menu, choose the options that says, "Assign Excitation," and choose "Wave Port." Proceed through the wave port set up as described in Section A.4.1 to obtain the final wave port excitation. When this is complete the wave port should look similar to Figure A.27.

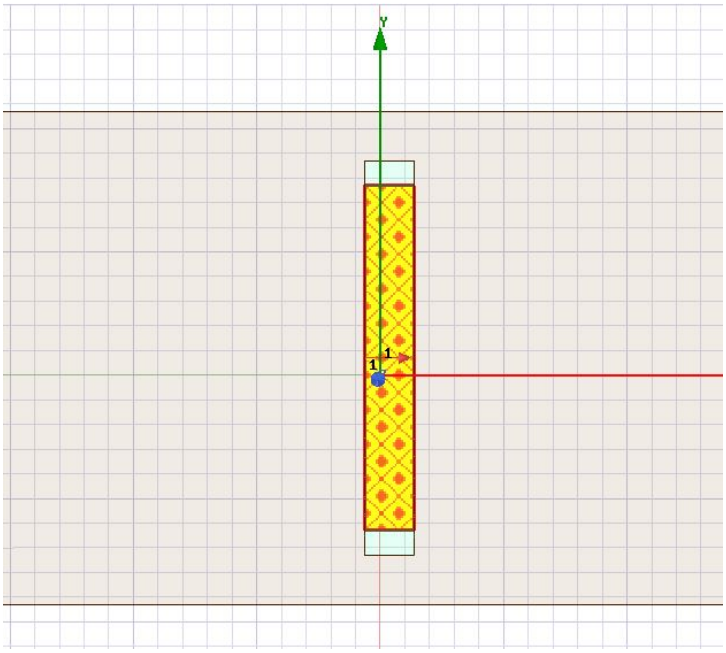

Figure A.27: Example of final wave port result for finite slot antenna

A.4.3 Lumped Port Implementation

This section will show the steps to take in order to set up a lumped port excitation for a slot antenna. This is the traditional and ideal excitation to use with a slot antenna if no master/slave boundary conditions are needed. To begin the lumped port implantation, build the slot antenna, air-box, and radiation truncation method as in Figure A.20. Next, in the space where the slot of the antenna is, create a rectangle that fits exactly in this space, as in Figure A.28.

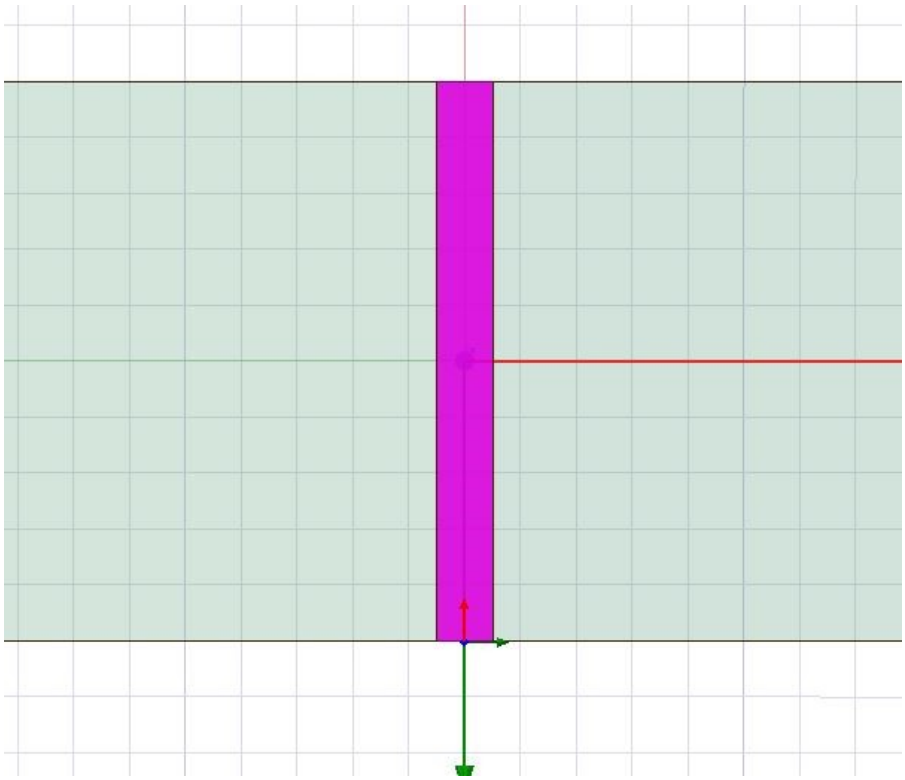

Figure A.28: Rectangle crated to apply excitation

Next, select the rectangle and right click to select “Assign Excitation.” Select the option that says “Lumped Port.” Now enter the desired impedance and click the “Next” button. Again, it will prompt the user to choose an integration line. Change the selection from “None” to “New Line,” and assign the integration line in the same manner as was done for the wave port; across the slot. Finally, the nodes may be re-normalized to the input impedance if desired, and the port is complete. The final result should look similar to Figure A.29. The difference between Figure A.23 and Figure A.29 is subtle, but the length of the lumped port matches that of the antenna height, while the length of the wave port is less than the antenna height to create the perfect H boundaries.

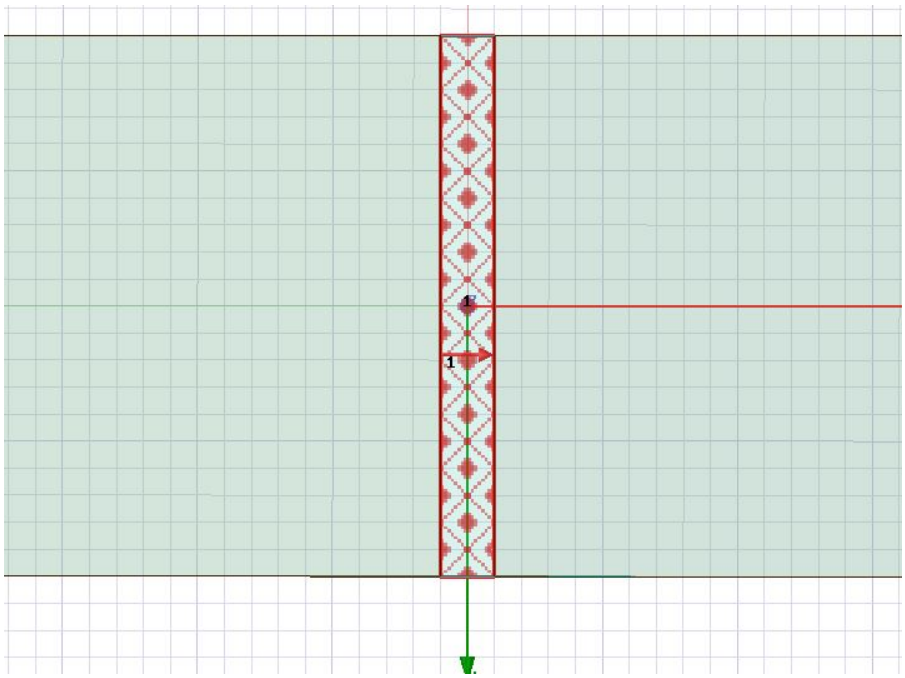

Figure A.29: Example of assigned lumped port on slot antenna

Appendix B

Code

B.1 PML Boundary and Phase Mode Spectrum Code

Chapter Four MATLAB Code

Listing B.1: PML Boundary and Phase Mode Spectrum Code

```
clear all
close all

elem = 96; %number of elements in the array
shift = 360/elem; %Master Slave relation will increase in
   increments of this amount

pathtofiles = '.\';

% dTheta = 3;
dPhi = 360/elem/2;
nTheta = 20;
nPhi = (elem)*4;
nModes = elem;
S = round(90/dPhi);
WedgeLa = 150; %in mm

phi = linspace(0, 360, nPhi+1);
phi = phi(1:(end-1));


theta = [90];
nTheta = numel(theta);


spaces = ['H32'; 'V32'];
spaces2 = ['387.5'; '312.5'; '237.5'; '162.5'; '112.5'];
nVar = 2;
```

```
ePhi_H_PM = zeros(nVar, nPhi, nModes);

for n = 1:nVar
   PhiFile(n,:) = [pathtofiles 'CPPARpml' spaces(n,:) '.csv'
      ]; %file name matching HFSS exports

   EPhiData(n,:,:) = csvread(PhiFile(n,:), 1,0);
   EPhiDataAng(n,:,:) = csvread(PhiFile(n,:), 1,(elem+1));

end
for n = 1:nVar
   h1 = waitbar(n/nVar);

 ePhi_H(n,:,:) = 10.^(EPhiData(n,1:(nPhi),2:(elem+1))/20).*
    exp(1i*(EPhiDataAng(n,1:(nPhi),1:(elem))*pi/180));

end
close(h1)


for n = 1:nVar
for m = 1:nModes
   l = -shift*(m-1);
   h1 = waitbar(m/nModes);
   % Actual CPSE fields:
   ePhi_H_PM(n,:,m) = shiftsumNew(nModes,l, ePhi_H(n,:,m));
end
end
close(h1)

for n = 1:nVar
ePhi_H_total(n,:) = sum(ePhi_H_PM(n,:,:), 3)/nModes;
end

phasAx = linspace(0,elem,elem*4);
phiAx = linspace(0,360,elem*4);

for n = 1:nVar
q(n,:) = 20*log10(abs(circshift(ePhi_H_total(n,:), [0 S*2]))
   )-max(20*log10(abs(circshift(ePhi_H_total(n,:), [0 S*2]))
   ));
end

figure(1)
```

```
% poop(n) = (200+50*(n-1));
subplot(2,1,1)
hhh = plot(phiAx, q(:,:))
set(hhh, {'color'}, num2cell(jet(nVar), 2));
zlim([-60 30]); caxis([-60 30]); view(2)
xlabel('Phi')
ylabel('E_\phi in dB')
% title(['E_\phi field for cylinder radius of ' num2str
   (200+50*(n-1)) 'mm and element spacing of ' num2str(2*(
   tan((360/elem/2)*pi/180)*(poop(n)+WedgeLa))) 'mm'])
title(['E_\phi field for cylinder radius of ' num2str(1000)
   'mm and element spacing of ' num2str(2*(tan((360/elem/2)*
   pi/180)*(1000))) 'mm'])

subplot(2,1,2)
hh = plot(phasAx, 20*log10(abs(fft(ePhi_H_total(:,:), [], 2)
   )));
set(hh, {'color'}, num2cell(jet(nVar), 2));
zlim([-50 50]); caxis([-50 50])
xlabel('Phase Mode Index')
ylabel('theta index')
% title(['Phase mode spectrum for cylinder radius of '
   num2str(poop(n)) 'mm and element spacing of ' num2str(2*(
   tan((360/elem/2)*pi/180)*(poop(n)+WedgeLa))) 'mm'])
title(['Phase mode spectrum for cylinder radius of ' num2str
   (1000) 'mm and element spacing of ' num2str(2*(tan((360/
   elem/2)*pi/180)*(1000))) 'mm'])
legend(spaces)
view(2)
```

B.2 Alternating Projections and Phase Mode Reduction Code

Chapter Five MATLAB Code

Listing B.2: Alternating Projections Code

```
clc
clear all
close all

elem = 96; %number of elements in the array
shift = 360/elem; %Master Slave relation will increase in
   increments of this amount
```

```
pathtofiles = './';

% dTheta = 3;
dPhi = 360/elem/2;
nTheta = 20;
nPhi = 384;
nModes = elem;
S = round(90/dPhi);
nVar = 2;
WedgeLa = 120; %in mm

phi = linspace(0, 360, nPhi+1);
phi = phi(1:(end-1));

theta = [90];
nTheta = numel(theta);

% files = dir('patterns_2p77_14ft.mat');
% files = files([1:18 20:end]);
PO = 3.9; % position offset
VO = 10; % dB correction for V horn
VOsim = 1.8; % dB correction to line up with simulated
   difference
ffi = 2; % far-field horn index
heighttrack = 1; % Height tagged or not?
f = 2.76E9;


spaces = ['H'; 'V'];
% spaces2 = ['387.5'; '312.5'; '237.5'; '162.5'; '112.5'];

ePhi_PM = zeros(nVar, nPhi, nModes);

for n = 1:nVar
   PhiFile(n,:) = [pathtofiles 'CSIM5' spaces(n,:) '.csv'];
      %file name matching HFSS exports

   EPhiData(n,:,:) = csvread(PhiFile(n,:), 1,0);
   EPhiDataAng(n,:,:) = csvread(PhiFile(n,:), 1,(elem+1));
end

for n = 1:nVar
 h1 = waitbar(n/nVar);
 ePhi(n,:,:) = (10.^(EPhiData(n,1:(nPhi),2:(elem+1))/20)).*
    exp(1i*(EPhiDataAng(n,1:(nPhi),(1:elem))*pi/180));
```

```
end
close(h1)

for n = 1:nVar
for m = 1:nModes
   l = -shift*(m-1);
   h1 = waitbar(m/nModes);
   % Actual CPSE fields:
   ePhi_PM(n,:,m) = shiftsumNew(nModes,l, ePhi(n,:,m));
end
end
close(h1)

for n = 1:nVar
ePhi_total(n,:) = sum(ePhi_PM(n,:,:), 3)/nModes;
end

A = linspace(0,96,384);
AA = linspace(-180,180,384);

FHH = ePhi_total(1,:);
FVV = ePhi_total(2,:);

FHHz = circshift(FHH, 96);
FVVz = circshift(FVV, 96);

figure(32)
plot(AA, 20*log10(abs(FHHz))-max(20*log10(abs(ePhi_total
   (1,:)))))
hold on
plot(AA, 20*log10(abs(FVVz))-max(20*log10(abs(ePhi_total
   (1,:)))))
xlim([-180 180])
ylim([-70 0])
legend('H','V')
xlabel('\phi (degrees)')
ylabel('dB')
title('CPPAR H and V Embedded Element Patterns')
hold off


ElimH = (1/sqrt(96))*circshift((fft((FHH))),193);

ElimHH = [0.001*ones(1,143) ElimH(144:216) 0.001*ones(1,168)
   ];
```

```
InElimHH = ifft(ElimHH);

figure(17)
plot(AA,InElimHH)
xlim([-180 180])

figure(34)
plot(A, circshift(abs(fft((FHH'))),193))
hold on
plot(A, circshift(abs(fft((FVV'))),193))
xlim([0 96])
hold off

%%

for k = 1:elem
FHH1(k,:) = circshift(FHH,4*k+96);
FVV1(k,:) = circshift(FVV,4*k+96);
end

FHH = FHH1;
FVV = FVV1;

   dl = 1; % number of "dummy" columns on left
   dr = 1; % number of "dummy" columns on right
   % Other CPPAR Stuff
   r = .99; % radius
   dz = 0.07; % dz spacing
   dp = 3.75; % rotation angle per column

   % Describe sector and mask goals parametrically
   Nt = elem; % total number of columns
   N = 22; % columns per sector
   winH = taylorwin(N, 4, -25);
   winV = taylorwin(N, 4, -90);
   Eh = 2; Ev = 3;
   % Eh = 1; Ev = 1;
   L0 = -50; P0 = 160;
   L1 = -30; P1 = 110;
   L2 = -30; P2 = 45;
   L3 = -25; P3 = 8.1;
   L4 = 0; P4 = 4.5;
   maxiters = 32;
   res = dp/Nt; % angular resolution for interpolated
      patterns
```

```
   wgt = -0.8; % WLS weight parameter (negative: emphasize
      sidelobes more)

   % Derived parameters
   lambda = 3e8/f;
   k0 = 2*pi/lambda;
   Na = Nt-dl-dr; % number of active channels;
   Ns = Na-N+1; % number of sectors to crank out
   cc = ((1:Nt)-(Nt+1)/2)*dp; % angles of column centers

   AZ = -180:(360/384):180;
   AZ = AZ(1:(end-1));

   for k = (1+dl):(Nt-dr)

pat_peakH = max((abs(FHH(1,:))));
pat_peakV = max((abs(FVV(1,:))));

      figure(1)
      plot(AZ, 20*log10(abs(FHH(k,:))), 'linewidth', 1.5);
      hold on
      plot(AZ, 20*log10(abs(FVV(k,:))), 'r', 'linewidth',
         1.5);
%       plot(AZ, 20*log10(abs(FHV(k,:))), '--', 'linewidth',
   1.5);
%       plot(AZ, 20*log10(abs(FVH(k,:))), 'r--', 'linewidth',
    1.5);
      hold off
      grid on
      set(gca, 'fontsize', 13)
      xlabel('AZ, deg.')
      ylabel('Pattern, dB')
      title(sprintf('Pattern for for element %d%', k))
      xlim([min(AZ) max(AZ)]);
      ylim([-50 20]);
      pause(.01)
   end

% sigl = .01
sigl = 0; % simulated (faked!!!) leakage, just for testing
% Align channels...
for k = (1+dl):(Nt-dr)
   FHH(k,:) = (FHH(k,:)/pat_peakH) + sigl*sqrt(2)/2*(randn()
      +1i*randn());
   FVV(k,:) = (FVV(k,:)/pat_peakV) + sigl*sqrt(2)/2*(randn()
```

```
      +1i*randn());
%    FVH(k,:) = FVH(k,:)/pat_peakV(k) + sigl*sqrt(2)/2*(randn
   ()+1i*randn());
%    FHV(k,:) = FHV(k,:)/pat_peakH(k) + sigl*sqrt(2)/2*(randn
   ()+1i*randn());

   figure(2)
   plot(AZ, 20*log10(abs(FHH(k,:))), 'linewidth', 1.5);
   hold on
   plot(AZ, 20*log10(abs(FVV(k,:))), 'r', 'linewidth', 1.5);
%    plot(AZ, 20*log10(abs(FHV(k,:))), '--', 'linewidth',
   1.5);
%    plot(AZ, 20*log10(abs(FVH(k,:))), 'r--', 'linewidth',
   1.5);
   hold off
   grid on
   set(gca, 'fontsize', 13)
   xlabel('AZ, deg.')
   ylabel('Pattern, dB')
   title(sprintf('Pattern for for element %d%', k))
   xlim([min(AZ) max(AZ)]);
   ylim([-70 0]);
   pause(.01)
end
%%
% Define the sidelobe mask for a broadside scan
mask = L0*(abs(AZ) >= P0);
mask = mask + (L1 - (L1-L0)/(P0-P1)*(abs(AZ)-P1)).*(abs(AZ)
   >= P1).*(abs(AZ) < P0);
mask = mask + (L2 - (L2-L1)/(P1-P2)*(abs(AZ)-P2)).*(abs(AZ)
   >= P2).*(abs(AZ) < P1);
mask = mask + (L3 - (L3-L2)/(P2-P3)*(abs(AZ)-P3)).*(abs(AZ)
   >= P3).*(abs(AZ) < P2);
mask = mask + (L4 - (L4-L3)/(P3-P4)*(abs(AZ)-P4)).*(abs(AZ)
   >= P4).*(abs(AZ) < P3);
% mask = mask.*(1-(8 < AZ).*(AZ < 50)) + -30*(8 < AZ).*(AZ <
    50);
mask = 10.^(mask/20);

% Build patterns and their "pseudo-inverses"
masks = zeros(numel(AZ), Ns);
Wghts = zeros(numel(AZ), numel(AZ), Ns);

pat_invsH = zeros(N, numel(AZ), Ns); % Pattern "pseudo-
   inverses," taking weights into account
```

```
pat_invsV = zeros(N, numel(AZ), Ns); % Pattern "pseudo-
   inverses," taking weights into account
sc = zeros(Ns,1); % Sector scan centers, in deg.
for k = 1:Ns
   sc(k) = cc(dl+N/2+k-1)+dp/2;
   FHHs(:,:,k) = FHH((dl+(1:N)+k-1),:).';
   FVVs(:,:,k) = FVV((dl+(1:N)+k-1),:).';

   masks(:,k) = circshift(mask, [0 -round(sc(k)/res)]);
   Wghts(:,:,k) = diag(squeeze(masks(:,k).^wgt));
   pat_invsH(:,:,k) = (squeeze(FHHs(:,:,k))'*squeeze(Wghts
      (:,:,k))*squeeze(FHHs(:,:,k)))^(-1)*squeeze(FHHs(:,:,k
      ))'*squeeze(Wghts(:,:,k));
   pat_invsV(:,:,k) = (squeeze(FVVs(:,:,k))'*squeeze(Wghts
      (:,:,k))*squeeze(FVVs(:,:,k)))^(-1)*squeeze(FVVs(:,:,k
      ))'*squeeze(Wghts(:,:,k));
end

EE = squeeze(Wghts(:,:,30));

FH = zeros(numel(AZ), Ns); % Co-pol of initial pattern
FV = zeros(numel(AZ), Ns); % Cross-pol of initial pattern
wH = zeros(N, Ns);
wV = zeros(N, Ns);
for n = 1:Ns
   for k = 1:N; % Variation in columns
      xkn = r*sind(sc(n)+(k-N/2-0.5)*dp); % x-coordinate of
         current element
      ykn = r*cosd(sc(n)+(k-N/2-0.5)*dp);
      wkn = exp(-1i*k0*(ykn*cosd(sc(n)) + xkn*sind(sc(n))));
          %weights for scanning
      wknH = wkn*cosd((k-N/2-0.5)*dp)^Eh; % correct for
         element density near edges of sector
      wknV = wkn*cosd((k-N/2-0.5)*dp)^Ev; % correct for
         element density near edges of sector
      wH(k,n) = wknH*winH(k); % final port weight
      wV(k,n) = wknV*winV(k); % final port weight
      % Beamform
      FH(:,n) = FH(:,n) + wH(k,n)*squeeze(FHHs(:,k,n));
      FV(:,n) = FV(:,n) + wV(k,n)*squeeze(FVVs(:,k,n));
   end
end

% The actual algorithm...
pc = zeros(2,2,Ns);
```

```
FHHb = FH;
FVVb = FV;
FHVb = FH*0;
FVHb = FV*0;
w_newH = zeros(N,Ns);
w_newV = zeros(N,Ns);
for n = 1:Ns
   for iters = 1:maxiters

      % Fix the pattern
      MH = max(abs(FHHb(:,n)));
      MV = max(abs(FVVb(:,n)));
      FHn = FHHb(:,n)/MH;
      FVn = FVVb(:,n)/MV;
      FHHn_mod = FHn.*(abs(FHn) < squeeze(masks(:,n))) + FHn
         .*squeeze(masks(:,n))./abs(FHn+eps).*(abs(FHn) >=
         squeeze(masks(:,n)));
      FVVn_mod = FVn.*(abs(FVn) < squeeze(masks(:,n))) + FVn
         .*squeeze(masks(:,n))./abs(FVn+eps).*(abs(FVn) >=
         squeeze(masks(:,n)));
      MB = find(squeeze(masks(:,n)) == 1);
      pad = round(res*2/3);
      FVVn_mod((MB(1)-pad):(MB(end)+pad)) = FHHn_mod((MB(1)-
         pad):(MB(end)+pad));

      % Calculate WLS fit to weights
      w_newH(:,n) = squeeze(pat_invsH(:,:,n))*FHHn_mod;
      w_newV(:,n) = squeeze(pat_invsV(:,:,n))*FVVn_mod;
%       w_newH(4,:) = -.0015;


      % Calculate new pattern
      FHHb(:,n) = zeros(numel(AZ,1));
      FVVb(:,n) = zeros(numel(AZ,1));

      for k = 1:N
         FHHb(:,n) = FHHb(:,n) + w_newH(k,n)*squeeze(FHHs(:,
            k,n));
         FVVb(:,n) = FVVb(:,n) + w_newV(k,n)*squeeze(FVVs(:,
            k,n));
      end


      if iters == maxiters
         % Polarization correction
```

```
        indc = MB(round(numel(MB)/2));
        pc(:,:,n) = [FHHb(indc,n) FHVb(indc,n); FVHb(indc,n
           ) FVVb(indc,n)]^(-1);

        figure(666)
        plot(AZ, 20*log10(abs(squeeze(FHHb(:,n)))), '
           linewidth', 1.5)
        hold on
        plot(AZ, 20*log10(abs(squeeze(FVVb(:,n)))), 'r', '
           linewidth', 1.5)
%         plot(AZ, 20*log10(abs(squeeze(FHVb(:,n)))), '--',
   'linewidth', 1.5);
%         plot(AZ, 20*log10(abs(squeeze(FVHb(:,n)))), 'r--',
    'linewidth', 1.5);
        plot(AZ, 20*log10(squeeze(masks(:,n))), 'g', '
           linewidth', 1)
        hold off
        set(gca, 'FontSize', 13)
        xlabel('AZ, deg.'); ylabel('Pattern, dB')
        title(['Far Field Pattern with ' num2str(L0) 'dB
           Backradiation Mask and ' num2str(wgt) ' Weight
           Factor'])
        legend('H','V')
        axis([-180 180 -70 1])
        grid on

        OFF = 18;
        figure(668)
        plot(20*log10(abs(squeeze(w_newH(:,n))))+OFF, '
           linewidth', 1.5)
        hold on
        plot(20*log10(abs(squeeze(w_newV(:,n))))+OFF, 'r',
           'linewidth', 1.5)
        hold off
        set(gca, 'FontSize', 13)
        xlabel('element number in sector '); ylabel('Weight
           , dB')
        title(['Final Element Weights for Sector ' num2str(
           n)])
        legend('H','V')
        axis([1 N -30 1])
        grid on

        pause(.01)
      end
```

```
    end
end
```